

Figure 1.

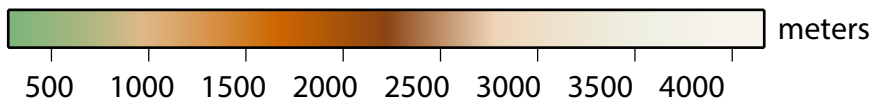
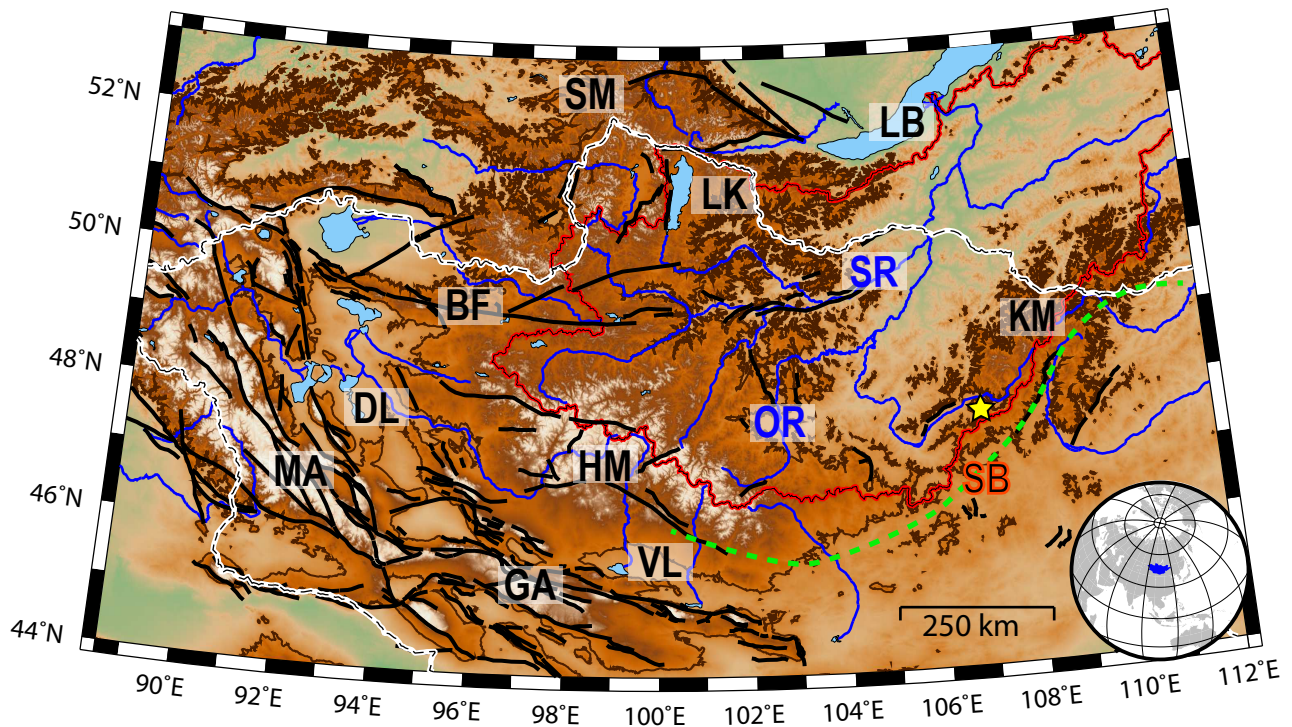




Figure 2.

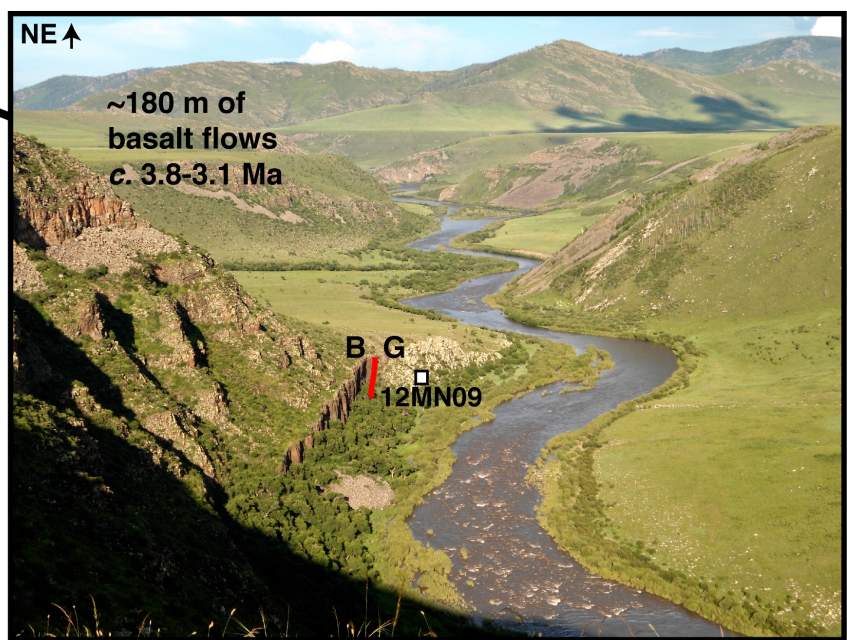
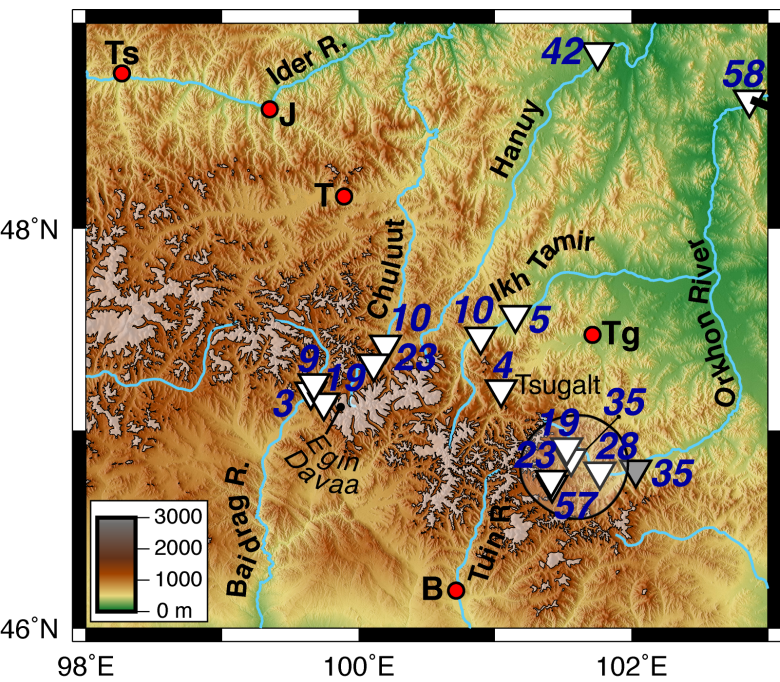
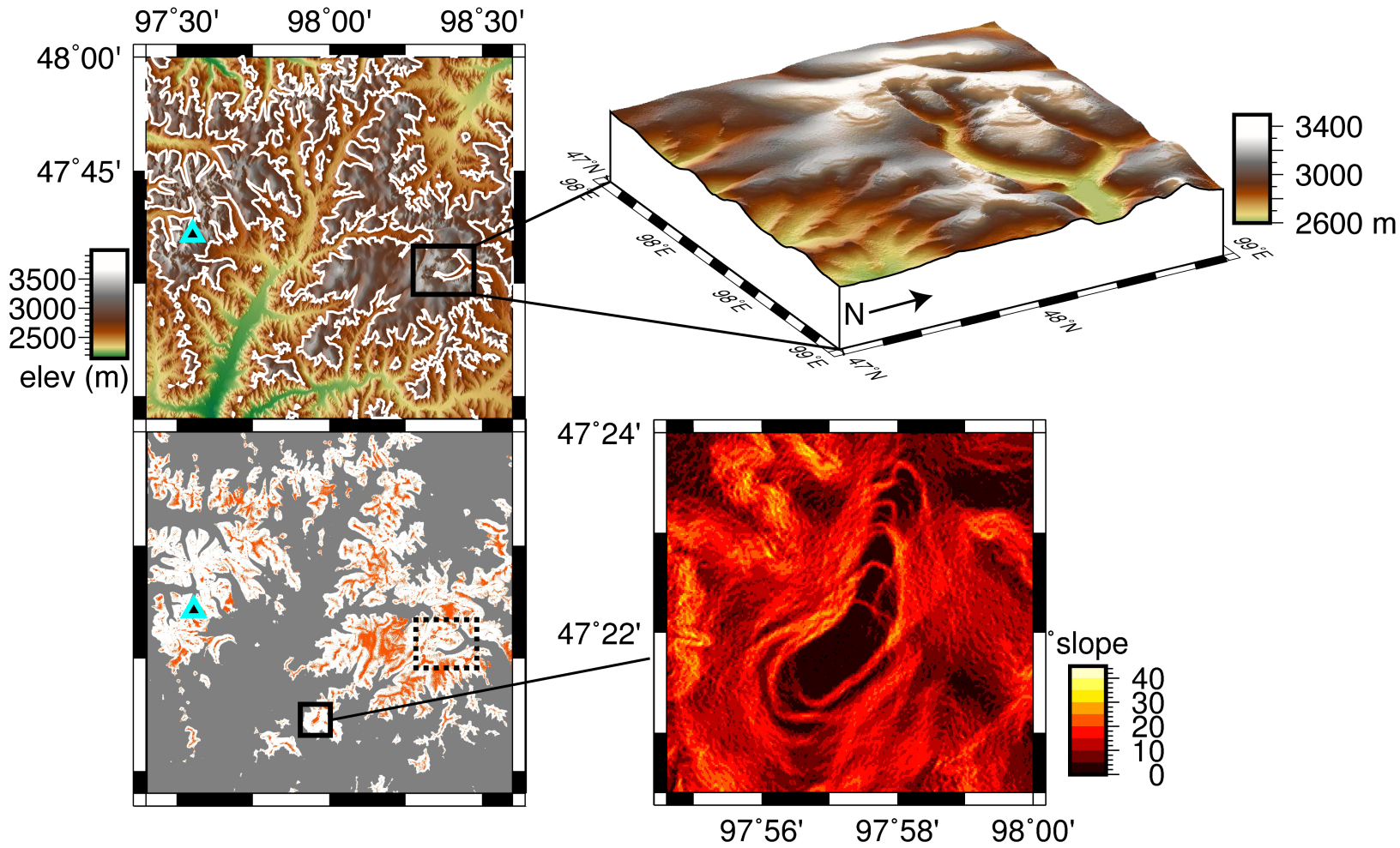


Figure 3.



**Figure 4.**

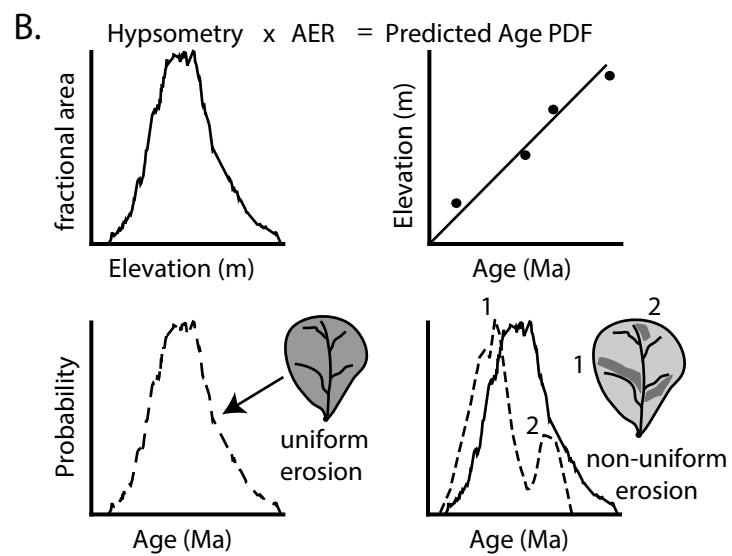
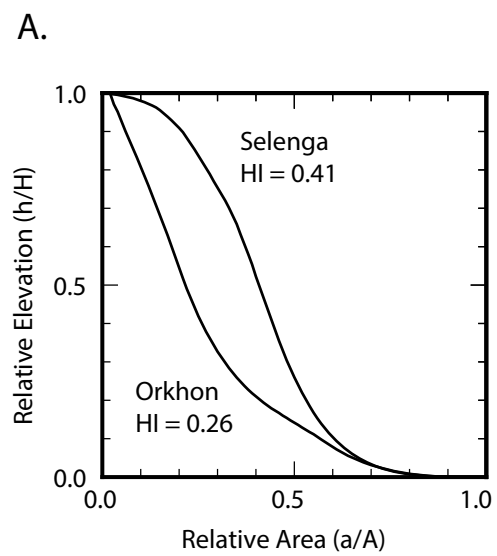




Figure 5.

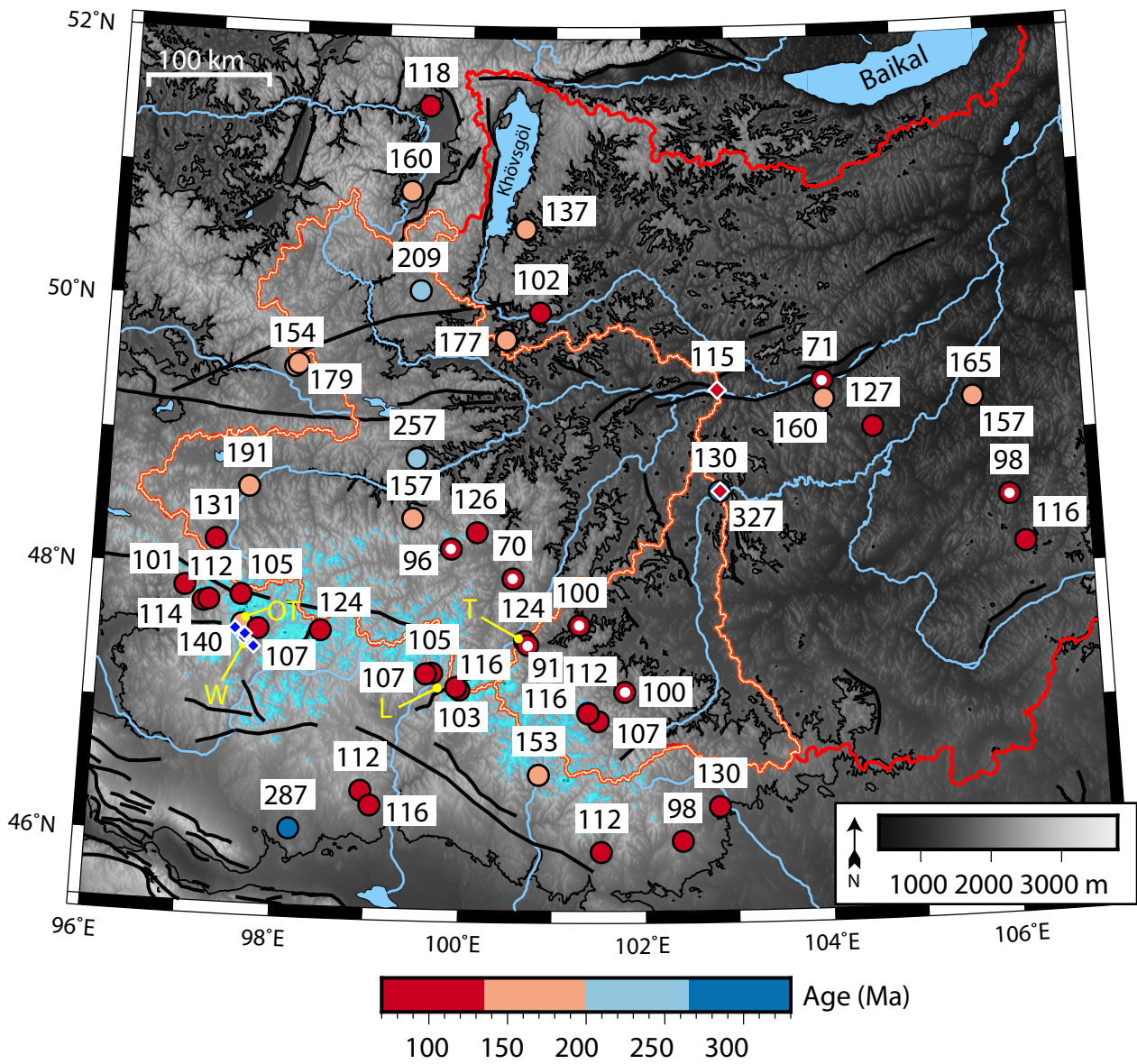
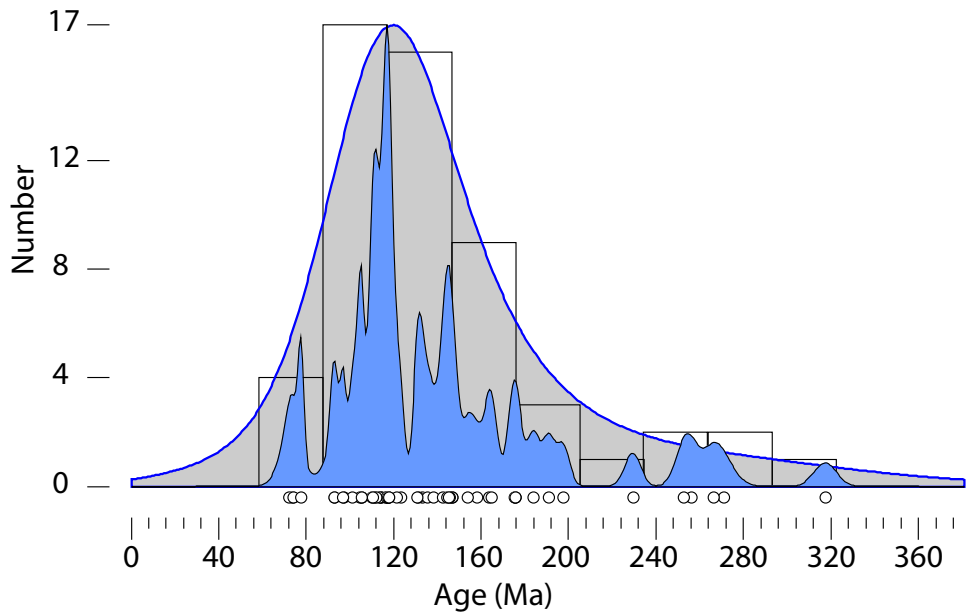
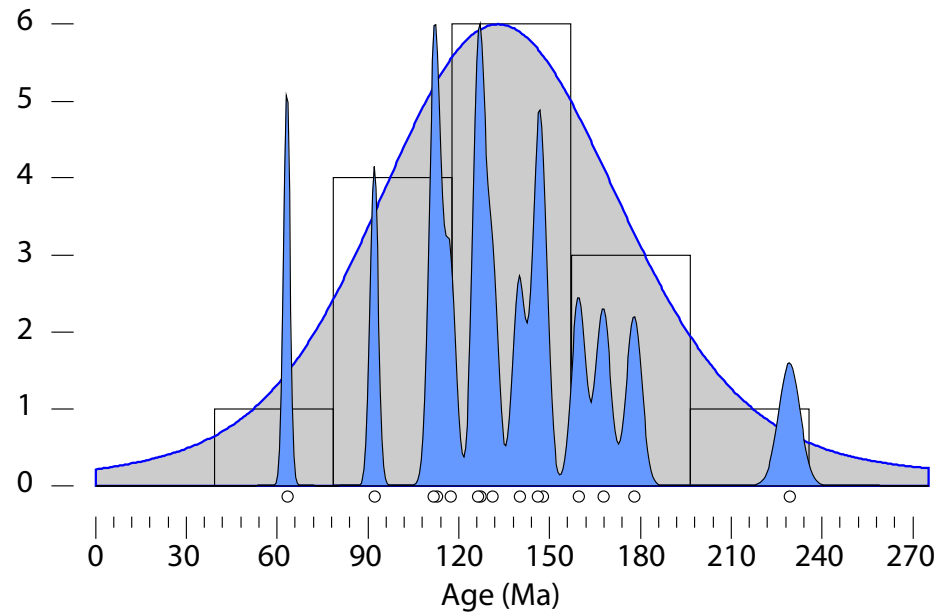


Figure 6.

Selenga detrital AHe (n=55)



Orkhon detrital AHe (n=15)



**Figure 7.**

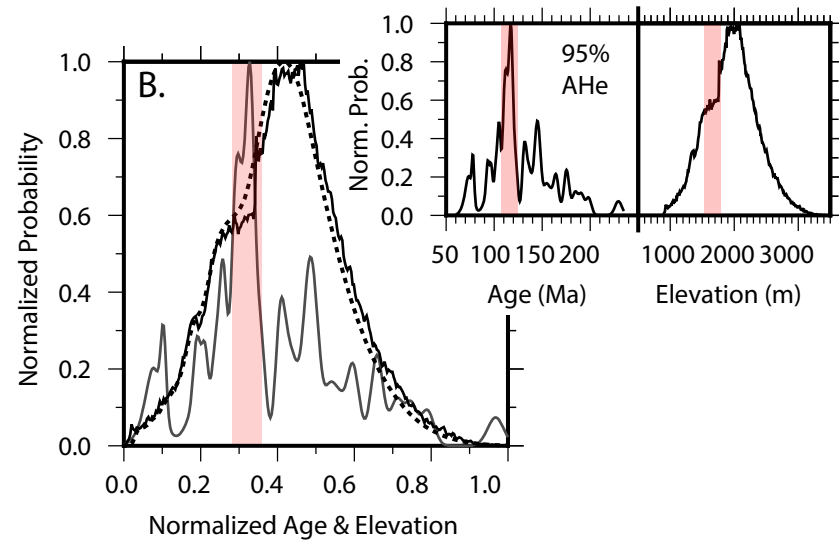
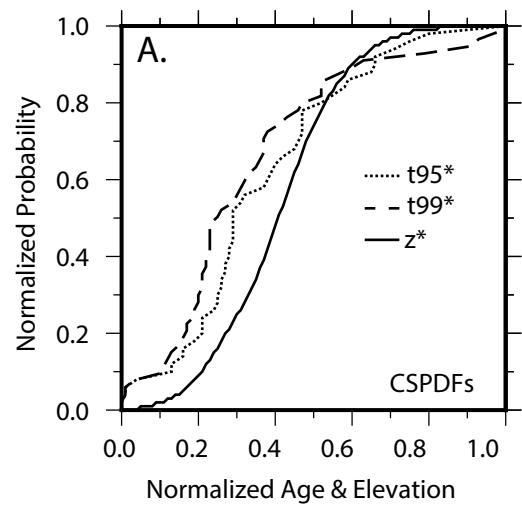




Figure 8.

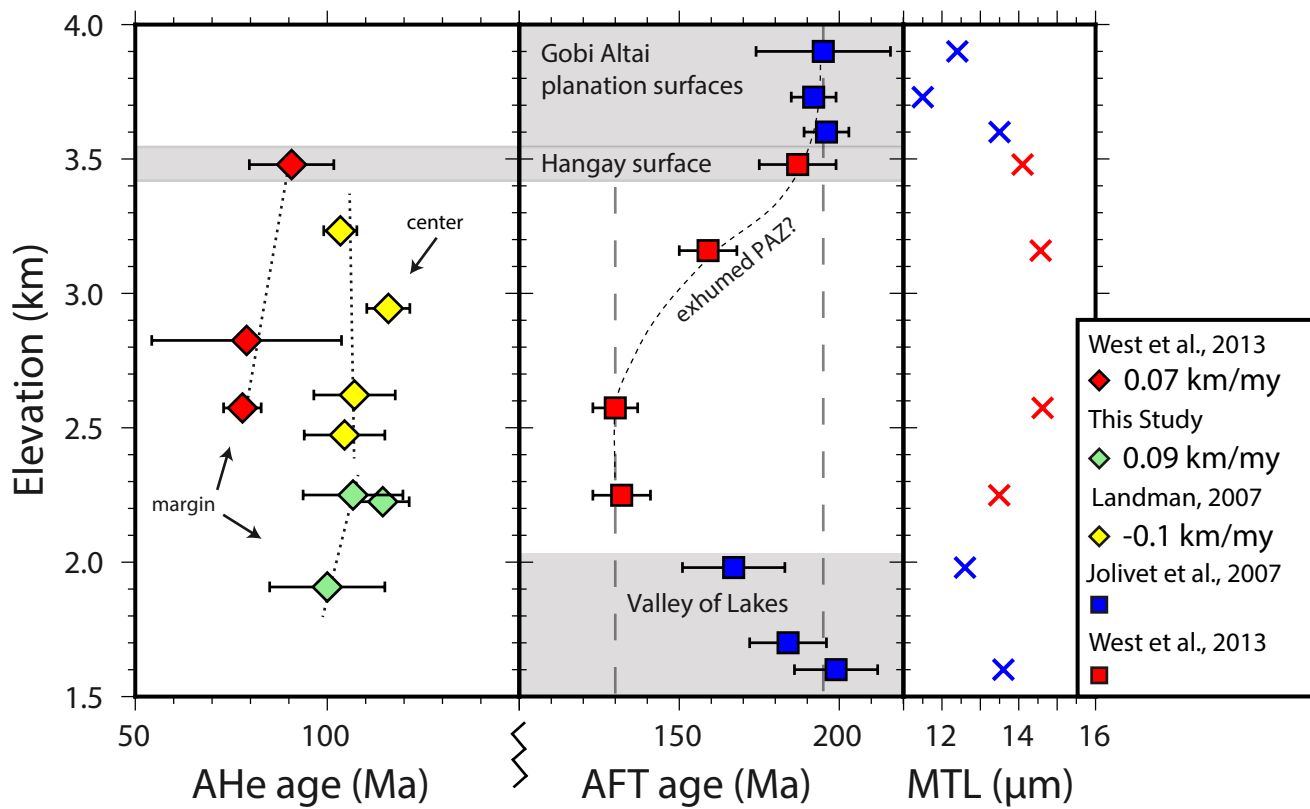


Figure 9.

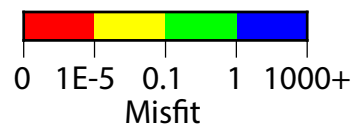
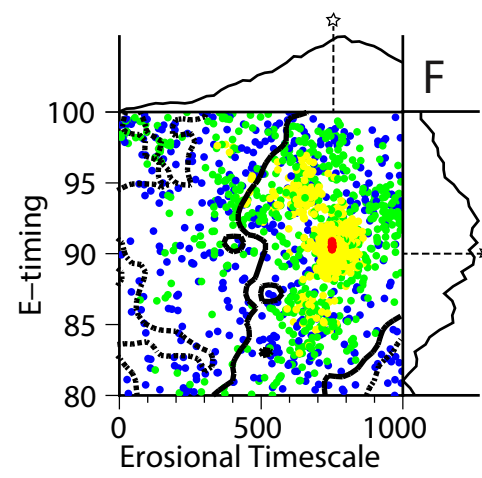
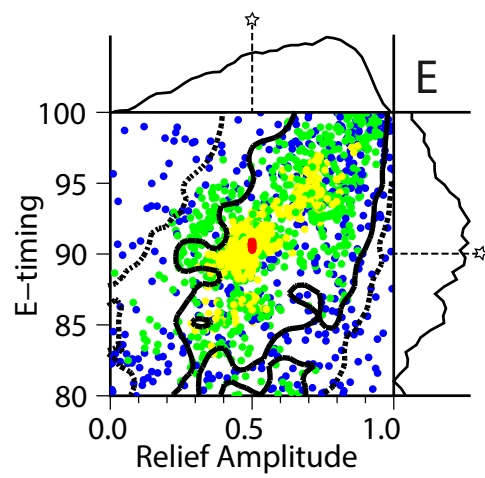
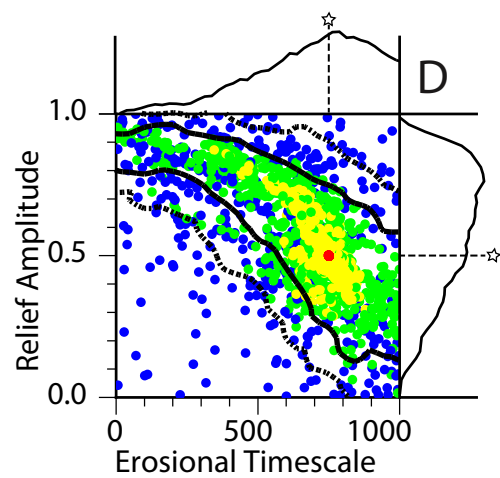
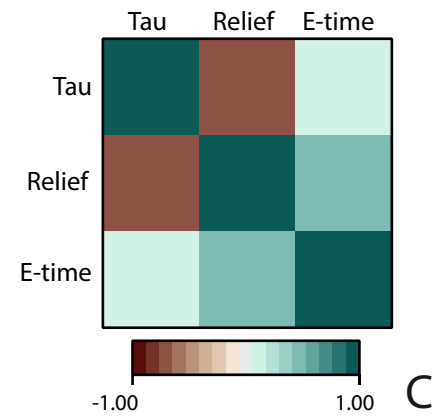
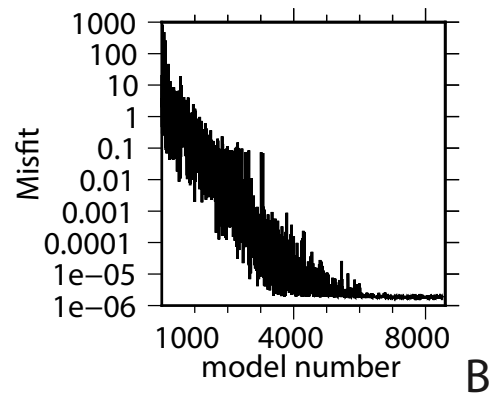
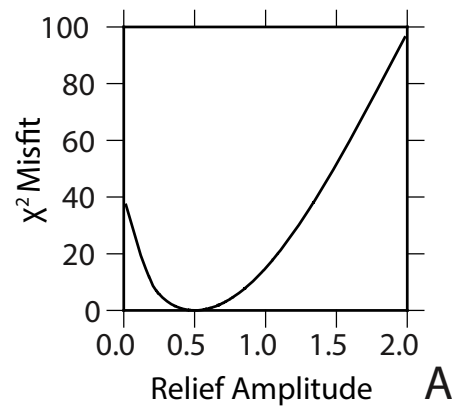
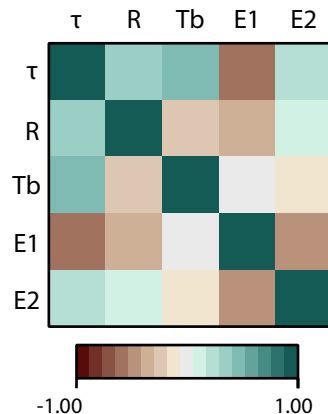
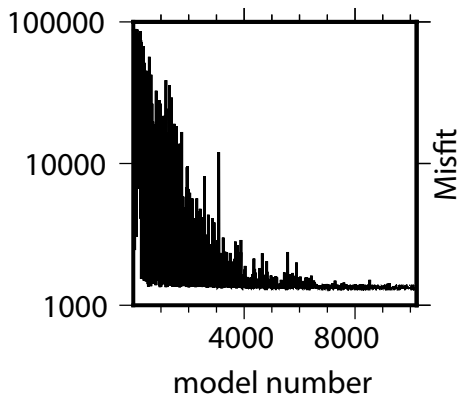
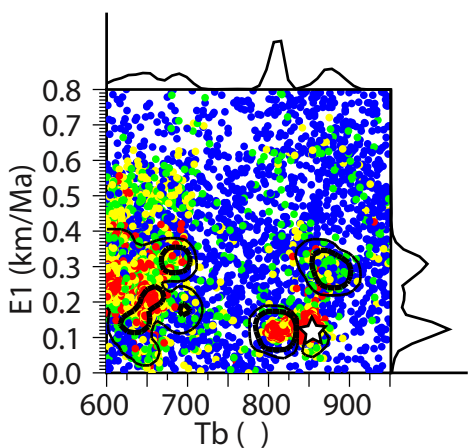
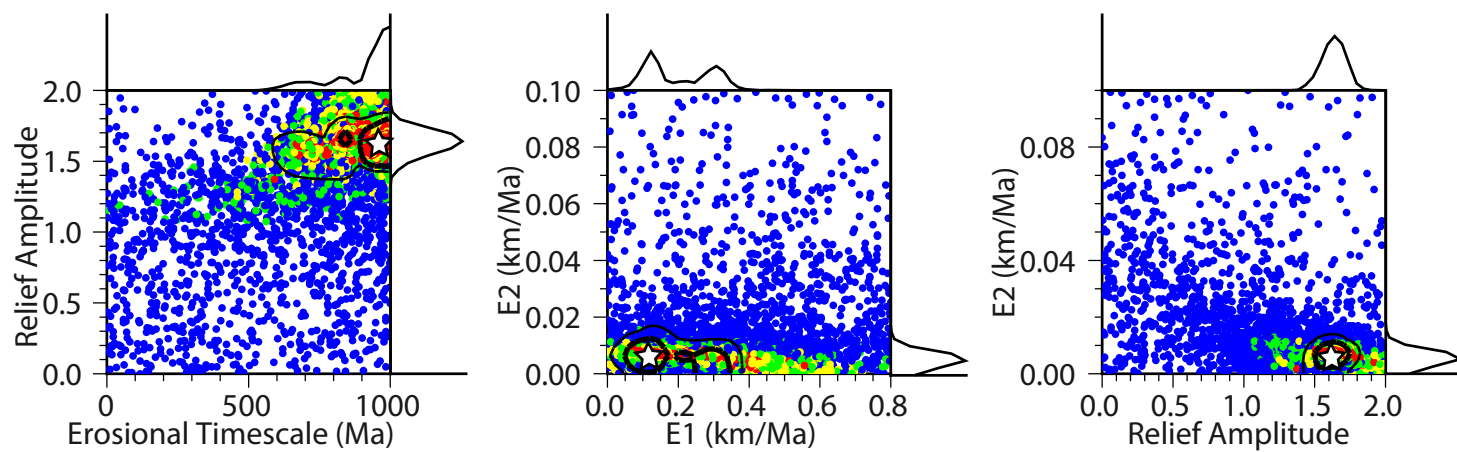


Figure 10.



—  $1\sigma$   
 —  $2\sigma$   
 ☆ lowest misfit

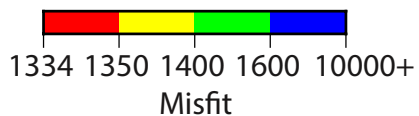




Figure 11.

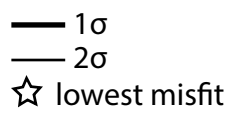
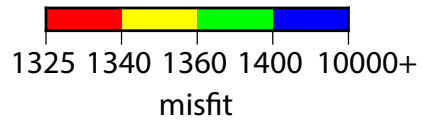
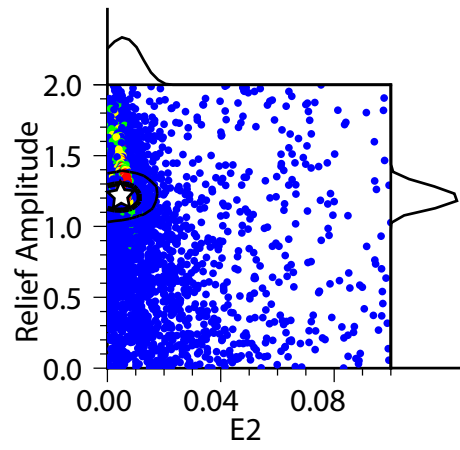
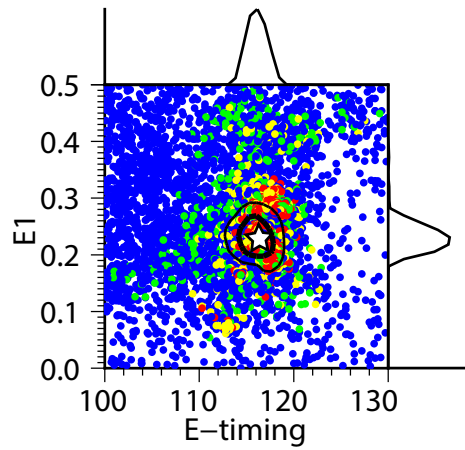
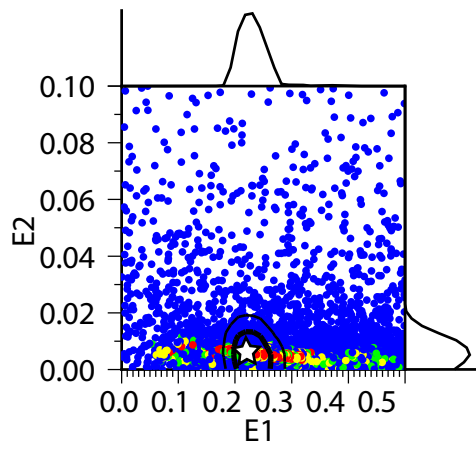
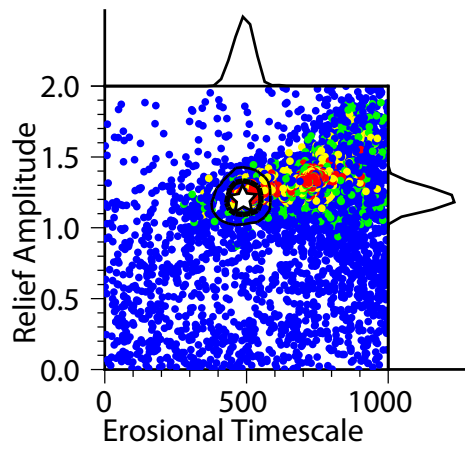


Figure 12.

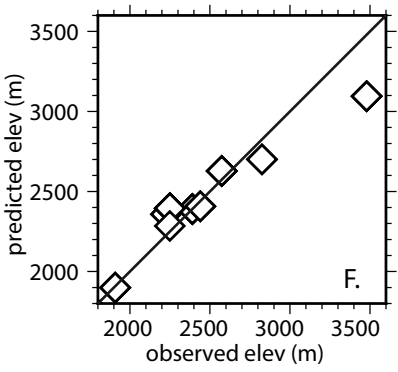
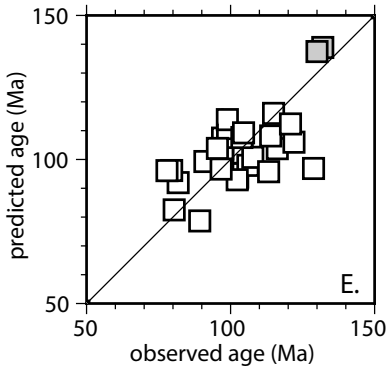
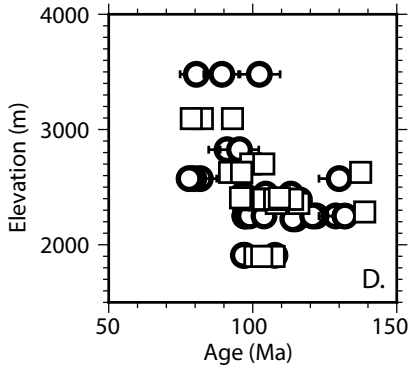
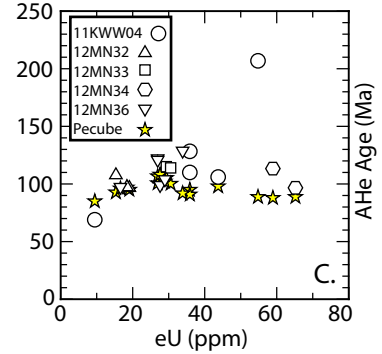
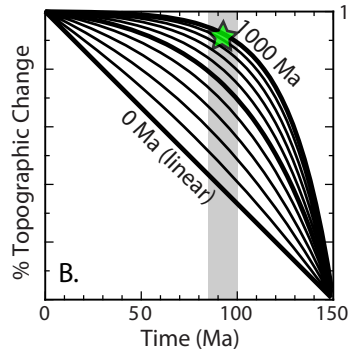
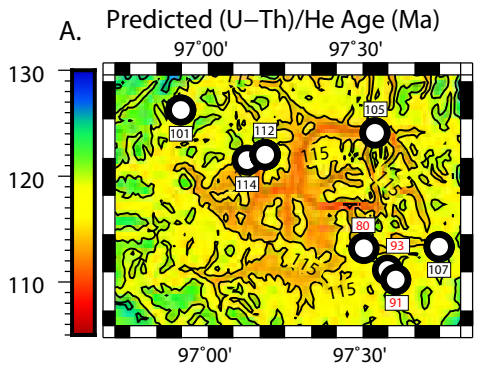


Figure 13.

Predicted model  
(U-Th)/He age (Ma)

Elev. (m)

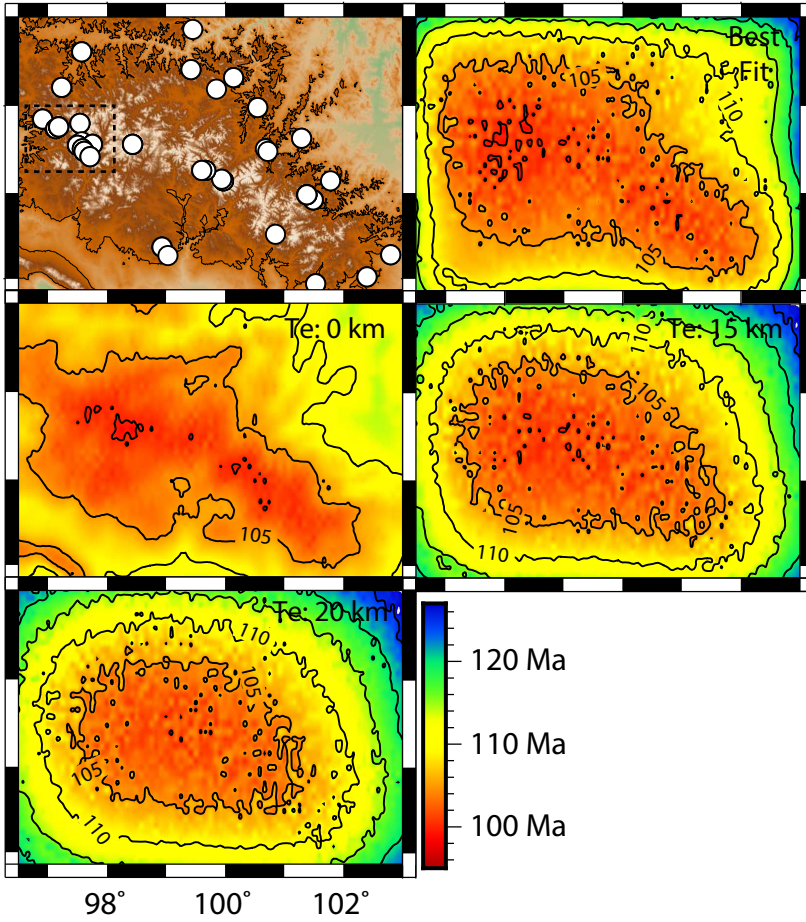
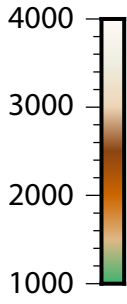
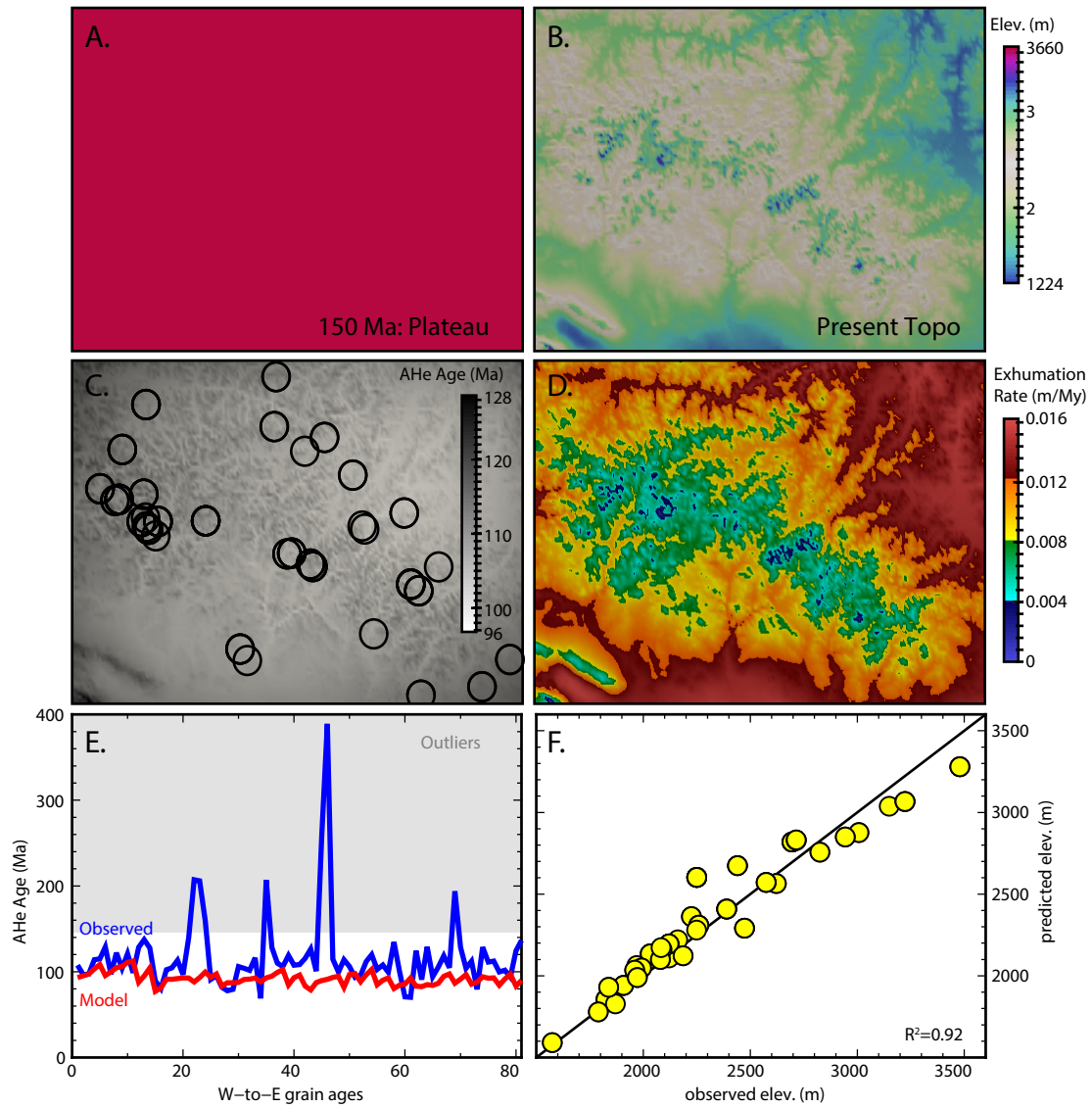




Figure 14.



1 **Relict topography within the Hangay Mountains in central Mongolia:**  
2 **Quantifying long-term exhumation and relief change in an old landscape**

3  
4 Kalin T. McDannell<sup>a,b,\*</sup>, Peter K. Zeitler<sup>a</sup>, and Bruce D. Idleman<sup>a</sup>

5  
6 <sup>a</sup>*Department of Earth & Environmental Sciences, Lehigh University, 1 W Packer Ave., Bethlehem, PA 18015, USA*

7  
8 <sup>b</sup>*Natural Resources Canada, Geological Survey of Canada, 3303 33 St NW, Calgary, AB T2L 2A7*

9  
10 Corresponding author: kalin.mcdannell@canada.ca

11  
12 **Key Points**

- 13 ■ New bedrock and detrital apatite (U-Th)/He cooling ages were determined for the Hangay  
14 Mountains and central Mongolia  
15 ■ Thermo-kinematic modeling suggests relief change in the Mesozoic with slow exhumation  
16 rates on the order of <20 m/My since the Cretaceous  
17 ■ Coupled Pecube-Neighborhood Algorithm modeling is successfully applied in a slowly  
18 eroding setting

19  
20 **Abstract**

21 The Hangay Mountains are a high-elevation, low-relief landscape within the greater Mongolian  
22 Plateau of central Asia. New bedrock apatite (U-Th)/He single-grain ages from the Hangay span  
23 ~70 to 200 Ma, with a mean of  $122.7 \pm 24.0$  Ma ( $2\sigma$ ). Detrital apatite samples from the Selenga  
24 and Orkhon Rivers, north of the mountains, yield dominant (U-Th)/He age populations of ~115  
25 to 130 Ma, as well as an older population not seen in the Hangay granitic bedrock data. These  
26 low-temperature data record regional exhumation of central Mongolia in the Mesozoic followed  
27 by limited erosion of <1-2 km since the Cretaceous, ruling out rapid exhumation of this  
28 magnitude associated with any late Cenozoic uplift. Apatite (U-Th)/He age-elevation patterns  
29 suggest long-term thermal stability of the upper crust, and thermal model inversions require late  
30 Mesozoic uplift and spatially variable exhumation driven by isostasy in concert with relief  
31 evolution to produce the observed cooling ages in the Hangay region. Regionally, modeling  
32 suggests reduction of topography in the Jurassic followed by rapid relief growth that was  
33 completed by the mid-Cretaceous. These results support Mesozoic topographic evolution and

34 relative stability of the landscape throughout the Cenozoic with very little subsequent  
35 exhumation. Alpine cirques and intact moraines are indicative of more recent, modest climate-  
36 driven erosion in the higher peaks of the western Hangay. These data reinforce the notion that in  
37 the absence of strong tectonic or climate forcing, erosion is limited and remnant landscapes can  
38 persist over 10s-100s of millions of years in a state of disequilibrium.

39 **Keywords:** Thermochronology, (U-Th)/He, Hangay, Mongolia, landscape evolution, Pecube

40

## 41 **1. Introduction**

42 The topographic evolution of landscapes offers a top-down perspective on understanding  
43 mountain-belt development through time. In recent decades, we have begun to understand that  
44 deformation, erosional unroofing, and climate can be coupled in active settings and that their  
45 system dynamics inherently regulate landscape geometries, [e.g., *Molnar and England, 1990;*  
46 *Raymo and Ruddiman, 1992; Zeitler et al., 2001*]. Studies of exhumation in active mountains  
47 have shown that orogenesis can take place quite rapidly at rates and durations consistent with  
48 plate convergence, and that surface processes can remove large relief rapidly [*Montgomery and*  
49 *Brandon, 2002*]. Conversely, ancient mountains and the records of their origins are often  
50 different from their modern counterparts, making the analysis of orogenic and topographic  
51 development a challenge.

52

53 Over orogenic timescales, the primary control on erosion and landscape evolution in active  
54 regions is tectonic uplift [e.g. *Koppes and Montgomery, 2009*]. In slowly eroding landscapes,  
55 where there is little tectonism, isostasy is the primary contributor to exhumation and under  
56 typical crustal and mantle density conditions reduction of surface topography requires significant

57 erosion [e.g. *Braun and Robert, 2005*]. The overall density structure of the lithosphere, in turn,  
58 controls the magnitude and distribution of isostatic adjustment to erosion, with less buoyant  
59 lithosphere demonstrating an inhibited isostatic response [e.g. *Fischer, 2002*]. Post-orogenic  
60 topography has been found to survive over extended timescales through various surface process  
61 interactions including landslide-erosion feedbacks [*Egholm et al., 2013*], and when sediment  
62 mobilization shear stresses are low and fluvial systems are transport-limited [*Baldwin et al.,*  
63 2003]. These phenomena allow topographic and geodynamic aberrations to persist over hundred  
64 million-year timescales, rather than disappear within tens of millions of years after tectonism  
65 ceases.

66

67 Clues to the exhumation and relief history of a landscape are held in the thermochronologic  
68 record of surface rocks across both short and long topographic wavelengths [*Braun, 2002;*  
69 *Mancktelow and Grasemann, 1997; Stüwe et al., 1994*]. Topography affects the upper-crustal  
70 thermal structure, with the severity of the thermal disturbance decreasing with depth and  
71 proportionally with the topographic wavelength [*Braun, 2002*]. At long topographic wavelengths  
72 (10s-100s of km) and low topographic relief, isotherms conform to the broad shape of the  
73 topography, whereas at very short wavelengths ( $\leq 10$  km) with high relief, low-temperature  
74 isotherms do not fully conform to topography. Rocks that are exposed at peaks have traveled a  
75 greater distance after crossing closure-temperature isotherms and therefore a cooling age  
76 increase with elevation is expected and provides a direct estimate of the exhumation rate for  
77 short topographic wavelengths [*Stüwe et al., 1994; Braun, 2002*]. Sampling at short wavelengths  
78 across steep valleys can be used to directly estimate the mean exhumation rate when higher  
79 temperature systems are used or in regions characterized by slow exhumation. An observed

80 positive age-elevation relationship (AER) becomes flattened with respect to steady-state  
81 topography if there has been relief growth, or steepened and even inverted if topographic relief  
82 has been reduced [Braun, 2002]. Therefore, short wavelength AERs are suitable for exhumation-  
83 rate estimation, while sampling long topographic wavelengths can provide estimates of relief  
84 change [Braun and Robert, 2005].

85

86 The Hangay Mountains of central Mongolia are high-elevation (>3500-4000 m), low-relief  
87 topography within the Asian continental interior. Broad, low-relief topographic surfaces that  
88 stand prominently above median continental base level are common features of continental  
89 interiors. How these apparently epeirogenic areas reach and maintain high elevations is puzzling  
90 because of their great distance from plate boundaries. Several studies suggest that the Hangay  
91 Mountains were uplifted recently in the mid-late Cenozoic [e.g. Cunningham, 2001; Windley and  
92 Allen, 1993; Yanshin, 1975] or rapidly within the past 5 Ma [Yarmolyuk et al., 2008]. Questions  
93 remain about the exact timing of surface uplift and whether the current topography is a youthful  
94 feature. To test this, inferences about topographic change and the erosion history of the upper  
95 crust can be made from spatial patterns in low-temperature thermochronology data. Here, we  
96 explore the ability of the apatite (U-Th)/He thermochronometer to constrain long-term, long-  
97 wavelength exhumation and relief evolution in the Hangay Mountains, where there is a lack of  
98 penetrative deformation, limited mass transport, and the regional climate has become  
99 increasingly arid from the Jurassic through the Cenozoic [Hendrix et al., 1992; Caves et al.,  
100 2014; Jolivet et al., 2015]. The elevated Hangay landscape itself thus shows no evidence for  
101 significant exhumation (more than 1-2 km) associated with any possible younger surface uplift,  
102 and likewise detrital age data show no evidence of such exhumation anywhere in the extensive

103 Selenga River catchment. This study suggests that the topography in the Hangay region is not  
104 young, but a relict feature that has persisted since the late Mesozoic. This work is part of a multi-  
105 institutional collaboration to study the development of high topography in intracontinental  
106 settings and the geodynamic and biologic implications of surface uplift in central Mongolia,  
107 specifically, addressing lithosphere-asthenosphere character and dynamics, Asian climate  
108 change, and climatic-tectonic forcing of landscapes [Ancuta, 2017; Carlson and Ionov, 2014;  
109 Caves *et al.*, 2014; McDannell, 2017; Meltzer *et al.*, 2012; Meltzer *et al.*, 2015; Sahagian *et al.*,  
110 2016; Smith *et al.*, 2016; Stachnik *et al.*, 2014; Wegmann *et al.* 2014].

111

## 112 **2. Regional setting and geologic history**

113 The Hangay Mountains are a high-elevation region in the Asian continental interior and offer the  
114 unique opportunity to study an old landscape in a setting affected by recent tectonism (fig. 1).  
115 The Hangay Mountains sit within the Mongolian Plateau (2.6 million km<sup>2</sup>) between the Siberian  
116 craton to the north and the Tarim and North China cratons to the south. The Hangay are also  
117 situated between the Altai Mountains (transpressional zone) and northern extensional zone of the  
118 Khövsgöl and Baikal rifts. The ranges in central Mongolia and southern Russia form the  
119 northernmost extent of the Central Asian Orogenic Belt (CAOB), which was a long-lived  
120 accretionary system, ca. 1000-250 Ma [Windley *et al.*, 2007]. The CAOB is composed of  
121 accretionary complexes including micro-continent blocks, volcanic arcs, back-arcs, and fore-  
122 arcs. This accretionary phase is believed to have lasted from Late Precambrian to Late Permian  
123 time when terrane suturing and closure of the Paleo-Asian Ocean was complete [Kroner *et al.*,  
124 2007; Lehmann *et al.*, 2010]. The Mongol-Okhotsk Ocean was located between the Siberian and  
125 Mongolian (Amuria) blocks during Paleozoic-Mesozoic time and closed along a scissor-like

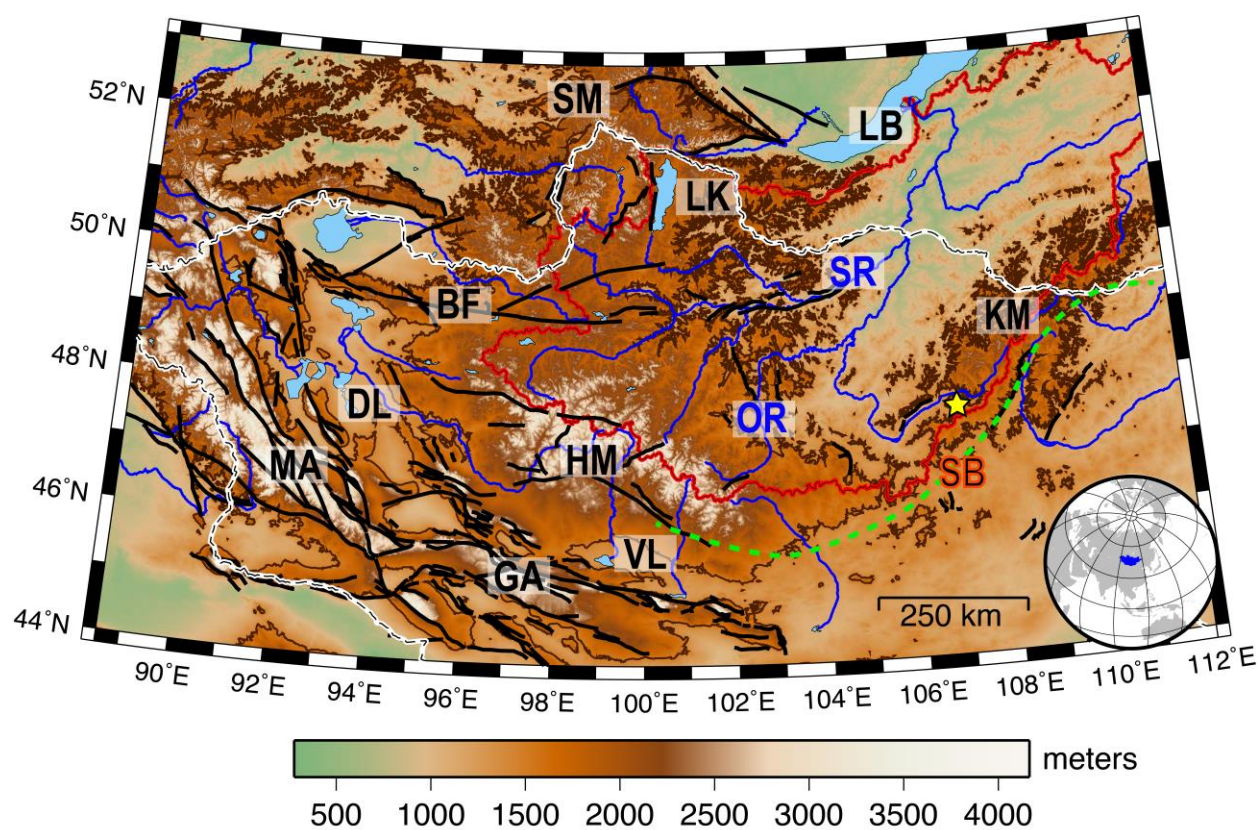
126 suture in the eastern CAOB [Tomurtogoo *et al.*, 2005]. The exact timing of closure is debated, as  
127 the Late Jurassic-Early Cretaceous appears to represent a period of rapid Mongol-Okhotsk  
128 closure based on the apparent clockwise rotation of Siberia during collision with the North China  
129 block [Cogné *et al.*, 2005], while Late Triassic-Early Jurassic exhumation was driven by  
130 Mongol-Okhotsk convergent margin tectonism [Yang *et al.*, 2015; Cunningham, 2017], followed  
131 by terminal collision in the Late Jurassic-Cretaceous. Yang *et al.* [2015] assessed the Jurassic-  
132 Cretaceous transition and propose that a brief (ca. 10 Ma), but significant collision occurred in  
133 the Late Jurassic-Early Cretaceous driven by collision of Siberia with the Kolyma-Omolon  
134 (Russia-Mongolia) block and terminal closure of the Mongol-Okhotsk seaway. Subsequently,  
135 there was a change in the regional stress field as regional compression ceased within the CAOB,  
136 allowing vast regions of over-thickened crust with high gravitational potential energy and  
137 elevated geothermal gradients to exist throughout central Asia [Cunningham, 2017]. Strike-slip  
138 system development and gravitational collapse of the upper crust gave way to the continental-  
139 scale extensional setting in East Asia accommodating India-Asia collision [Yin, 2010]. Seismic  
140 analysis in the Tugrug Basin (Valley of Lakes region) also supports a rapid change from  
141 orogenic thickening to collapse in the Late Jurassic [Johnson *et al.*, 2015]. Thermochronologic  
142 data from the Kyrgyz Tian Shan and Siberian Altai-Sayan confirm regional cooling during the  
143 initial stages of the Mongol-Okhotsk orogeny and contemporaneous Lhasa collision at about 150  
144 Ma, with orogenic collapse occurring afterwards around 100 Ma [Glorie and De Grave, 2016].

145

146 Mongolia is divided into two major geologic domains: a northern zone of Precambrian basement  
147 rocks and a southern zone of Paleozoic sedimentary and volcanic rock. The basement of the  
148 Hangay Dome is Archean to Early Proterozoic and is composed of metamorphic rocks



149 unconformably overlain by Cambrian through Devonian (meta)sedimentary units. The crystalline  
 150 and sedimentary rocks were intruded by Permian and Jurassic post-orogenic granitoids and  
 151 underwent deformation during major Late Paleozoic compression [Lehmann *et al.*, 2010]. The  
 152 granitoid massifs of the Hangay batholith yield zircon U-Pb crystallization ages of 260-242 Ma  
 153 [Yarmolyuk *et al.*, 2008] while the Khentiy batholith (abbrev. KM; fig. 1) is 220-200 Ma  
 154 [Yarmolyuk *et al.*, 2001]. Formation of the Hangay batholith is believed to be related to  
 155 magmatism associated with the Mongolian-Siberian craton collision [Zorin, 1999] or from post-  
 156 orogenic intraplate magmatism [Jahn *et al.*, 2000].  
 157



158  
 159 **Figure 1:** Regional map showing areas of high topography within Mongolia and southern Russia. The  
 160 mean elevation in this view extent is  $1500 \pm 563$  m and shows that the Hangay, Khövsgöl, Khentiy, and  
 161 Sayan Mountains (Russia) are a region of long-wavelength, high topography that has been dissected by  
 162 the Selenga River network that drains the northern flank of the Hangay into Lake Baikal. Note that the  
 163 deformation patterns vary regionally, i.e. the strong, large fault control in the Altai versus the diffuse,

164 smaller faults of the Hangay. The dark brown line denotes the 1500 m topographic contour. Regional fault  
165 systems are also shown; the sinistral Bulnai (BF) is the major strike-slip fault north of the Hangay  
166 separating the Sayan/Khövsgöl from the Hangay. The Mongolian (MA) and Gobi Altai (GA) ranges south  
167 of the Hangay are within a major transpressional fault system. The Siberian craton margin begins just  
168 north of the Sayan Mountains in the < 500 m elevation region (green) near the Mongolia-Russia border  
169 and Lake Baikal at ~53°N latitude. Blue lines are major permanent streams draining higher elevations and  
170 the red line denotes the Selenga River system drainage divide. Heavy white line is Mongolian political  
171 border. Green dashed line is approximate Mongol-Okhotsk Ocean suture after *Van der Voo et al.* [2015].  
172 Yellow star is Ulaanbaatar, the capital city. (MA=Mongolian Altai; GA=Gobi Altai; DL=Depression of  
173 Lakes; VL=Valley of Lakes; HM=Hangay Mountains; LK=Lake Khövsgöl; KM=Khentiyn Mountains;  
174 SM=Sayan Mountains; OR=Orkhon River; SR=Selenga River; LB=Lake Baikal; SB=Selenga basin).  
175 Major towns in Hangay region shown on figure 2.  
176

177 Gravity data along with seismic tomography and mantle xenolith information have allowed  
178 interpretation of the lithospheric structure below the Hangay-Khövsgöl region [*Ionov et al.*,  
179 1998; *Petit et al.*, 2002; *Zorin et al.*, 1990]. The lithosphere is thinner in Mongolia relative to the  
180 Siberian craton, and cratons to the south. Gravity anomalies are associated with localized  
181 lithospheric flexure from the current compressional stress regime [*Petit et al.*, 2002]. Deep ( $\geq 100$   
182 km) anomalous buoyant lithosphere is causing a long-wavelength, low-amplitude negative  
183 gravity signal with regional uplift of ~400 m, crustal velocity dampening, and a low-density  
184 lower crust-upper mantle beneath the Hangay, that results in a high amplitude gravity residual  
185 and localized uplift of ~700 m [*Petit et al.*, 2002; *Petit et al.*, 2008]. The uplifted high  
186 topography of the Mongolian Plateau (and central Mongolia) has mainly been described as a  
187 distal expression of the India-Asia collision [*Molnar and Tapponnier*, 1975; *Vassallo et al.*,  
188 2007]. However, other proposed uplift mechanisms include, Pacific plate subduction  
189 [*Yanovskaya and Kozhevnikov*, 2003], localized mantle plume activity [*Windley and Allen*,  
190 1993], asthenospheric upwelling and support [*Cunningham*, 2001; *Petit et al.*, 2008; *Tiberi et al.*,  
191 2008; *Chen et al.*, 2015], delamination of the lithospheric mantle [*Hunt et al.*, 2012], and  
192 thickened crust resulting from mafic underplating [*Stosch et al.*, 1995; *Petit et al.*, 2002].  
193

## 194 **2.1 Regional thermochronology**

195 During the Middle to Late Mesozoic, parts of central Asia were characterized by a topographic  
196 planation surface [e.g. *Cunningham*, 2001; *Hetzel et al.*, 2011; *Jolivet*, 2017]. The Hangay  
197 Mountains, Sayan-Baikal ranges, and the Altai systems all show preserved Jurassic through  
198 Paleogene planation surfaces at elevations ranging from a few hundred meters to up to 4000 m  
199 [*Cunningham*, 2001; *Jolivet et al.*, 2007; *Vassallo et al.*, 2007; *De Grave et al.*, 2009; *Jolivet et*  
200 *al.*, 2013; *West et al.*, 2013; *Glorie and De Grave*, 2016]. In the Hangay Mountains, Valley of  
201 Lakes, and Gobi Altai, rocks from these relict erosional surfaces have Jurassic-Early Cretaceous  
202 apatite fission-track (AFT) ages [*Jolivet et al.*, 2007; *Vassallo et al.*, 2007]. The similarity in  
203 AFT ages at peak summits in the Mongolian-Gobi Altai, Hangay, and the adjoining Valley of  
204 Lakes piedmont suggests that cooling below ca. 110°C occurred at roughly the same time across  
205 this region and these surfaces were at the same paleo-depth (see fig. 8; *Jolivet et al.* [2007]).

206  
207 Central Mongolia also shares similarities with mountains in neighboring southern Russia. The  
208 mountains around Lake Baikal record AFT ages between ~140-100 Ma and experienced rapid  
209 cooling in the Early Cretaceous, indicated by thermal-history modeling of AFT length  
210 distributions [*van der Beek et al.*, 1996; *Jolivet et al.*, 2009]. AFT ages from the Siberian Altai  
211 and Western Sayan of Russia are Jurassic to Cretaceous in age [*De Grave et al.*, 2009; *Jolivet et*  
212 *al.*, 2013; *Glorie and De Grave*, 2016]. Apatite fission-track thermal models for the Sayan  
213 suggest long-term erosion rates of 17.5 m/My, while <sup>10</sup>Be cosmogenic data suggest short-term  
214 (10<sup>5</sup> years) rates of 12-20 m/My [*Jolivet et al.*, 2013]. <sup>10</sup>Be cosmogenic data from basins in the  
215 eastern Hangay also show erosion rates between 12-20 m/My [*Hopkins*, 2012]. Short and long-

216 term rates are similar and at first-order imply an extended period of nearly constant, slow erosion  
217 since the Mesozoic across Mongolia and southern Russia.

218

### 219 **2.3 Hangay geomorphology**

220 Stratigraphy and basin analysis of the Tian Shan Mountains (see supplement for location) shows  
221 that the aforementioned Late Mesozoic tectonic reorganization and surface uplift shut off the  
222 monsoon system in central Asia, and aridification occurred through the Late Jurassic [*Hendrix et*  
223 *al.*, 1992; *Jolivet et al.*, 2015]. This region of central Asia has been arid through the end  
224 Mesozoic and Cenozoic and much of the aridification is attributed to the uplift of the Tibetan  
225 Plateau and corresponding intraplate mountain belts extending to the north towards the Siberian  
226 craton [*Molnar et al.*, 2010]. Observed shifts in regional isotopic aridity signatures support the  
227 timing of Hangay surface uplift to be at least as old as Oligocene, and Late Miocene for the Altai  
228 range [*Caves et al.*, 2014].

229

230 The ages of tilted sediments and volcanic rocks exposed on the flanks of the Hangay also support  
231 Oligocene doming and surface uplift of the Hangay, which is also broadly coincident with the  
232 initiation of regional volcanic activity [*Devyatkin*, 1975; *Cunningham*, 2001]. Basalt vesicle  
233 paleo-altimetry shows the surface of the Hangay may have been modestly uplifted by up to 1 km  
234 over the past ~10 Ma [*Sahagian et al.*, 2016]. Stratigraphic relationships between basalt flows  
235 and granitic bedrock document the existence of ~700 m of local paleo-relief in central Mongolia  
236 [*Smith et al.*, 2016], and this pre-existing topography is similar to the modern topography. Basalt  
237  $^{40}\text{Ar}/^{39}\text{Ar}$  ages constrain the minimum age of the Hangay landscape to the Oligocene [*Ancuta*,

238 2017], while  $^{14}\text{C}$  dating indicates that material in lacustrine deposits overlying basalt flows near  
239 Tariat (fig. 2 for location) are as young as ~5 Kya [Logachev *et al.*, 1982].

240

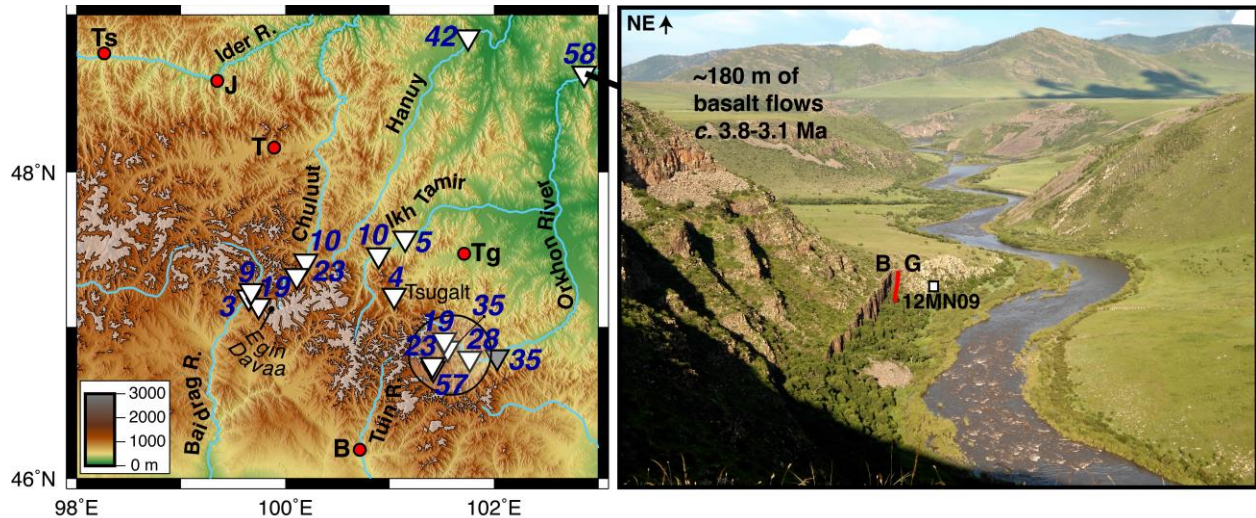
241 The central Mongolian fluvial network comprises alluvial streams with high sediment loads and  
242 limited transport ability due to many factors, including prolonged high aridity and spatially  
243 variable fluvial network integration. The Selenga River has a large drainage network (447,000  
244  $\text{km}^2$ ) that sources the entire northern flank of the Hangay and most of central Mongolia and  
245 flows north into Lake Baikal, contributing a large volume of the lake water supply. The Orkhon  
246 River is one of the major Selenga tributaries flowing out of the glaciated eastern Hangay (fig. 1  
247 and fig. 2). The river network has modestly eroded most of the northern Hangay since minor late  
248 Cenozoic surface uplift. West *et al.* [2013] recognized two major river profile knickpoints near  
249 the northern and southern Hangay margins at ~2500 m elevation and estimate that up to 1-1.5 km  
250 of total erosion (relative to reconstructed “pre-incision” remnants at high elevations) have  
251 occurred below these knickpoints and in other areas in the eastern Hangay.

252

253 Geomorphic observations coupled with  $^{40}\text{Ar}/^{39}\text{Ar}$  dated whole-rock basalt stratigraphy [Ancuta,  
254 2017] allow us to calculate minimum incision rates in the Hangay region (fig. 2). The Orkhon  
255 River headwaters show rates of ~20 m/My through the late Pliocene to Holocene, while Orkhon  
256 headwater tributaries show late Pliocene through Holocene rates of ~30-60 m/My. At the Orkhon  
257 River waterfall (Ulaan Tsutgalan) basalts are ~700 Ka in age and yield incision rates of ~35  
258 m/My. The northern flank of the Hangay shows rates of ~10 m/My in 13-14 Ma basalts exposed  
259 along the Ikh Tamir River, a tributary of the Orkhon. The Chuluut River valley, to the west,  
260 shows variable incision rates of 10-23 m/My over the past ca. 8-10 Ma. Basalt incision rates are



261 similar to the aforementioned cosmogenic erosion rates in adjacent drainages and those estimated  
 262 at Egiin Davaa in the central Hangay of ~25-77 m/My over the past 9 Ma [Smith *et al.*, 2016].  
 263 Basalt damming of river valleys in the past few million years establish that isolated flows caused  
 264 accelerated incision (fig. 2), but overall these rates are comparable to those seen in old orogens  
 265 such as the Appalachians [e.g. Matmon *et al.*, 2003; McKeon *et al.*, 2014].

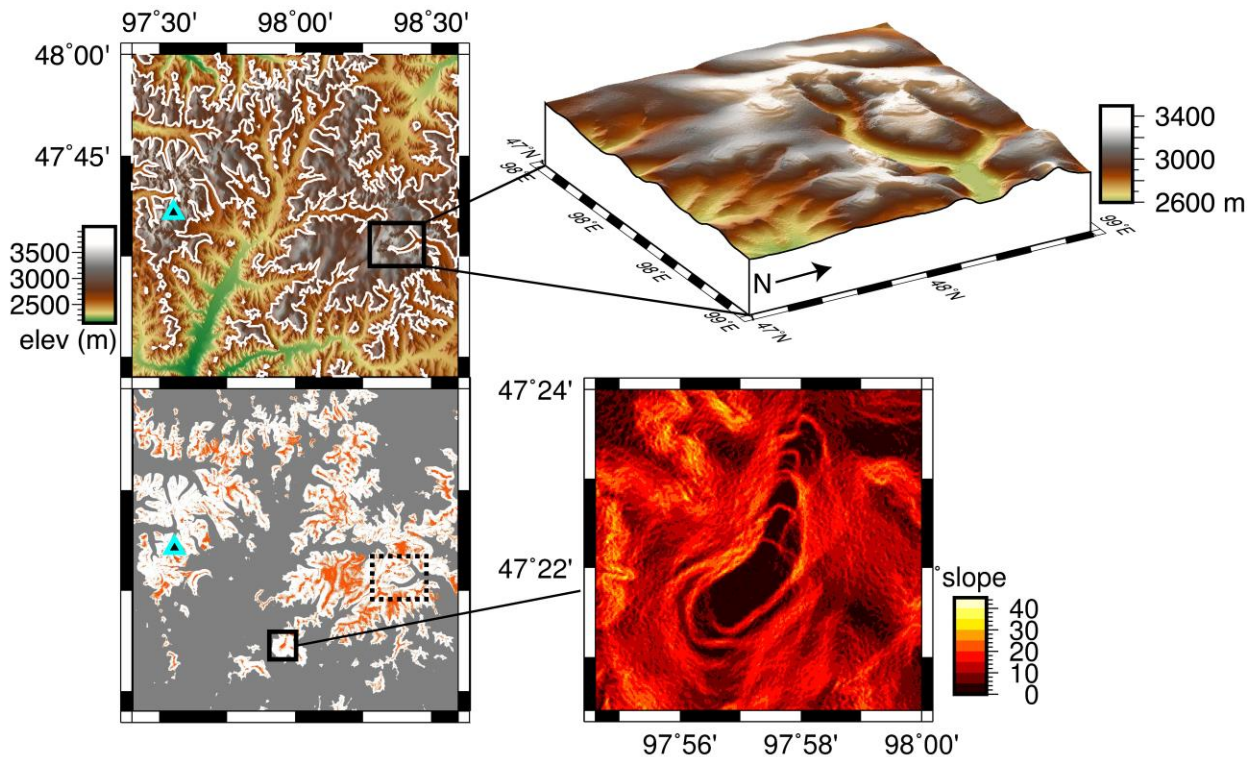


266  
 267 **Figure 2:** The eastern Hangay Mountains and major rivers (blue lines) with high elevation areas glaciated  
 268 in the LGM shown in gray. River incision estimates at locations (triangles) from basalt age data presented  
 269 in *Ancuta* [2017]. Numbers shown are in incision rates in m/My. Circled area in the southeast is the  
 270 headwaters of the Orkhon River. Gray triangle is the Orkhon waterfall location (Ulaan Tsutgalan). Photo  
 271 on the right shows a canyon location along the Orkhon River, at lower elevations in the Selenga River  
 272 basin, where the higher incision rates (~58 m/My) are due to local basalt flow damming (~180 m total  
 273 thickness) over the past 3 m.y. Red dots mark major towns in the area. B = Bayankhongor; J = Jargalant;  
 274 T = Tariat; Tg = Tsetserleg; Ts = Tosontsengal. Photo: The contact between granitic basement and the  
 275 basalt flows is shown by the red line in the photo. Apatite (U-Th)/He sample 12MN09 is from the granite  
 276 bedrock [mean (U-Th)/He age of ~325 Ma].  
 277

278 The Hangay Mountains were glaciated in the Pleistocene during the Last Glacial Maximum  
 279 [Lehmkuhl *et al.*, 2004]. Evidence for this exists in the form of well-defined cirques and  
 280 preserved moraine deposits. There are currently no permanent alpine glaciers in the Hangay, but  
 281 cryoplanation features, patterned ground, and other glacial features exist at high elevations and  
 282 advocate a more recent climate-driven erosion signal in the past few million years. Cryoplanation  
 283 terraces are typically just below relict planation surfaces at high elevations (fig. 3) [West *et al.*,

284 2013]. *Lehmkuhl* [1998] estimates the equilibrium line altitude (ELA) of the last glacial  
 285 maximum (LGM) to be at ~2700-2800 m elevation. Current ELA estimates are ~3700 m  
 286 [*Lehmkuhl and Lang, 2001*], which is ~1000 m higher than the Pleistocene ELA and at fairly  
 287 high elevations relative to the highest peaks of the Hangay (~4000 m), thereby limiting the  
 288 potential for modern glaciation. The highest peaks show evidence of cryoplanation terraces down  
 289 to 3100-3300 m elevation, while most glacial processes below 2600 m in the Hangay are limited  
 290 in extent and mainly restricted to frost shattering of bedrock [*Lehmkuhl and Lang, 2001*].  
 291 Presumably, glaciation in the western Hangay near Otgontenger (fig. 3) has recently created  
 292 more dramatic topographic relief, which is almost twice the relief observed in lower elevations  
 293 near the Selenga River headwaters (see suppl. figure S2).

294



295  
 296  
 297  
 298  
 299

**Figure 3:** Imagery showing the regional topography near the highest Hangay peak, Otgontenger Uul (triangle). The areas outlined in white are the ELA for the LGM at 2800 m elevation. The image below is of the same area as above but showing elevations >2800 m (gray area is <2800 m) and areas with slopes  $\leq 5^\circ$  (orange). Enlarged digital elevation model (DEM) inset (top right, looking  $240^\circ$  at  $20^\circ$  inclination)

300 shows example of high elevation relict planation surface and associated cryoplanation features east of  
301 Otgontenger. Bottom panel is a slope map of another such area to the south with a flat, relict surface and  
302 cryoplanation terraces. See *West et al.*, [2013] for other examples.  
303

### 304 **3. Methodology**

#### 305 **3.1 Apatite (U-Th)/He thermochronology**

306 Granitic bedrock and detrital sediments were collected for apatite (U-Th)/He (AHe) analysis  
307 throughout central Mongolia. Igneous bedrock samples went through standard procedures for  
308 rock crushing, sieving (<250 microns), Frantz magnetic splitting, and heavy-liquid separation  
309 using lithium polytungstate and methylene iodide. Unbroken, symmetric apatite grains without  
310 visible inclusions were selected under a high-power petrographic microscope at 250-300X  
311 magnification. Samples were digitally photographed in order to record their 3D morphology for  
312 determination of alpha-correction factors using a cylindrical geometry. Grains were then placed  
313 in small Nb tubes whose ends were crimped and loaded into the extraction system in the Lehigh  
314 University noble gas laboratory for analysis following conventional methodology (see below) or  
315 underwent continuous ramped heating treatment [*Idleman et al.*, 2018; *McDannell et al.*, 2018].  
316  $^4\text{He}$  and the  $^3\text{He}$  spike were measured using a Balzers bakeable quadrupole mass spectrometer  
317 designed for UHV operation, fitted with both Faraday and electron-multiplier detectors. For  
318 helium extraction, a double-vacuum resistance furnace was used for heating, and an all-metal  
319 sample dropper permits multiple samples to be loaded for sequential analysis in the resistance  
320 furnace. Helium evolved from heated samples was purified in an all-metal extraction line  
321 pumped by an ion pump during routine operation as well as a 70 l/s turbo-molecular pump with a  
322 small rotary backing pump used during bake-out. An SAES GP50 getter in the extraction line  
323 removes active gases, while a smaller SAES getter in the mass spectrometer volume is used to  
324 minimize hydrogen loads. Reservoirs containing a  $^3\text{He}$  spike and a  $^4\text{He}/^3\text{He}$  standard are attached



325 to the line behind all-metal pipettes while two temperature-stabilized capacitance manometers  
326 provide the precise, accurate pressure measurements needed for spike preparation (the extraction  
327 line  $^4\text{He}$  blank is  $1 \times 10^{-16}$  moles or less).  $^4\text{He}$  was measured by isotope dilution, using a  $^3\text{He}$  spike,  
328 and also by manometric peak-height comparison against a mass-discrimination standard.  
329 Generally these approaches agree to better than 1% and the dual calibrations provide an internal  
330 crosscheck. Over periods spanning the analysis of sample batches, the  $^4\text{He}/^3\text{He}$  ratio for the  
331 standard was precise to within 0.3%, with a value of about 0.795 (the true  $^4\text{He}/^3\text{He}$  ratio of  
332 standard is 1.000). For the current spike preparation, the size of a typical spike is  $4 \times 10^{-13}$  moles.  
333 Following helium extraction, U, Th, and Sm measurements were obtained from the University of  
334 Arizona in the laboratory operated by Dr. Peter Reiners, where samples were dissolved, spiked,  
335 and analyzed using isotope-dilution ICP-MS [Reiners and Nicolescu, 2006]. U, Th, and Sm were  
336 measured on the same aliquots of apatite that were used for He determinations, eliminating any  
337 uncertainties contributed by weighing errors and sample heterogeneity. A mean age of  $31.85 \pm$   
338  $0.24$  Ma (2 SE,  $n=78$ ) for the Durango apatite age standard has been acquired over repeated  
339 experiments in the Lehigh noble gas laboratory. McDowell *et al.* [2005] obtained a direct  
340  $^{40}\text{Ar}/^{39}\text{Ar}$  reference age of  $31.13 \pm 0.42$  (2 SE) for Durango apatite.

341

### 342 **3.2 Detrital apatite (U-Th)/He modeling**

#### 343 **3.2.1 Inference of detrital cooling age distribution components**

344 The BayesMixQt program allows Bayesian inference of probability distributions regarding the  
345 number of component age distributions from a set of individual mineral cooling ages and their  
346 associated errors under Gaussian or Skew assumptions [Jasra *et al.*, 2006]. More simply, it  
347 allows identification of discrete age components (mixture modeling) in a larger age distribution

348 and is well suited for the heterogeneity often encountered in detrital age datasets. The modeling  
349 infers the proportion of each individual distribution that contributes to the total distribution as  
350 well as the parameters that define each distribution (i.e. mean and standard deviation). The  
351 approach implements Reversible Jump Markov chain Monte Carlo methods that employ an  
352 iterative sampling scheme and allow changes in the problem-space dimensionality (i.e.  
353 component distributions). This approach requires defining prior and proposal distributions for the  
354 dataset and allows a “burn-in” phase for exploratory sampling of the model space, which is used  
355 to infer the component distribution parameters (i.e. post-burn-in phase). Refer to *Jasra et al.*  
356 [2006] for a more complete overview of mixture modeling.

357

### 358 **3.2.2 Catchment-averaged erosion rates and topographic relief histories from detrital data**

359 The age distribution of detrital mineral cooling ages provides a proxy for the erosional history of  
360 mountain catchments [e.g. *Avdeev et al.*, 2011; *Brewer et al.*, 2003]. The range of cooling ages  
361 can also provide information about erosion timing and magnitude. The detrital age range for a  
362 catchment is proportional to the time needed to erode the total relief in the source region [*Brewer*  
363 *et al.*, 2003; *Ruhl and Hodges*, 2005], while narrow or broad age spread is interpreted as rapid or  
364 slow erosion rate, respectively [*Stock and Montgomery*, 1996]. Assuming uniform erosion and a  
365 positive trend AER, the observed elevation distribution in a catchment should produce a  
366 predicted age probability density function (PDF) that matches the hypsometry (fig. 4) [*Brewer et*  
367 *al.*, 2003; *Ruhl and Hodges*, 2005; *Stock et al.*, 2006]. If there is non-uniform erosion in a  
368 catchment then the predicted age PDF will be out of phase with the hypsometric curve or have  
369 multiple peaks corresponding to the areas of the catchment that are being more heavily eroded

370 (fig. 4) [Stock et al., 2006; Ehlers et al., 2015]. Equations (1-3) after Ruhl and Hodges [2005]  
371 describes this relationship:

372 (1)

$$PDF = \frac{1}{\sigma t_m \sqrt{2\pi}} \exp \left[ -\frac{1}{2} \left( \frac{t - t_m}{\sigma t_m} \right)^2 \right]$$

373

374 Where  $t$  is the PDF of the age,  $t_m$  is the measured age with the analytical uncertainty,  $\sigma$ . The  
375 synoptic probability function (SPDF) is the summation of all individual grain PDFs multiplied  
376 by the reciprocal of the number of detrital grains normalized to unity.

377 (2)

$$SPDF = \frac{1}{n} \sum_{i=1}^n PDF (i)$$

378 The shape of the SPDF should mimic the hypsometric curve if bedrock erosion scales with  
379 surface area and the cooling ages accurately reflect the eroded sediment signal. The cumulative  
380 synoptic probability function (CSPDF) represents the probability that the age takes on a value  
381 less than or equal to  $t$ , the PDF of the cooling age. The CSPDFs are normalized hypsometric  
382 curves of elevation,  $z^*$ , and cooling age,  $t^*$ , and assuming uniform erosion, should overlap.

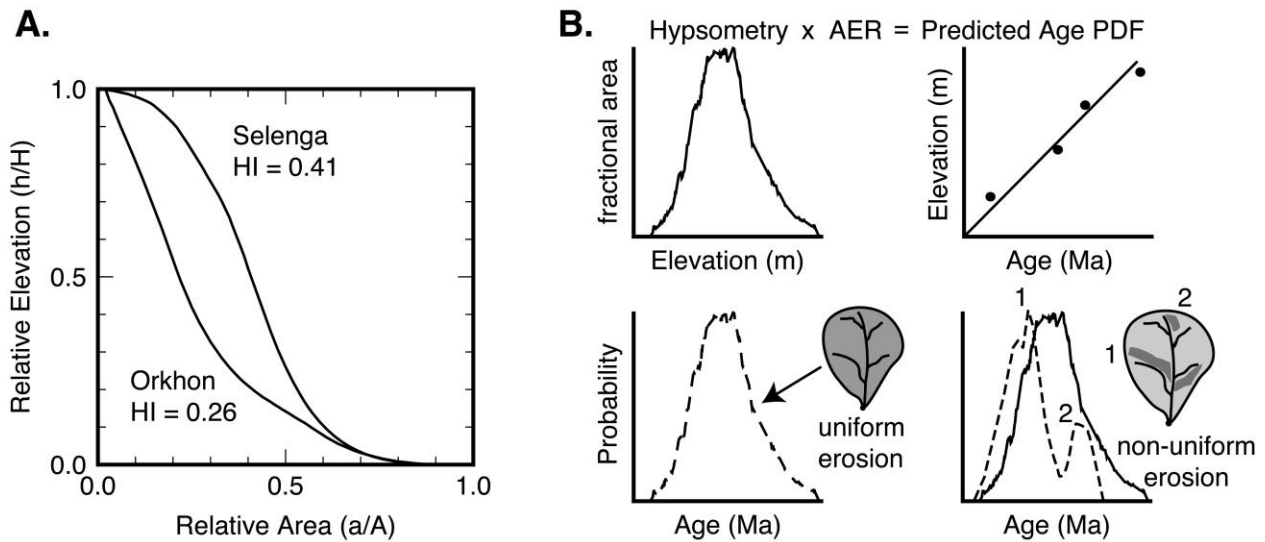
383 (3)

$$CSPDF = \sum_{i=0}^t SPDF (j)$$

384

385

386



387  
 388 **Figure 4:** (A) Hypsometry of the Selenga and Orkhon River sub-catchments sampled for detrital AHe  
 389 (see figure 5 for locations; section 5 for discussion). (B) Schematic diagram illustrating the relationship  
 390 between detrital thermochronometer data and the hypsometry of a catchment given an assumed positive  
 391 age-elevation relationship where cooling ages should match the hypsometric curve if erosion is uniform,  
 392 i.e. all points on the topography produce cooling ages that correspond to the basin AER. If there is non-  
 393 uniform erosion, then the elevations on the landscape contributing sediments will affect the SPDF curve  
 394 accordingly, modified after *Stock et al.* [2006].  
 395

### 396 3.3 Methods: Coupled Pecube-Neighborhood Algorithm modeling

397 Pecube [*Braun, 2003*] is a finite-element thermo-kinematic model that solves the 3D heat  
 398 transport equation in a crustal block with the allowance of a time-variable surface boundary  
 399 condition (topography) including the effects of isostasy. Pecube predicts thermochronometric  
 400 ages for crustal scenarios involving erosional or fault-driven exhumation. In our Pecube  
 401 inversions we adopt spatially constant material properties for the crust (table 1) and a sub-region  
 402 of central Mongolia is modeled as a single uplifting block, as the entire Hangay and  
 403 thermochronology dataset coverage are too large to model efficiently (see section 5.4 for location  
 404 and discussion). A SRTM digital elevation model of central Mongolia resampled to 1 km  
 405 resolution was used as the topographic input. The conventional volume diffusion model of  
 406 *Farley* [2000] has typically been used for AHe age prediction, and in the case of grains with low  
 407 (<20-30 ppm) effective uranium (eU) content [*Flowers et al., 2009*], and/or rapid cooling this

408 model is satisfactory and does not require more sophisticated age prediction models that account  
409 for compositional or radiation damage effects [e.g. *Flowers et al.*, 2009; *Gautheron et al.*, 2009].  
410 Since radiation damage tends to suppress partial He loss, the closure temperature varies in  
411 proportion to the eU and cooling rate, thus contributing to the observed apatite cooling age  
412 dispersion commonly seen in slowly cooled settings. The *Flowers et al.* [2009] radiation damage  
413 model was incorporated for age prediction within Pecube for modeling of our Mongolia data  
414 similar to code used in *Fox et al.*, [2014]. Pecube and previous applications are reviewed  
415 thoroughly in *Braun et al.* [2012]. Here we summarize some of the main features relevant to this  
416 study.

417

418 During a Pecube model inversion, the use of a two-step *Neighborhood Algorithm* (NA) inverse  
419 approach is employed, where during the sampling stage the multi-dimensional prior model space  
420 is efficiently sampled to find the best-fitting parameter combinations that produce the lowest  
421 user-defined misfit between observed and predicted data [*Sambridge*, 1999a]. The appraisal  
422 stage then allows robust measures of parameter resolution to be extracted in the form of  
423 Bayesian marginal posterior probability density functions (PPDF) during resampling of the  
424 model ensemble [*Sambridge*, 1999b]. During the sampling stage an initial model ensemble is  
425 randomly generated using the prior parameter range (assumed uniform distribution) of the  
426 Pecube variables. The misfit is assessed and Voronoi cells are created about nearest neighbor  
427 models that are subdivided after successive iterations as the algorithm focuses on regions of  
428 lower misfit by resampling the previous iteration. We employed an objective function or  $\chi^2$   
429 misfit of the form:

430

(4)

$$\mu = \sum_{i=1}^n \left( \frac{m_i - o_i}{\sigma_i} \right)^2$$

431  
432 Where  $\mu$  is the misfit value,  $n$  is the number of data, and for each datapoint  $i$ ,  $o_i$  is the observed  
433 age,  $m_i$  is the model age, and  $\sigma_i$  the observed age error. During the NA appraisal stage the entire  
434 sampling-stage ensemble is resampled to gain Bayesian estimates of parameter values and assess  
435 the lowest misfit via the Likelihood function,  $L$ , to assess the likelihood of different model  
436 predictions, given in the simplified form as:

$$437 \tag{5}$$

$$438 L = \exp\left(-\frac{1}{2}\chi^2\right)$$

439 In the case of  $\chi^2$  misfit, the simplified form of the  $\log(L)$  is equal to -0.5 multiplied by the misfit  
440 value [Glotzbach *et al.*, 2011]. The motivation for examining individual model misfit during the  
441 appraisal stage is that the lowest misfit can be misleading, for example, the lowest misfit may be  
442 identified for an individual parameter, but in the multi-dimensional case the overall misfit is a  
443 combination of several parameters where the identified best fit may have a single parameter  
444 value that is associated with a large misfit due to trade-offs in multi-dimensional space. Posterior  
445 probability accounts for this, because although it is a function of all parameters, it may be  
446 integrated over one or more parameters to examine the probability of that parameter in relation to  
447 the other parameters in the form of a 1-D marginal PPDF curve. Parameters plotted as 2-D  
448 marginal PPDFs examine potential correlative tradeoffs between different parameters. In the case  
449 of a purely Gaussian PPDF the results are interpreted as a mean/mode value at the peak  
450 maximum, and in the case of a skewed PPDF, the mode is at the maximum probability peak of  
451 the PPDF curve.

452

453 The sampling stage has typically been performed iteratively but here we use the MPI-enabled  
454 parallelized version of the code that does away with ‘formal iterations’ and instead of the misfit  
455 being assessed at the end of an iteration, it is continuously assessed during the inversion, leading  
456 to more efficient algorithm performance [Rickwood and Sambridge, 2006]. The number of  
457 iterations, the number of models in each iteration step, and the resampling rate all control the  
458 NA-sampler stage and influence the NA search. Although there are no specific rules for these  
459 configurations, a lower resampling rate allows faster convergence, albeit with the danger of  
460 prematurely converging on local minima, while a greater resampling rate allows more thorough  
461 exploration of the ensemble space but is slower to converge. Generally, inversions with a greater  
462 number of free parameters require a larger number of iterations to converge on the best fitting  
463 parameter combination.

464

465 The relief amplitude,  $R$ , in Pecube is fairly simplistic as it assumes the planform geometry of the  
466 topography does not change, only the amplitude varies, i.e. valleys and ridges do not migrate  
467 laterally [Valla *et al.*, 2010; van der Beek *et al.*, 2010]. This assumption is justified in  
468 equilibrated landscapes with low erosion.  $R$  is defined as the ratio between the relief amplitude  
469 ( $\Delta h_i$ ) when rocks passed through the closure isotherms and the modern-day relief amplitude  
470 ( $\Delta h_0$ ). Where: (6)

$$R = \frac{\Delta h_i}{\Delta h_0}$$

471

472 According to the model definition, where  $R = 1$  is the modern topography, when  $R = 0$  the initial  
473 topography is a plateau (no relief) at the highest elevation; for  $R < 1$  relief has grown from the

474 past to present; while for  $R > 1$  relief has decreased from past to present [Beucher *et al.*, 2012;  
 475 Valla *et al.*, 2010]. The erosional (or relief change) timescale,  $\tau$ , is a function that describes how  
 476 relief evolves through time, either in an exponential or linear fashion (see fig. 12), where 0 is a  
 477 linear change in relief in the model between time steps (equation 7). When values are highly  
 478 positive, relief change will take place rapidly at the model onset, and if  $\tau$  is highly negative the  
 479 relief change will take place close to present day [Beucher *et al.*, 2012].

480 (7)

$$481 \quad \Delta h_t = \Delta h_0 + \left[ (R - 1) \Delta h_0 \frac{1 - e^{-\left(\frac{t\tau}{t_f^2}\right)}}{1 - e^{-\left(\frac{\tau}{t_f}\right)}} \right]$$

482  
 483 Pecube-NA inversions have been applied successfully to high-relief regions that have  
 484 experienced relatively high exhumation rates and recent relief development such as the European  
 485 Alps [van der Beek *et al.*, 2010] and Southern Alps [Herman *et al.*, 2010]. There has been  
 486 varying success in applying this approach to determine relief histories accurately and difficulties  
 487 are attributed to incomplete sampling of topography at multiple wavelengths, and the  
 488 insensitivity of low-temperature thermochronometers to rapid topographic change or high  
 489 exhumation rates [e.g. Valla *et al.*, 2010; Reverman *et al.*, 2012]. Valla *et al.* [2010] explored the  
 490 efficacy of estimating denudation rates and relief histories using the Pecube-NA inversion and  
 491 the resolving power of the AFT and AHe low-temperature thermochronometers. They suggest  
 492 that settings where relief development is approximately two to three times higher than  
 493 background exhumation rates, or where background exhumation rates are generally low, as being  
 494 more suitable for relief-change investigations. Central Mongolia is a setting where the latter is  
 495 likely to be true throughout the latest Mesozoic and Cenozoic.



496

#### 497 **4. Apatite (U-Th)/He thermochronology results**

##### 498 **4.1 Bedrock (U-Th)/He data**

499 Granitoid bedrock samples were collected across the Hangay and areas to the north (fig. 5; suppl.  
500 table S1 for data). We dated 106 single-crystal aliquots of apatite (44 bedrock samples) and also  
501 report 12 multi-grain aliquots (5 bedrock samples) dated at Lehigh University during pilot  
502 Mongolia sampling presented in *Landman* [2007]. For mean age calculations, bedrock ages that  
503 were older than reported Hangay U-Pb ages of ~250 Ma were discarded as outliers. However,  
504 there is a lack of age control for granitoids to the north, and those found in the Altai in southwest  
505 Mongolia have older zircon U-Pb populations spanning 289-317 Ma and 350-398 Ma [*Cai et al.*,  
506 2015], considerably older than the ~240-250 Ma granites in the Hangay. This allows for the  
507 possibility that there are older granites to the north that exhumed prior to those in the Hangay.

508

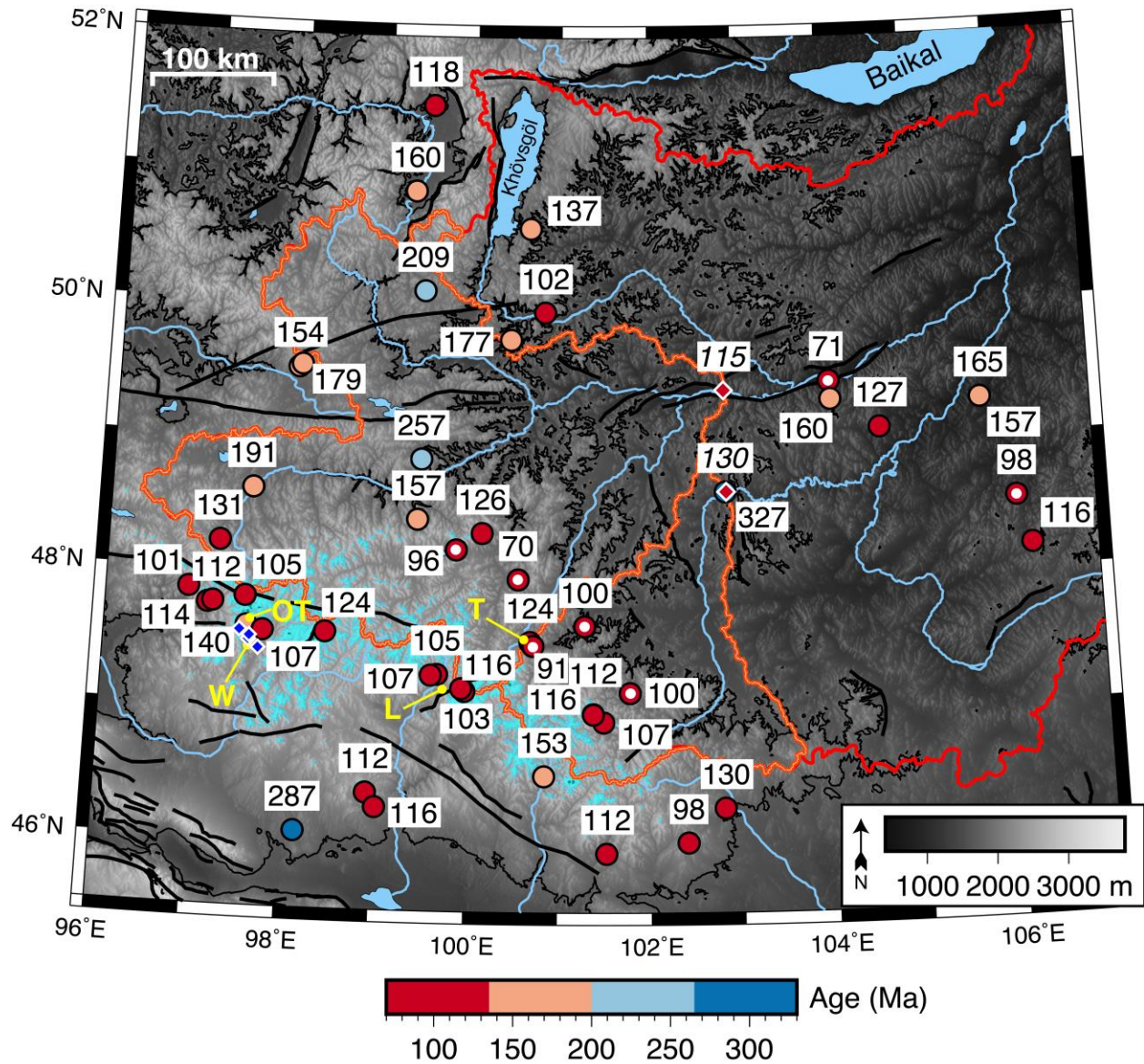
509 Age dispersion in slowly-cooled settings is a common issue [e.g., *Fitzgerald et al.*, 2006;  
510 *McDannell et al.*, 2018] that is often attributed to factors such as fluid and mineral inclusions  
511 [e.g. *Farley*, 2000], U-Th zonation [e.g. *Farley et al.*, 2011], and radiation damage effects [e.g.  
512 *Shuster et al.*, 2006]. We ran a number of replicate grains for each sample in order to identify  
513 any dispersion, and it does occur in a few samples. The convention is to analyze 2-5 replicate  
514 single grains for each sample; however, robust averaging methods are difficult to justify for  
515 small sample sizes less than 10 grains due to the effects of age dispersion and outlier treatment  
516 [e.g. *Vermeesch*, 2010]. Additionally, because factors such as U content, radiation damage, and  
517 grain size control kinetic properties and He retentivity [*Farley*, 2000; *Shuster et al.*, 2006], each  
518 grain from the same rock is in effect a separate thermochronometer, so statistical averaging is not

519 always warranted. We report arithmetic mean ages only for the purpose of an overview of  
520 regional age patterns. Mean ages are not used in thermal modeling (see later sections), as it is a  
521 requirement to model single grains because each analyzed grain is unique in its kinetic properties  
522 and slow cooling amplifies these kinetic effects.

523

524 Single-grain ages replicate well within the central Hangay and cluster around ~100-120 Ma at  
525 various elevations with a few exceptions, while data outside the Hangay show greater variation  
526 and generally older ages (fig. 5). The cooling ages from the north flank of the range are  
527 marginally younger than elsewhere in the higher elevations (<100 Ma), which coincides with the  
528 focus of modern erosion and precipitation leading to peak height asymmetry in the Hangay [*West*  
529 *et al.*, 2013]. This regional cooling age pattern is similar to that of the Dabie Shan in China  
530 [*Reiners et al.*, 2003] where significant age differences exist between the range core and flanks,  
531 with a progressive younging of cooling ages toward the mountain interior. Modeling of these  
532 data may be explained by a twofold decrease of topographic relief over the past ~100 m.y. to  
533 produce observed age patterns [*Braun and Robert*, 2005].

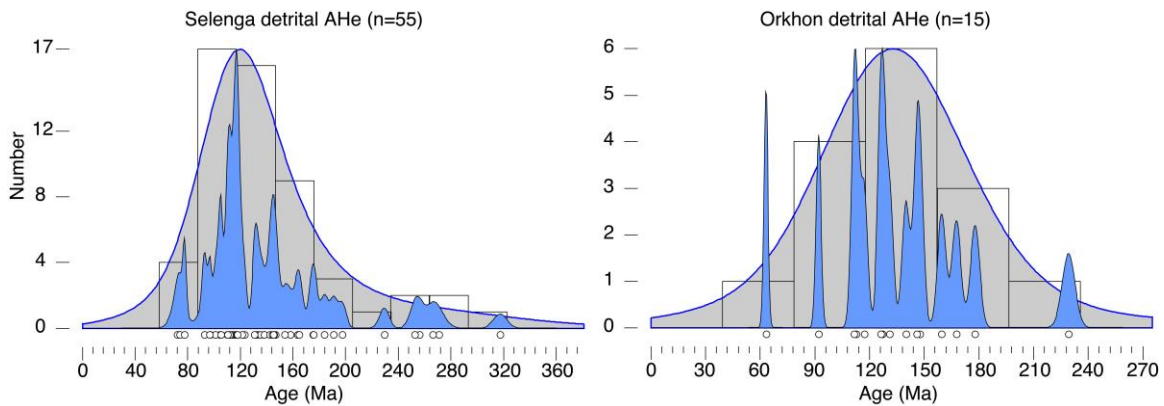
534



535  
 536 **Figure 5:** Granitic-bedrock mean AHe ages across the Hangay Mountains and north-central Mongolia  
 537 colored by age. The majority of cooling ages in the Hangay are ca. 100-120 Ma, with a slightly younger  
 538 grouping <100 Ma on the north flank (red/white center). Off the Hangay, ages are similar, albeit with  
 539 greater scatter and an older component greater than ca. 120 Ma. Detrital sample locations are shown as  
 540 diamonds (mean age in italics). The red line shows the Selenga watershed and sub-catchments with  
 541 respect to detrital samples for the Selenga and Orkhon are the orange lines. Points tagged in yellow are  
 542 AHe/AFT transect (W) of *West et al.* [2013] shown in blue diamonds, transect (L) of *Landman* [2007]  
 543 near Egiin Davaa, and transect (T) discussed with figures 7 and 8. OT = Otgontenger Uul. Grayscale 90 m  
 544 DEM with 1700 m contour to mark higher elevations above the regional background and onset of  
 545 ‘regional knickpoint elevation zone’ discussed in text and with fig. 7. Glaciated high elevations areas  
 546 shown in cyan blue, derived from the ELA during the LGM from *Lehmkuhl* [1998]. Major faults from  
 547 *Tomurtogoo* [1999] geologic map of Mongolia shown by heavy black lines. See supplement for full age  
 548 dataset.  
 549

550 **4.2 Detrital (U-Th)/He data**

551 The lower reaches of the Orkhon and Selenga Rivers were sampled to survey regional detrital  
552 apatite cooling ages (suppl. table S2 for data). The corresponding watersheds of the sampled  
553 locations are shown in figure 5. The motivation for detrital dating was to establish the age  
554 distribution that may be expected from bedrock ages, and to assess any dominant subsets. There  
555 was also an added motivation to determine if younger detrital ages were expressed that were  
556 missed by bedrock sampling. The Selenga and Orkhon Rivers (fig. 6) show similar age  
557 distributions with dominant peaks at ~115-120 Ma for the Selenga and a broad peak centered at  
558 ~130 Ma for the Orkhon (this central value is likely controlled by the low number of data).  
559



560

561 **Figure 6:** Selenga and Orkhon River detrital apatite (U-Th)/He cooling age populations shown by kernel  
562 density estimator (KDE) (smooth, gray envelope) and probability density functions (PDF) (shaded blue)  
563 from DensityPlotter [Vermeesch, 2012] using a Gaussian kernel and adaptive bandwidth (varied based on  
564 local data density). White dots show individual grain ages for the datasets. The y-axis is number of grains.  
565

566 **5. Modeling and interpretations**

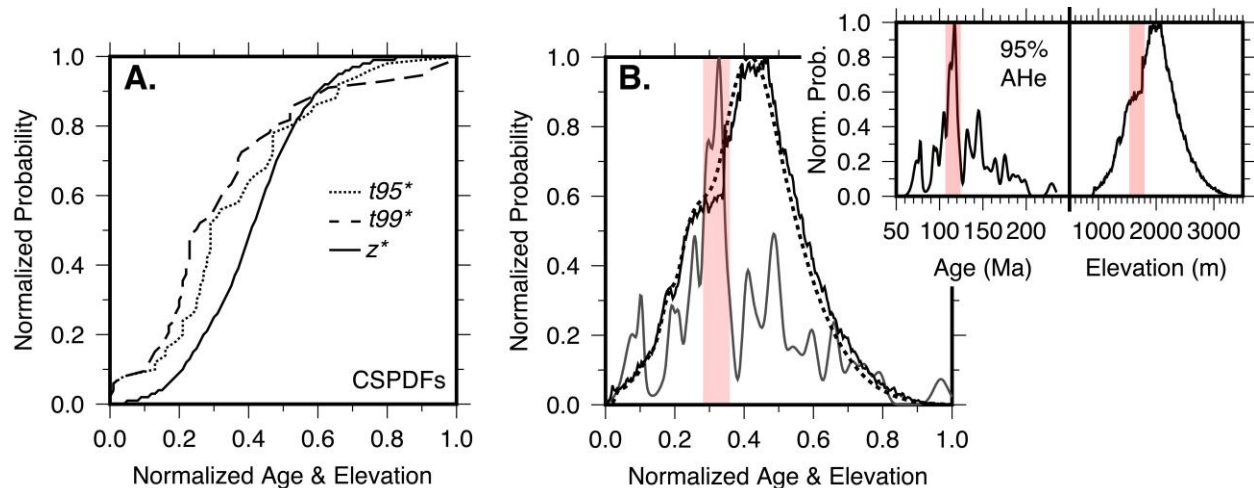
567 **5.1 Detrital apatite (U-Th)/He modeling**

568 Inference of the probability distribution of the number of detrital cooling age components was  
569 performed via BayesMixQt using Reversible Jump Markov-Chain Monte Carlo methods [Jasra  
570 *et al.*, 2006]. There are two major age components identified in the Selenga River sample with an

571 expected model mean of  $124 \pm 29$  Ma, representing 83% of the detrital population and an older  
572 component at  $227 \pm 51$  Ma, representing 17% of the population (200,000 iterations, post burn-  
573 in). The Orkhon sample has very few grains and is less resolved, but mixture modeling reveals a  
574 single component maximum posterior peak at  $131 \pm 29$  Ma, showing overall agreement between  
575 both rivers. The Selenga detrital population contains a few dates that may reflect the end of  
576 CAO B orogenic exhumation, while the majority of grains are from the last major exhumation  
577 event in the early Cretaceous during Mongol-Okhotsk suturing. The notable outcome from the  
578 detrital dating is that the area supplying sediment to these two locations contains an older age  
579 component that is not reflected in the Hangay bedrock samples, implying that the older ages are  
580 potentially coming from bedrock in the lower reaches of the catchments or that older cooling  
581 ages are sourced from glacially-eroded relict surfaces.

582

583 The hypsometry of the Selenga and Orkhon catchments relative to the detrital sample locations  
584 are quite different (fig 4). Both drainage basins have been glaciated (fig. 5), but the glaciation is  
585 limited in extent to only the highest elevations, compared to the overall basin areas. Based on the  
586 shape of the hypsometric integral, the Orkhon basin would be “mature or old,” with the majority  
587 of the catchment area at low elevations, while the Selenga would represent a younger stage of  
588 development [Strahler, 1952]. Nevertheless, caution is required during interpretation because the  
589 influence of tectonics or fluvio-glacial processes, along with basin size and tectonic activity can  
590 render basin hypsometry non-unique [Brocklehurst and Whipple, 2004].



591  
 592 **Figure 7:** (A) Normalized CSPDF curves of Selenga detrital ages (dashed lines,  $t^*$ ) and catchment  
 593 elevations (solid line,  $z^*$ ) for the Selenga River, using 95% and 99% of the detrital dataset, after *Ruhl and*  
 594 *Hodges* [2005]. (B) SPDF curves for normalized age (gray) and elevation (solid black line) distributions  
 595 with inset age and elevations (upper right). Dashed line in (B) is the ‘ideal’ age SPDF obtained from  
 596 inverting the observed age SPDF and hypsometric curves with respect to the regional AER from the  
 597 northern Hangay (figure 5, transect labelled T). Small inset panels show ages for 95% of the detrital AHe  
 598 dataset and the elevations in the Selenga sub-catchment and red shading shows the dominant mismatch in  
 599 age/elevation from the ideal age SPDF, see text for details.  
 600

601 Figure 7 show plots of detrital cooling age PDFs from equation 1-3 after *Ruhl and Hodges*  
 602 [2005]. To minimize the mismatch between normalized age and elevation curves due to  
 603 uncertainty in cooling ages, both the 95% and 99% detrital SPDF were used to construct the  $t^*$   
 604 CSPDFs, which effectively removes a small component of the older age signal. The  $CSPDF_{t^*}$   
 605 curves are slightly offset from the  $CSPDF_{z^*}$  curve for the Selenga basin, suggesting non-uniform  
 606 erosion and a preferential erosional zone at elevations between ~1600-1800 m in the northern  
 607 Hangay landscape. *Whipp et al.* [2009] showed through 3D thermal modeling that an increase in  
 608 relief amplitude (with a constant minimum elevation) causes a shift in the detrital age population  
 609 towards older ages relative to steady-state relief, whereas a relief decrease would have an  
 610 opposite trend. This is directly linked to the higher or lower effective denudation rate between  
 611 each respective relief change scenario. The mismatch/shift towards younger ages in fig. 7B may



612 be in line with the relief-decrease age shift of *Whipp et al.* [2009]. The Orkhon basin curves are  
613 not shown due to the limited number of dated grains.

614

615 We solve for the expected uniform erosion AER by dividing the observed detrital PDF by the  
616 hypsometry to obtain the slope of the ideal AER to match the hypsometry. This produces a  
617 predicted slope of 0.068 that is then compared to a bedrock age-elevation transect on the north  
618 flank of the Hangay in the Selenga sub-catchment (see fig. 5 for location), which yields a slope  
619 of 0.060 (dashed predicted age SPDF curve in fig. 7B). Another short bedrock age transect from  
620 the valley floor to the Orkhon headwaters cirque yields a slope of 0.059. Near Otgontenger Uul,  
621 the highest elevation peak in the glaciated interior of the Hangay, age-elevation transects are  
622 shown in figure 8 using our data and cooling ages from *West et al.* [2013], *Jolivet et al.* [2007],  
623 and *Landman* [2007]. Here, AER slopes are greater but still similar to the predicted and  
624 measured AER slopes in the Selenga basin. The slight mismatch in the PDF curves could be due  
625 to:

626 1) Sampling bias or outlier ages: The Selenga basin sources not only the Hangay, but lower  
627 elevations to the north that have a slightly older, albeit scattered, cooling age signal and  
628 therefore are eroding more slowly than the Hangay. Bias could be introduced from the  
629 dating process itself or be naturally occurring if a higher proportion of ‘younger’ Hangay  
630 sediments were being supplied to the lower reaches of the basin. Naturally occurring bias  
631 may be a reflection of alpine cirque cutting and higher erosion along steeper slopes of the  
632 Hangay. There is also the possibility of sampling other Mesozoic-Paleozoic bedrock and  
633 older, recycled sediments. If this were the case, it would seem that this is a fairly small  
634 proportion of dated grains. Alternatively, some of these slowly-cooled apatites could be

635 cooling age outliers that are skewing the age PDF; this situation is apparent in the 95%  
636 CSPDF<sub>t\*</sub> curve, which more closely matches the hypsometry by removing only the oldest  
637 ages from the detrital population.

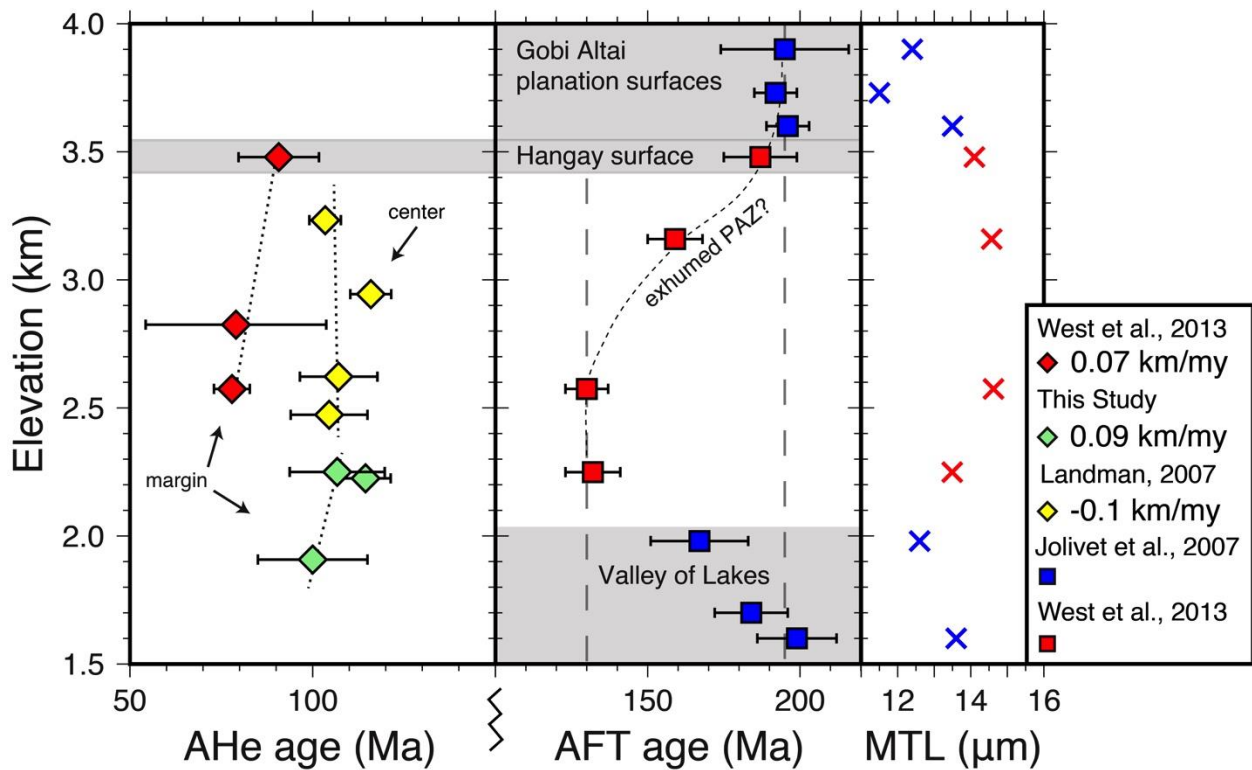
638 2) Detrital under-sampling: The Selenga CSPDFs are reminiscent of those presented by  
639 *Ruhl and Hodges* [2005] for the Marsyandi trunk stream in Nepal where there is also  
640 departure of the CSPDF<sub>t\*</sub> from the elevation range. This was attributed to sediments not  
641 capturing the full bedrock age signal in a very large catchment. This could very well be  
642 the case here as well, since the sampled Selenga catchment is >95000 km<sup>2</sup> in size.

643 3) The ‘spike’ in the measured detrital age PDF is the only main point of deviation between  
644 the PDFs and occurs at a large step in the hypsometric curve, which roughly aligns with  
645 the shift from the background low-lying elevations in the deeper basin to the elevated  
646 landscape of the Hangay. This shift likely signifies a regional, preferential cooling age  
647 ‘erosional zone’ that is the current focus of incision at the crossover into higher  
648 elevations of the Hangay where more sediment of the primary detrital peak is being  
649 sourced. In line with this, the mismatch between hypsometry and the age CSPDF may  
650 also signify a change in erosion rate at ~120-130 Ma, which agrees to first-order with the  
651 *West et al.* [2013] apatite fission-track AER (fig. 8).

652  
653 The large spread in our observed detrital ages suggests that erosion has been slow, of low  
654 magnitude, and operative over a prolonged period since the Mesozoic. In a simplistic 1-D case  
655 where lateral advection is ignored, an erosion rate over the time represented by the detrital  
656 population can be calculated by simply dividing the total catchment relief by the cooling age  
657 range, which in this case is quite long, >150 Ma. Long-term slow erosion and low modern relief



658 suggest that the shallow isotherms have conformed to the topography, and a simple 1-D  
 659 technique is adequate for erosion rate estimation [Whipp *et al.*, 2009]. To reduce the influence of  
 660 potential outlier ages, only cooling ages falling within 95% of the detrital population mean were  
 661 used. The detrital apatites from the Selenga catchment that source the majority of the western  
 662 Hangay and northern Mongolia show a time-integrated erosion rate ( $\dot{E}$ )  $\approx$  17 m/My, which  
 663 decreases to  $\sim$ 10 m/My if the entire detrital dataset is used. This is in agreement with the  
 664 independently derived basalt incision rates for the late Cenozoic and previous thermochronologic  
 665 and cosmogenic estimates for the region cited in section 2, all in accordance with a long-term  
 666 history of slow erosional exhumation.



667

668 **Figure 8:** Apatite AERs (left panel) from the western Hangay near Otgontenger (highest peak; figs. 3 and  
 669 4) incorporating a short transect from this study and from *West et al.* [2013] and *Landman* [2007] datasets  
 670 (see fig. 5 for transect locations). Positive AERs suggest valley-scale topographic wavelengths do not  
 671 affect low-T isotherms. Right panels show AFT and mean fission-track lengths (MTL) for *Jolivet et al.*  
 672 [2007] and *West et al.* [2013] datasets. Planation surfaces in the Gobi Altai, Valley of Lakes, and W.  
 673 Hangay (gray) are all similar in age suggesting regionally coincident exhumation and that highest  
 674 elevations are preserved remnants from an older event. *West et al.* AFT transect suggests the period

675 between ~180-130 Ma being governed by a moderate exhumation rate. Our rates and those published on  
676 the right are for the AHe transects and overestimate the true exhumation rate.  
677

678 Conversely, the detrital cooling age range and the AER can be used to estimate the paleo-relief  
679 of a catchment [*Stock and Montgomery, 1996*]. On the large scale in the slowly-eroding Hangay,  
680 isotherms would presumably now be parallel to the surface, and assuming horizontal isotherms,  
681 the exposed bedrock ages divided by the modern relief yields the change in cooling age with  
682 elevation. By the same token, the detrital age range divided by the AER provides estimates of the  
683 paleo-relief. The apatite fission-track AER of *West et al. [2013]* spans  $46.34 \pm 0.24$  Ma over  $1.23$   
684  $\pm 0.01$  km of modern elevation (using 10 m elevation errors from 90 m DEM) in the western  
685 Hangay. Using the 95% spread about the mean Selenga detrital age approximates catchment  
686 paleo-relief of  $3.39 \pm 0.1$  km, or a  $0.79 \pm 0.1$  km decrease in relief in the time represented by the  
687 sub-basin detrital dataset. However, two potential caveats exist for interpreting AERs throughout  
688 the Hangay, (1) the rivers sample the flank of a long wavelength topographic structure, which  
689 presumably means the isotherms conform to the topography to some degree, and (2) the remnant  
690 planation surfaces imply that the landscape underwent modest uplift and has been deformed  
691 since the development of the low relief surface, therefore the cooling ages could vary as a  
692 function of depth below the surface and not with elevation. We see both positive and negative  
693 AERs across the landscape, which collectively suggest either paleo-relief change or incision of a  
694 thermally stable upper crust.

695  
696 Our detrital age sample population is too small to allow a definitive assessment of landscape  
697 change, although assumptions of widespread steady-state erosion in the Hangay are invalidated.  
698 It is reasonable to suspect that the landscape has experienced variable, finite erosion since the  
699 Cretaceous that has been more focused in certain areas of the landscape. The continued existence

700 of the remnant planation surfaces across the Hangay is further evidence that an erosional steady  
701 state has yet to be reached. The recent surface uplift has potentially complicated the erosional  
702 history and provided a “regional knickpoint” at the uplifted Hangay margins for focused incision,  
703 which is supported by knickpoints in river profiles at elevations of ~2000-2500 meters [*West et*  
704 *al.*, 2013]. The eastern Hangay and Orkhon watersheds contain the majority of Cenozoic valley-  
705 filling basalts that have dammed valleys and locally disrupted the fluvial system by resetting  
706 base level in the last ca. 10-15 Ma. Our geomorphic observations, detrital data, and the findings  
707 of *West et al.* [2013] agree and support modest glaciation, recent surface uplift, modern  
708 precipitation gradients, and structural or lithologic controls as the cause of localized erosional  
709 variability in this setting. Our detrital AHe ages also suggest areas of the Hangay landscape near  
710 ~1600-1800 m elevation are the focus of erosional unroofing.

711

## 712 **5.2 Pecube-NA thermo-kinematic modeling**

713 We are interested in not only the long-term exhumation of the region but also the relief evolution  
714 through time. We performed modeling analogous to the Dabie Shan study of *Braun and Robert*  
715 [2005] to ascertain the topographic and thermal histories necessary to produce the observed AHe  
716 dataset for central Mongolia using Pecube. Modeling was carried out as an exploration of  
717 plausible scenarios rather than an attempt to rigorously invert for actual values that are free of  
718 assumptions, including inferences about the state of relief earlier in the Mesozoic or spatial  
719 variability in timing, magnitude, and phases of exhumation during that time. Our thermo-  
720 kinematic models are inherently non-unique and should be viewed as an assessment tool that aid  
721 in ruling out extremes, and to assess whether our AHe data permit any ‘young’ exhumation  
722 scenario.

723

### 724 **5.3 Inversion resolution tests**

725 As a first step, we ran a Pecube-NA sensitivity test inversion in the same model domain as our  
726 true inversions in the western Hangay to primarily assess model performance and the ability of  
727 the model to efficiently evaluate if exhumation rates and relief could be adequately constrained  
728 to first order. Values for erosional timescale ( $\tau$ ), relief amplitude ( $R$ ), and exhumation rate timing  
729 (E-timing) were set and run through a forward Pecube model to produce synthetic AHe and AFT  
730 cooling ages. These synthetic ages were then used as input in a Pecube inversion to determine if  
731 the true values could be recovered (with 6% and 10% synthetic measurement uncertainties  
732 derived from the output ages,  $2\sigma$ ; results shown in table 2). The sensitivity test recovered the true  
733 parameter values and the overall misfit was very good, however the assigned synthetic age errors  
734 were larger than the observed analytical errors on our data, and so were more permissive of good  
735 fits.

736

737 We then tested whether moderate relief change in a slow exhumation setting is adequately  
738 modeled using Pecube-NA (fig. 9). We set background exhumation rates from exhumation phase  
739 #1,  $E_1$ , from 180-90 Ma at 0.1 km/My and a second slower phase,  $E_2$ , from 90-0 Ma at 0.03  
740 km/My. The relief amplitude,  $R$ , is set to 0.5 (50% of modern relief) at the model start, and the  
741 erosional timescale,  $\tau$ , to 750 Ma. These variables are fixed and a Pecube forward model predicts  
742 model AHe and AFT cooling ages output at the same locations as observed data applying 6%  
743 AHe and 10% synthetic AFT age errors. The model ages and respective errors are then supplied  
744 back into two NA inversions, one where the relief amplitude is the only free parameter varying  
745 between 0-2, and the other with  $\tau$ ,  $R$ , and E-timing set free. This second test is to examine the

746 ability to identify the true parameter values and any tradeoff effects. The second resolution test  
747 initially allowed  $E_1$  and  $E_2$  as free parameters but during initial tests the “true” rates were quickly  
748 identified, therefore during later inversions the background exhumation rates were fixed.

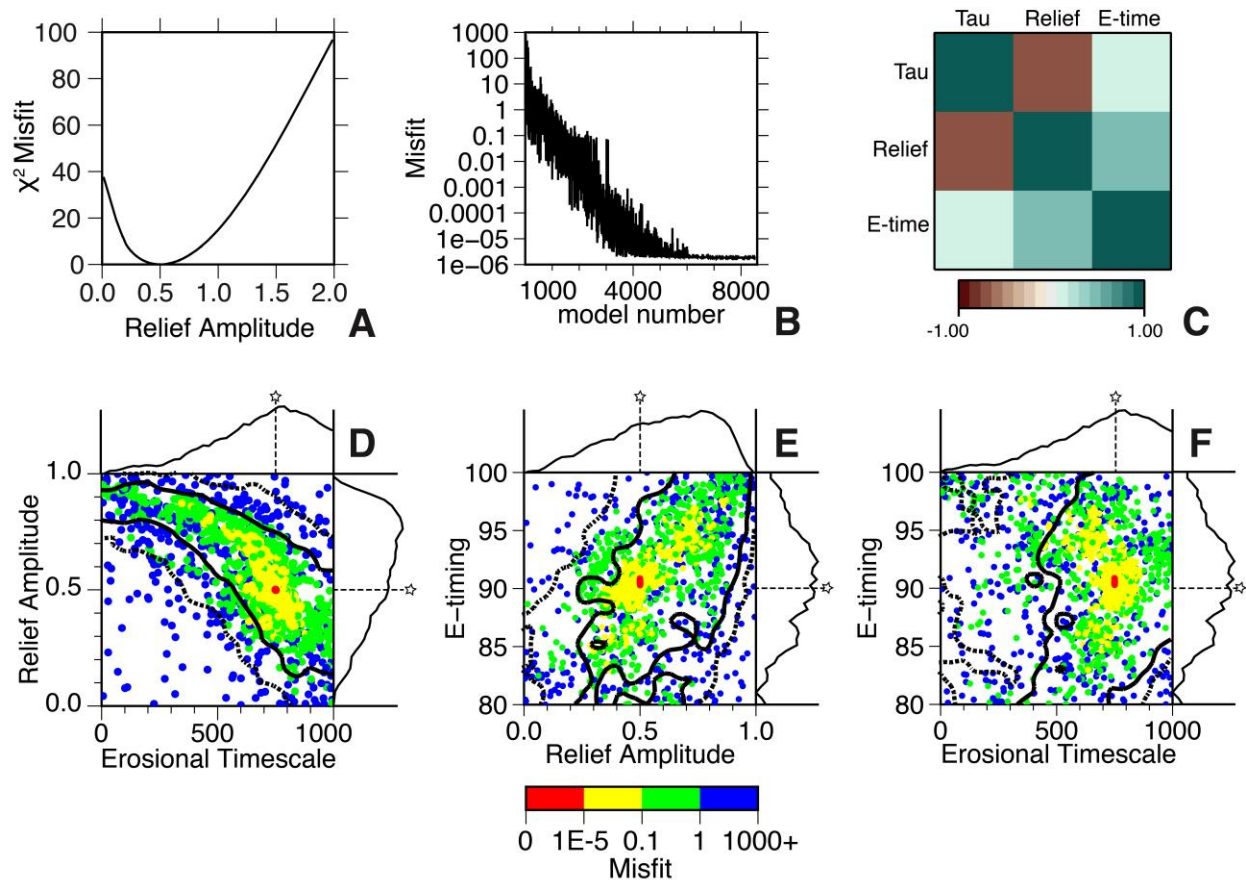
749

750 The relief amplitude-only sensitivity test inversion (fig. 9A) was set to run for >6000 total  
751 models with 96 models in an initial iteration and 96 models in each subsequent iteration with a  
752 96% resampling rate. Convergence on the true value of  $R = 0.5$  was found within a few hundred  
753 models but the algorithm was allowed to run to ~850 models before the run was stopped due to  
754 adequate convergence. This result verifies that in the case of low model complexity  
755 (dimensionality), well-known thermo-kinematic parameters and high quality  
756 thermochronometric data can accurately resolve relief change in a post-orogenic setting to within  
757 2% in a short number of iterations, in this example the best 50 models resulted in an  $R = 0.49 \pm$   
758  $0.02$  ( $1\sigma$ ).

759

760 The sensitivity test inversion for  $\tau$ ,  $R$ , and E-timing was run with an initial and subsequent pool  
761 of 112 models over 75 iterations with a 68% resampling rate for a total of 8504 models (fig. 9B-  
762 F). The lowest misfit values matched the true values very accurately, suggesting the absence of  
763 synthetic noise in the resolution test. The model appraisal shows that relief amplitude was well  
764 resolved with a mode and standard deviation of  $0.57 \pm 0.23$  for  $R$  and E-timing mean of  $90.2 \pm$   
765  $5.5$  Ma. The erosional timescale showed considerable scatter but was within one standard  
766 deviation of the true value. Trade-offs between parameter combinations can be noted in figure  
767 9C. Under fixed exhumation rates, relief amplitude decreases non-linearly as the relief-change

768 timescale increases, while the timing of exhumation rate change is positively correlated with  
 769 both relief amplitude and relief-change timescale.



770

771 **Figure 9:** Pecube-NA sensitivity test of variables controlling relief to assess the ability to resolve relief  
 772 change in this type of slow exhumation setting. For tests, a two-phase exhumation scenario was used with  
 773 fixed rates of 100 m/My and 30 m/My. (A) Sensitivity test for *relief amplitude-only* showing least-  
 774 squares misfit and relief amplitude between 0 (no relief) to 2 (two times modern relief) with a defined  
 775 misfit minima at the true value of 0.5X the modern relief in the Hangay. (B) Misfit evolution over the  
 776 sensitivity test inversion where  $\tau$ , R, and E-timing are allowed free, exhibiting optimal convergence after  
 777  $>6000$  models. (C) Correlation matrix for the free inversion parameters using NA-plot [Sambridge,  
 778 1999b]. Values approaching (-1)+1 show greater (anti)-correlation while values near 0 show no  
 779 relationship or dependence. Erosional timescale and relief amplitude are highly anti-correlated, while both  
 780 the exhumation rate change timing and relief amplitude have a slight positive correlation with erosional  
 781 timescale. These trends can also be seen in the PPDFs in panels D to F. (D-F) Scatter plots showing misfit  
 782 between  $\tau$ , R and E-timing, the 2-D PPDF  $1\sigma$  (solid) and  $2\sigma$  (dashed) contours shown as overlays and the  
 783 corresponding 1-D marginal PPDF curves for each parameter on the corresponding axes. In each case the  
 784 star marks both the ‘true parameter value’ and in this case, the respective lowest misfit of the 1-D PPDF,  
 785 which in this synthetic example is also the mean or modal value.

786

## 787 5.4 Pecube-NA model inversion results

788 Following the sensitivity tests, we then applied Pecube-NA modeling to learn about the  
789 landscape evolution in Mongolia. The AHe thermochronologic data suggest low background  
790 exhumation rates have been sustained over the past ~100 m.y., so here we test the resolving  
791 power of the Pecube-NA model to estimate timing and magnitude of long-term exhumation rates  
792 and paleo-relief histories using a modest data subset in the western Hangay. We used  
793 representative values for model (crustal) thickness, basal temperature, etc. for central Mongolia  
794 (table 1) and our data input consists of replicate single grain AHe cooling ages and those  
795 reported in *West et al.*, [2013]. Figures 10 and 11 and table 2 show inversion results. We ran  
796 ~10,000 models for each inversion with a resampling rate between ~60-70% to obtain adequate  
797 convergence and sampling of the model space.

798

799 We report results for two inversions that simulate the last 150 Ma in the western Hangay (see  
800 figs. 12 and 13 for location). One inversion (run 1-TSW) held the major exhumation phase  
801 timing fixed from 150-130 Ma, which was derived from the modeled AFT thermal history of  
802 *West et al.* [2013]. The optimal relief history and basal temperature of the model (geothermal  
803 gradient) were investigated in this run. The inversions allowed relief to evolve in one of three  
804 ways, either (1) relief stays fixed through time (same as modern topographic relief), (2) start as a  
805 plateau at low elevations with simulated ‘incision’ to grow the modern topography, or (3)  
806 topography is at higher elevations (than modern peaks) at the model start and is then incised to  
807 form the modern topography. A second inversion attempt allowed the end of the exhumation  
808 phase to be a free parameter (run 1-C). The second inversion with the unrestricted exhumation  
809 phase was mainly for comparative purposes, as delayed or prolonged exhumation may have been

810 possible in different parts of Mongolia during the end of the Mongol-Okhotsk orogeny in the  
 811 Jurassic through the Cretaceous.

812

**Table 1: Model parameters used in Pecube-NA inversions**

Fixed Parameter	Value	Units	Reference
Model initiation	150	Myr	
Basal temperature, $T_b$	850	°C	<i>Ionov et al., 1998; Ancuta, 2017</i>
Volumetric heat production, $H$	0.7	$\mu\text{W m}^{-3}$	<i>Lysak and Dorofeeva, 2003</i>
Radiogenic heat production, $A$	8	°C Myr <sup>-1</sup>	
Thermal diffusivity, $\kappa$	25	km <sup>2</sup> Myr <sup>-1</sup>	
Specific heat capacity, $C_p$	800	J kg <sup>-1</sup> K <sup>-1</sup>	
Surface Temperature, $T_s$	0	°C	
Atmospheric lapse rate	0	°C km <sup>-1</sup>	
Crust/Mantle density, $\rho_c/\rho_m$	2800/3300	kg m <sup>-3</sup>	
Model Thickness, $Z_c$	49	km	<i>Stachnik et al., 2014</i>
Effective elastic thickness, $T_e$	6.1	km	<i>Bayasgalan et al., 2005</i>
Model domain	80 x 60	km	
1 km grid resolution	0.00833	degrees	
Vertical node spacing	1	km	

813

814 **Table 1:** Fixed model parameters used in Pecube inversions to calculate the isostatic and thermal  
 815 response to varying relief.

816

817

818

819

820

821

822



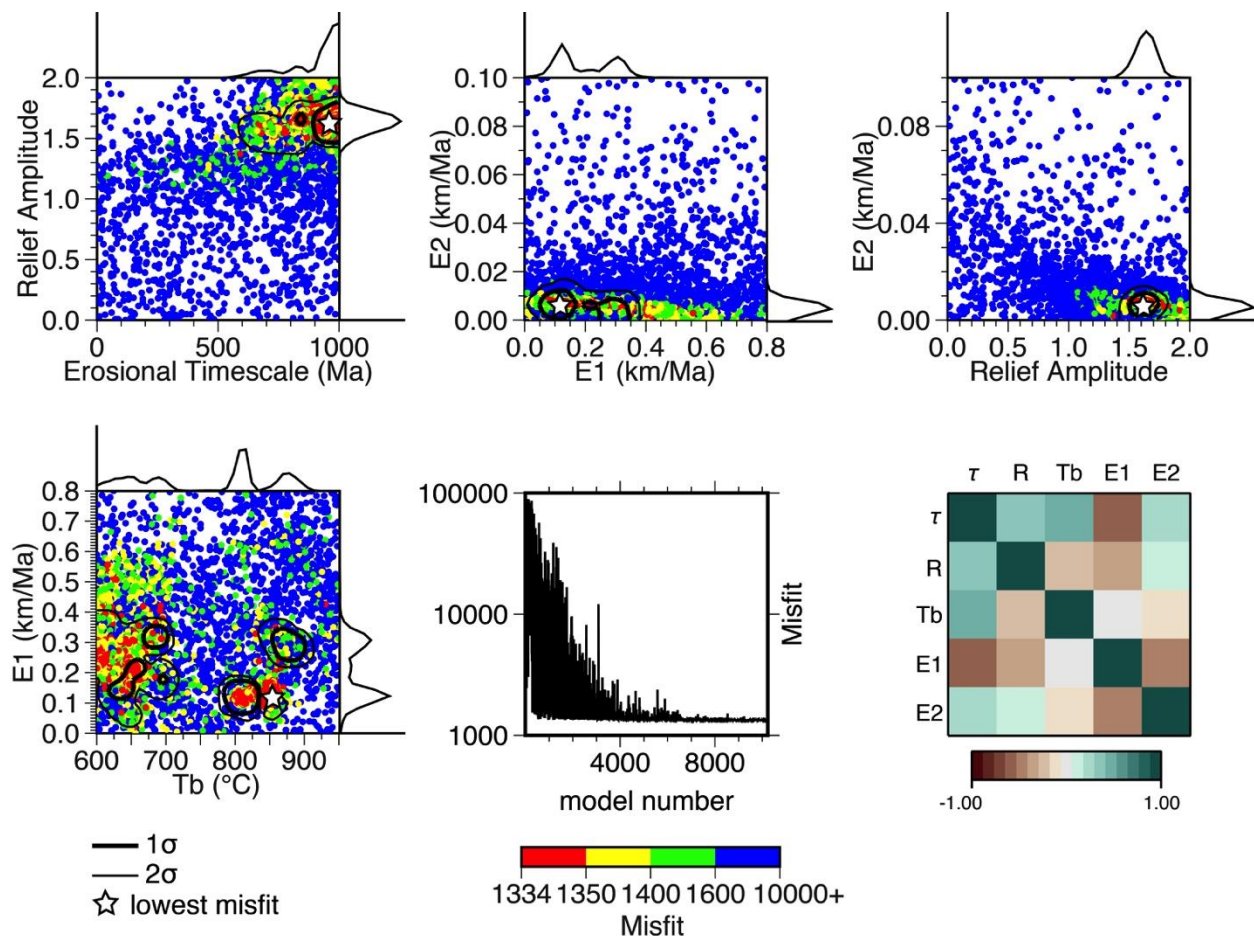
**Table 2: Pecube-NA inversion results**

<b>SENSITIVITY TEST</b>				
<b>Inversion Parameter</b>	<b>True value</b>	<b>Inversion Results</b>	<b>Mean <math>\pm</math> SD</b>	
Erosional timescale (Myr), $\tau$	750	750.1 (0:1000)	608 $\pm$ 260	
Relief amplitude, $R$	0.5	0.50 (0:1)	0.57 $\pm$ 0.23	
Exhumation change timing (Myr), E-timing	90	90.4 (100:80)	90.2 $\pm$ 5.5	
Exhumation rate 1 (km Myr <sup>-1</sup> ), $E_1$	0.1	-	-	
Exhumation rate 2 (km Myr <sup>-1</sup> ), $E_2$	0.03	-	-	
Number of models	8512			
Lowest misfit, $\mu$	1.8E-06			
Misfit type	$\chi^2$			
Free parameters	3			
Models/Iterations	112/75			
Resample rate	68%			
<b>FULL INVERSIONS</b>	<b>INVERSION 1</b>		<b>INVERSION 2</b>	
<b>Inversion Parameter</b>	<b>Run 1-TSW</b>	<b>Mean <math>\pm</math> SD</b>	<b>Run 1-C</b>	<b>Mean <math>\pm</math> SD</b>
$\tau$	<b>930</b> (0:1000)	890.6 $\pm$ 110	<b>482</b> (0:1000)	491.7 $\pm$ 43
$R$	<b>1.58</b> (0:2)	1.62 $\pm$ 0.08	<b>1.24</b> (0:2)	1.20 $\pm$ 0.07
E-timing	130	-	<b>116.5</b> (130:100)	116.0 $\pm$ 1.1
$E_1$	<b>0.13</b> (0:0.8)	0.21 $\pm$ 0.09	<b>0.22</b> (0:0.5)	0.23 $\pm$ 0.03
$E_2$	<b>0.0071</b> (0:0.1)	0.0064 $\pm$ 0.0029	<b>0.0056</b> (0:0.1)	0.0078 $\pm$ 0.0046
$T_b$ (basal temp, °C)	<b>860.5</b> (600:950)	760.7 $\pm$ 92.8	850	
Time Step	1		1	
Run time (Ma)	150		150	
Number of models	10224		9504	
Lowest misfit, $\mu$	1334.2		1325.5	
Number of Data	28		28	
Misfit type	$\chi^2$		$\chi^2$	
Free parameters	5		5	
Models/Iterations	144/70		144/65	
Resample Rate	63%		70%	

**Table 2:** Pecube-NA inversion results for sensitivity test and full inversions. Values separated by a colon are the prior search ranges during the NA sampling stage while those in bold are the best-fit parameter values (lowest misfit). Mean and standard deviation represent the resampling results from the NA

829 appraisal of the model ensemble.  $R$  = relief amplitude;  $\tau$  = erosional timescale; E-timing is the time of  
 830 exhumation rate change;  $E_1$  and  $E_2$  = exhumation rate 1 and exhumation rate 2. See text for details.  
 831

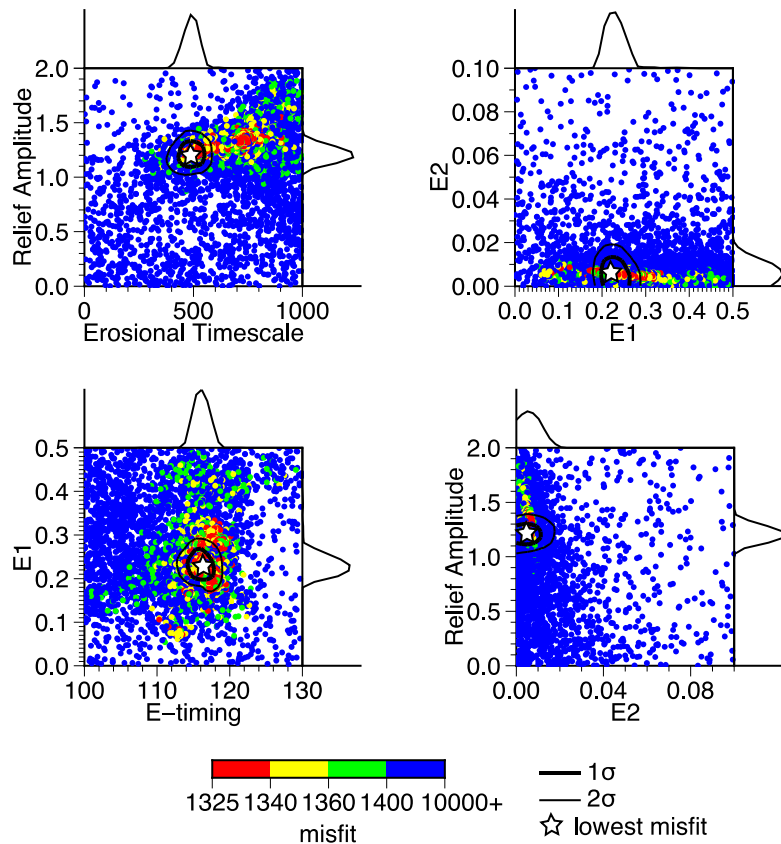
832 Model inversion 1-TSW (fig. 10) shows paleo-relief  $\sim 50\%$  greater than the modern relief ( $1.62 \pm$   
 833  $0.08$ ) is required to explain the AHe ages. The  $\tau$  (erosional timescale) parameter is a primary  
 834 control on the evolution of relief, as the relief amplitude and erosional timescale show a positive  
 835 correlation. The large positive value for  $\tau$  suggests exponentially rapid relief evolution following  
 836 the main exhumation phase with the majority of paleo-relief ( $\sim 90\%$ ) reduced by ca. 100-85 Ma  
 837 (see fig. 12).



838  
 839 **Figure 10:** Pecube-NA inversion results for Run 1-TSW. Scatter plots are 2-D projections of the 5  
 840 dimensional parameter space on planes defined by combinations of two parameters. 1-D posterior curves  
 841 show probability density within the parameter search range. See supplementary material for additional  
 842 plots of other variables. Each dot represents a forward model from the inversion and is colored by the  $\chi^2$   
 843 misfit value. Stars denote the lowest misfit model while heavy/thin black lines are  $1\sigma$  ( $67\%$  confidence)

844 and  $2\sigma$  (95% confidence) errors, respectively. Bottom middle panel shows misfit evolution and  
845 convergence during the inversion and the bottom right shows the correlation matrix between difference  
846 parameters between -1 to +1 signifying strong (negative) anti-correlation or positive correlation, with  
847 values near zero having no relationship. Pecube physical modeling domain shown in fig. 13 inset box, see  
848 text for discussion.  
849

850 Inversion 1-C results are in good agreement with inversion 1-TSW, where the only difference is  
851 in the delayed timing in exhumation rate change at  $\sim 116$  Ma (lowest misfit), which appropriately  
852 constrains the predicted relief reduction to be lower and approaches a relief amplitude of 1.0,  
853 suggesting very little to no relief change by the end of the Cretaceous (fig. 11). A two-stage  
854 exhumation scenario was applied for simplicity and because more complicated exhumation  
855 histories are unnecessary to explain the data. If exhumation is shorter in duration, i.e. 150 to 130  
856 Ma versus 150 to  $\sim 115$  Ma, the required paleo-relief is also greater. Both inversions suggest  
857 background exhumation was never extremely rapid during this time, on the order of  $\sim 100$ -200  
858 m/My during the primary phase and very low since the Early Cretaceous at  $\leq 10$  m/My (table 2).  
859 The  $E_1$ - $E_2$  scatterplot (fig. 11; table 2) shows that the secondary phase of exhumation is required  
860 to be very low at  $\sim 6 \pm 3$  m/My, regardless of what the  $E_1$  exhumation rate is. The erosion rates  
861 for the Hangay, which account for background exhumation, isostasy, and relief evolution,  
862 suggest rates in the higher elevations (fig. 12A) of up to 16 m/My since the Early Cretaceous.  
863 The geothermal gradient, which is controlled by the basal temperature ( $T_b$ ) shows two distinct  
864 regions of either a cooler or hotter temperature, where neither has a clear relationship with the  
865 primary exhumation phase ( $E_1$ ), however larger values of  $R$  require a lower ( $E_2$ ) exhumation rate.  
866 The best-fit model has a basal temperature of  $860^\circ\text{C}$ , which is in agreement with local  
867 geochemical data [e.g. *Ionov et al.*, 1998; *Ancuta*, 2017] and produces a geothermal gradient in  
868 agreement with paleo- and modern estimates of 15 and  $21^\circ\text{C}/\text{km}$ , respectively [*Ionov et al.*,  
869 1998; *Kopylova et al.*, 1995; *Lysak and Dorofeeva*, 2003; *West et al.*, 2013].



871

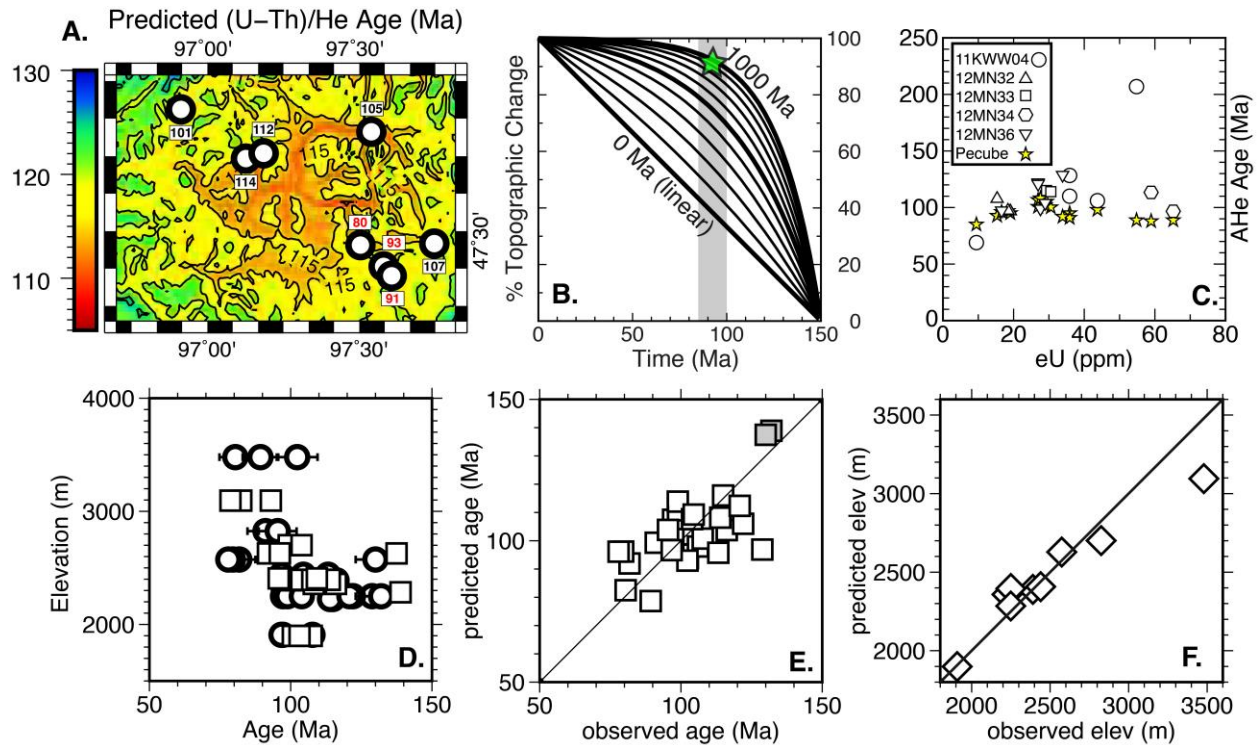
872 **Figure 11:** Pecube-NA Run 1-C inversion results for 9504 models. The same figure scheme as figure 9.  
 873 The difference between Run 1-TSW is that the exhumation rate change timing is allowed free in this  
 874 inversion.

875

876 The misfit values reported for the full inversions are higher than the sensitivity inversion because  
 877 the sensitivity test allowed much greater variance in the synthetic age uncertainties. The full  
 878 inversions used the analytical error, which is typically  $\leq 2$  Ma. The observed and predicted ages  
 879 agree very well, generally within 2%, except for a few cases where the reported AHe age is  
 880 slightly older ( $\sim 10\%$ ) than the predicted age, which drove the misfit up (fig. 12; suppl. table S4).  
 881 The reported multi-grain aliquot AHe data from *West et al.* [2013] were over-predicted and were  
 882 the main contributors to the higher overall misfit values, stressing the importance of single-grain  
 883 (U-Th)/He data in old, slowly-cooled regions.

884

885 We ran Pecube forward models using the best-fit parameters of inversion 1-TSW to predict  
886 model regional AHe cooling ages (fig. 12), since our inversions are focused on a small area of  
887 the western Hangay and the flexural response to exhumation will be variable depending on the  
888 size of the area modeled. Figure 12C-F shows observed versus predicted cooling ages using the  
889 best-fit parameters from inversion 1-TSW for the western Hangay and the age-eU relationship  
890 using the RDAAM for age prediction. The major discrepancy in age agreement (higher  
891 associated misfit) lies between the *West et al.* [2013] multi-grain aliquot AHe ages and those  
892 modeled at high elevations (fig. 12A and 12D). This is likely due to the cooling age ‘averaging’  
893 bias from using multiple grain aliquots, and in combination with the known scatter in slowly  
894 cooled samples, produces ages that do not adequately represent the ‘true’ single grain cooling  
895 ages. In this case, it seems that the *West et al.* [2013] AHe ages are younger in comparison to  
896 nearby samples from this study. Potential outlier ages from our dataset that are anomalously old  
897 and not readily explained by radiation damage, grain size, etc., also cannot be fit adequately (fig.  
898 12C and fig. 14E). The elevation for the highest samples is also under-predicted (fig. 12F),  
899 which may be convolved with the errors associated with the age prediction itself, or indicates  
900 that the predicted relief evolution is too simplistic and does not fully capture the nuanced  
901 topography (see regional model in fig. 14).



902

903

904 **Figure 12:** (A) Contoured age map (5 Ma interval) of Pecube-NA Run 1-TSW in the western Hangay  
 905 (see fig. 13 for location, inset box). Locations of samples are circles with mean ages shown, ages in red  
 906 are multi-grain aliquots from *West et al.* [2013]. Note that single grain ages were used in the inversion.  
 907 Single grains shown in panel D. (B) Plot showing how topography changes in the model according to  
 908 equation 6. Our model inversion 1-TSW exhibits highly positive best-fit values for  $\tau$ , suggesting relief  
 909 decayed rapidly and was  $\geq 90\%$  of the modern relief by ca. 100-85 Ma. (C) A plot of single-grain AHe  
 910 ages with respect to eU for a few samples in the modeling domain. The Pecube model predictions (stars)  
 911 are fairly consistent with observed age-eU patterns. (D) Observed and predicted cooling ages and  
 912 corresponding elevations are in good agreement except mainly at the highest elevations which are derived  
 913 from Pecube forward models using our best-fit or maximum likelihood values from the model inversion.  
 914 Black circles are observed single-grain age replicates with errors, while squares are predicted cooling  
 915 ages. (E) 1-to-1 line for predicted vs. observed cooling ages; gray squares are AFT samples. (F) observed  
 916 versus predicted elevations using best-fit 1-TSW inversion relief scenario in Pecube forward model.

917

918 The optimum inversion 1-TSW model parameters for the western Hangay were held fixed and

919 extrapolated to the entire Hangay and forward modeled (fig. 13). Four different model scenarios

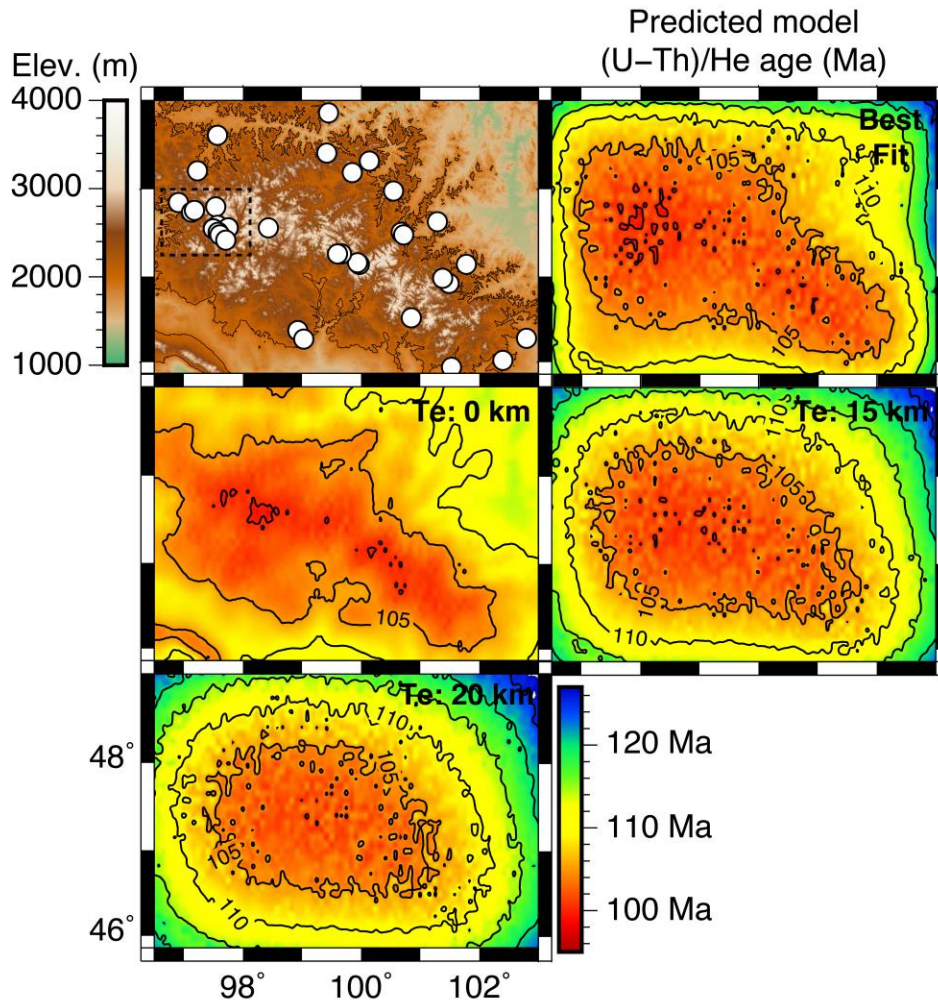
920 explored changes in effective elastic thickness. This was done to test the flexural response to

921 erosional unloading, which is magnified or isostatically-enhanced when the elastic thickness is

922 low (in local isostatic equilibrium), compared to a high elastic thickness of 20 km or more

923 (strong lithosphere). These results highlight the complexity between relief evolution and isostasy  
924 and deconvolving the two in a slowly-eroding setting where isostasy is a primary contributor to  
925 rock uplift over long timescales. Regional variations in lithospheric thickness and mechanical  
926 properties, as well as varying depths of seismicity and changes in regional faulting character,  
927 cause effective elastic thickness variability in Mongolia [Bayasgalan *et al.*, 2005]. The Pecube-  
928 predicted age surface maps were resampled at the 10 km length scale to smooth age gradients  
929 (fig. 13). Contouring the predicted age surfaces allowed comparisons of regional cooling age  
930 spatial patterns. The effective elastic thickness from Bayasgalan *et al.* [2005] is shown in the  
931 upper right panel ( $T_e$  of 6.1 km), while the other panels show results using elastic thicknesses of  
932 0 (local isostasy), 15, and 20 km. Local isostasy ( $T_e = 0$ ) produces uniform predicted ages across  
933 the Hangay, closely following the topography but with less age variation in the broad sense (fig.  
934 13). Increasing  $T_e$  (panels 15 and 20 km) yield concentric ‘bulls-eye’ patterns of increasing  
935 cooling ages away from the range center with less topographic correlation. However, this pattern  
936 is partially due to an edge effect modeling artifact because of the ‘zero exhumation’ model  
937 domain boundary but would be theoretically expected if  $T_e$  increases away from the Hangay  
938 high elevations. The overall misfits for each model are fairly similar and fit the data within  
939 analytical error (reduced chi-squared misfit 0.8-0.9), demonstrating that varying  $T_e$  has little  
940 effect on the match between observed and predicted ages for low exhumation rates. However, at  
941 the orogeny-scale an elastic thickness of 20 km yields a marginally better misfit compared to the  
942 other models, which agrees with the findings of Bayasgalan *et al.* [2005] that the elastic strength  
943 of the lithosphere increases away from the central Hangay.





944

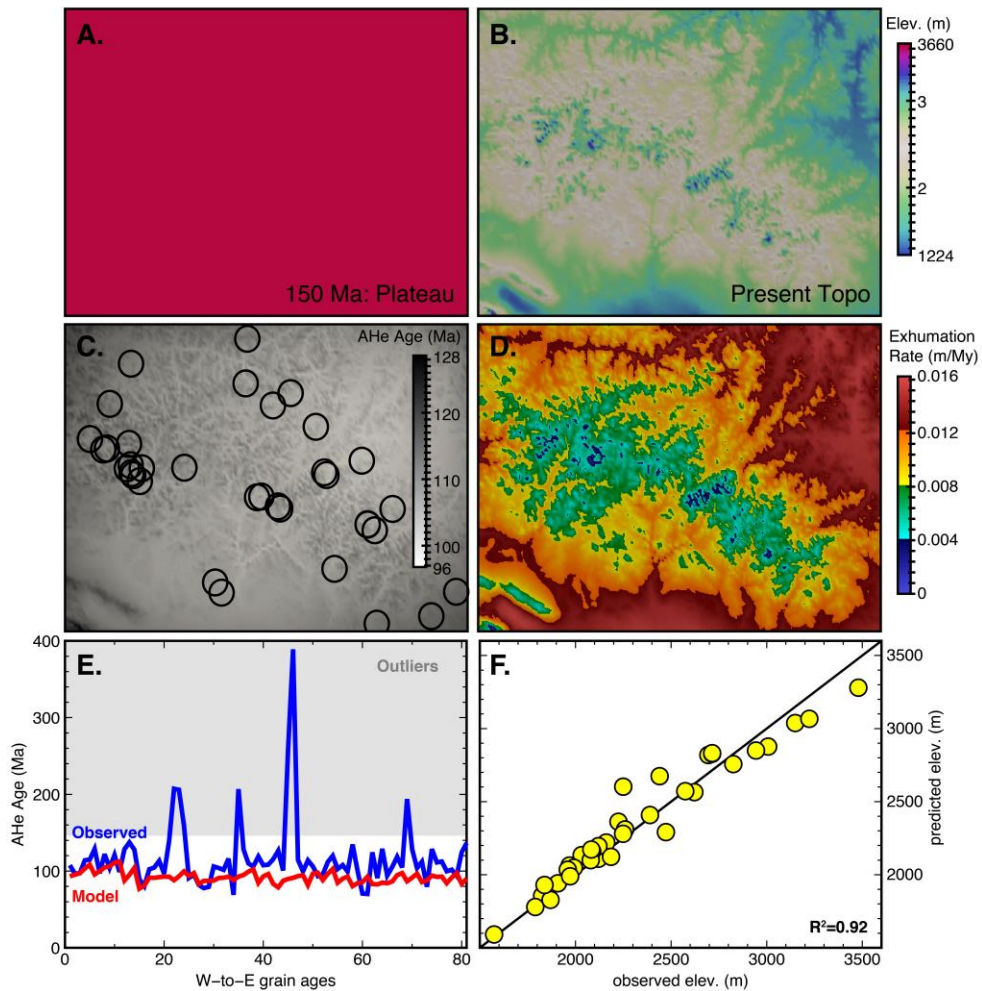
945 **Figure 13:** Pecube forward model age predictions using inversion run 1-TSW best-fit parameter values  
 946 with the main exhumation stage from 150-130 Ma after *West et al.* [2013] model thermal history. Inset  
 947 box shows location of western Hangay bounds used in Pecube-NA inversion. Regional forward models  
 948 are resampled at 10 km to smooth ages and are shown with a 5 Ma contour interval. (Top left) Elevations  
 949 from 90m SRTM DEM (2000 m elev. contoured) with white dots showing sample locations used in  
 950 Pecube modeling of the entire Hangay, (top right) the ages predicted by the best-fit model results of  
 951 inversion 1-TSW shown in table 1 ( $T_e = 6.1$  km). Other panels show the effects of varying the effective  
 952 elastic thickness ( $T_e$ ) while holding all other best-fit variables constant.  
 953

954 To investigate relief evolution in a more regional sense and to reproduce the relict planation  
 955 surfaces, we ran a Pecube forward model for central Mongolia using our full AHe dataset that  
 956 begins at 150 Ma with a flat plateau at the highest modern elevation, similar to *Valla et al.*  
 957 [2010] (fig. 14A and 14B, same regional model domain as shown in fig. 13). This simulates a  
 958 regional relief increase through preferential valley incision, where highest peaks stay at a fixed



959 point but valley bottoms are lowered. Forward modeling was necessary because a full inversion  
960 over such a large area would be computationally infeasible. For simplicity, late Cenozoic surface  
961 uplift (elevation change) is ignored because it amounts to only on the order of a few hundred  
962 meters, accompanied by minor erosion, and occurs very late in the overall history, so it is of little  
963 consequence for AHe age prediction. We used a DEM resampled to 4 km resolution for faster  
964 computation over this large area, an elastic thickness of 20 km, and the  $E_1/E_2$  exhumation phases  
965 and best-fit background exhumation rates from inversion 1-TSW (fig. 14). All other forward  
966 model parameters were the same as the inversions. The forward model MSWD misfit is very  
967 high ( $\gg 1$ ) for models involving an exponentially rapid late change in topography (i.e. young  
968 relief creation) or a linear change through time, which is expected since our AHe data are old and  
969 require cooling through closure isotherms in the Mesozoic. We used a value of 930 My for the  
970 erosional timescale ( $\tau$ ), which indicates rapid relief change early in the model (fig. 12B) and is  
971 the best-fit value from inversion 1-TSW. The major assumption here is that differential  
972 exhumation across the region is not high, however we know this is likely the case given our  
973 detrital modeling results, older bedrock AHe ages outside the Hangay, and the effects of isostasy  
974 in the Hangay compared to the outlying area. This model is simplistic and meant to reproduce  
975 observed regional cooling age spatial patterns to first order and the predicted AHe ages are in  
976 agreement with observed data (MSWD=0.92), especially in the Hangay high elevations (fig. 14C  
977 and 14E). However, older observed ages outside of the Hangay to the northeast would be  
978 predicted too young under these exhumation conditions, suggesting more complexity is required  
979 to fully capture subtleties, including differential uplift/regional tilting or spatially varying  
980 exhumation. The model is able to reproduce older planation surface remnants that are not eroded  
981 while the rest of the topography shows higher exhumation rates into the lower elevations and in

982 the modern incised channels (fig. 14D), furthermore, the observed and predicted Hangay ages  
 983 (14E) and elevations are in excellent agreement (14F).



984  
 985 **Figure 14:** Pecube forward model results for a planation surface and carving of topographic relief (A)  
 986 The model starting condition for topography is a high plateau at the highest modern elevation (slightly  
 987 lower than actual due to grid resampling). See elevation scale in panel B. (B) The end of the model run  
 988 showing the modern topography. This relief was created using an erosional timescale of 930 My, which  
 989 created the modern topography (within 90%) by 100-85 Ma. Note: although difficult to see, there are  
 990 remnant surfaces (red) at highest elevations in panel B. (C) The predicted AHe age map across the region.  
 991 Ages are best predicted in the Hangay but suggest younger ages outside of the Hangay, which is not in  
 992 total agreement with real AHe data. Circles are the locations of real data used in the model (D) The  
 993 predicted exhumation rates over the single time step with two phases of exhumation using the best-fit  
 994 values from inversion 1-TSW. The rates are spatially variable and show no erosion at highest peaks and  
 995 more focused/higher exhumation in the incised topography. Exhumation rates are on par with previously  
 996 mentioned long-term estimates and inversion results between 4-16 m/My. (E) The observed and predicted  
 997 single-grain AHe ages going from west to east in panel C showing a good match (also refer to fig. 5 for  
 998 AHe age reference). The MSWD model misfit is 0.92 between observed/predicted and shaded gray  
 999 denotes single-grain age outliers. (F) The observed and predicted elevations for a ‘planation surface’

1000 exhumation model displaying excellent correlation ( $R^2=0.92$ ) and suggesting the exhumation/relief  
1001 evolution model is viable at orogeny-scale. Line is 1-to-1 for reference.  
1002

## 1003 **6. Discussion**

1004 Some first-order conclusions about the regional relief history of the Hangay can be made from  
1005 the thermochronology and modeling results. Apatite (U-Th)/He cooling ages and regional  
1006 patterns from this study document Mesozoic cooling based on spatial relationships across central  
1007 Mongolia. Modest relief lowering in the western Hangay in the latest Jurassic through  
1008 Cretaceous could expose younger ages at high peaks while valley bottoms are older, producing  
1009 an orogen-scale, inverted age-elevation relationship but maintained valley-scale positive AERs.  
1010 The steep trend of positive AERs also suggests a low elastic-plate thickness in the central  
1011 Hangay (<20 km), which has been previously advocated [*Bayasgalan et al.*, 2005]. These AER  
1012 trends have been documented in other old, post-orogenic mountains in central Asia with similar  
1013 exhumation histories, such as the Dabie Shan [*Reiners et al.*, 2003]. This age relationship is  
1014 observed in the Hangay as well, where cooling ages are generally uniform in the mountain core,  
1015 while away from the higher topography ages are slightly older, which points to modest, localized  
1016 relief change within the highest peaks, spatially variable regional exhumation, or the combined  
1017 effects of both to produce the observed cooling age patterns. A regional model for the Hangay is  
1018 that there was regional ‘peneplanation’ in the Jurassic and then relief was created rapidly in the  
1019 Cretaceous, which is consistent with the geology and tectonic models for the main cooling and  
1020 exhumation phase for central Mongolia [e.g. *Jolivet et al.*, 2007; *West et al.*, 2013]. In either  
1021 scenario, relief evolution is completed by the end of the Cretaceous and the landscape remains in  
1022 disequilibrium throughout the Cenozoic.

1023

1024 The regional bedrock cooling age trends and the detrital AHe data point to erosion following the  
1025 last major tectonic event in the Late Jurassic-Early Cretaceous. Cooling-age patterns are  
1026 explained by preferential exposure of younger rocks at higher elevations through modest summit  
1027 relief lowering or variable exhumation of the Hangay Mountains and central Mongolia that  
1028 mainly occurred during the initial post-orogenic phase in the Cretaceous. “Total exhumation”  
1029 rates that combine relief change and isostasy with the background rates are on the order of 4-16  
1030 m/My. One could instead argue that relief lowering, recent surface uplift accompanied by some  
1031 amount of erosion could produce similar age patterns however there is no evidence to support a  
1032 Cenozoic history involving accelerated, high-magnitude (>1-2 km) erosion of the Hangay.  
1033 Moderately higher erosion rates from basalt age data are only found in isolated cirques and  
1034 glacial valleys (river headwaters regions), or valleys that have experienced local base-level  
1035 changes due to Cenozoic basalt emplacement.

1036

1037 The suturing of Mongolia and collision with the Siberian craton created high mountain peaks in  
1038 central Mongolia in the early Mesozoic, which eroded rapidly through the Cretaceous. The peaks  
1039 were heavily eroded and subsequent uplift drove the creation of regional relief during the  
1040 Cretaceous (setting our AHe ages) followed by minimal exhumation since that time. This  
1041 allowed the landscape to remain as an erosional remnant throughout the Cenozoic. In either case,  
1042 an important conclusion is that relief was rapidly changed to within 10% of the modern relief by  
1043 ca. 100-85 Ma. Erosional proxies in the form of detrital cooling ages agree to first-order with  
1044 thermo-kinematic models and indicate extended, low erosion since the end Mesozoic and that  
1045 Jurassic-Early Cretaceous paleo-relief may have been modestly greater than the present in the  
1046 western Hangay. Holding the current landscape geometry fixed through time, the current

1047 approximated mountain relief of the Hangay is approximately 2500 m, which would be  
1048 approaching 4000 m in the Mesozoic using the modeled paleo-relief relative to current  
1049 elevations. Relief 50-60% greater than the modern value would produce ancient elevations in the  
1050 Hangay >5000 m at the highest peaks, roughly on par with the modern Tian Shan to the  
1051 southwest.

1052

1053 Exhumation rates estimated from Pecube inversions suggest a period of moderate exhumation in  
1054 the Early Cretaceous followed by low rates of ~4-16 m/My since that time. This history agrees  
1055 with shorter-term cosmogenic estimates of erosion and implies that the Hangay have been  
1056 subject to a long regime of very slow erosion, similar to other old orogenic landscapes, such as  
1057 the Appalachians in the eastern USA [e.g. *McKeon et al.*, 2014]. The high-elevation regions of  
1058 the Hangay have experienced topographic rejuvenation because of recent enhanced erosion from  
1059 alpine glaciation that is minimal in magnitude and regional extent (supplement fig. S2).

1060

1061 In summary, thermochronological evidence provides support for either minor high-elevation  
1062 peak relief loss or formation of the central Mongolian landscape in the Mesozoic through  
1063 variable exhumation and relief change subsequent to Late Jurassic through Early Cretaceous  
1064 tectonism associated with terminal Mongol-Okhotsk suturing. During the Cretaceous there was a  
1065 phase of relief evolution completed by ca. 100-85 Ma followed by minor erosion since the  
1066 Oligocene due to regional “doming,” glacial cirque cutting, and fluvial incision (i.e. valley  
1067 cutting leaving non-dissected plateau remnants). There is no evidence for Cenozoic  
1068 compressional deformation in the Hangay and limited normal faulting, which suggests that the  
1069 modern landscape was formed in two main stages, with the second stage being entirely

1070 epeirogenic. All of the other regional Asian mountains are dominated by horizontal tectonic  
1071 forces, (e.g. transpressional: Altai, Gobi Altai, eastern Tian Shan; transtensional: Transbaikalia,  
1072 Longshan, etc.; [Cunningham, 2013; Cunningham, 2017]), while the Hangay are not. The  
1073 Hangay Mountains may be tectonically unique due to the Archean basement that is exposed and  
1074 underlies much of central Mongolia, which may be important in terms of long-term stability and  
1075 preservation of the landscape. Remnant landscapes may persist over hundred million year  
1076 timescales if the landscape is built upon old, rheologically strong lithosphere that may respond to  
1077 vertical forces but resist or focus horizontal tectonic stresses creating deforming belts around  
1078 their margins.

1079

## 1080 **7. Conclusions**

1081 The termination of the Mongol-Okhotsk orogeny in the Cretaceous and synchronous rapid relief  
1082 change produced the observed pattern of progressively older cooling ages away from the highest  
1083 topography of the Hangay Mountains. Bedrock apatite (U-Th)/He age spatial patterns in the  
1084 Hangay Mountains are reinforced by detrital (U-Th)/He ages and indicate <1-2 km of  
1085 exhumation since the Cretaceous, while detrital age distributions and geomorphic relationships  
1086 suggest that current elevations between ~1600-1800 m at the Hangay margins are the current  
1087 focus of incision across the landscape. A regional Pecube forward model suggests the landscape  
1088 was heavily eroded through the Jurassic, followed by subsequent uplift and exhumation that  
1089 drove creation of topography and was completed by the end of the Cretaceous. This is in  
1090 agreement with other published data that suggest some amount of regional relief planation in the  
1091 Mesozoic followed by topographic rejuvenation. Pecube thermo-kinematic inversions and  
1092 detrital age modeling suggests western Hangay paleo-topographic relief was between ~10-70%

1093 greater than the modern relief in high elevations and that total exhumation rates have been up to  
1094 16-17 m/My since the late Mesozoic. The magnitude of relief loss in Pecube model inversions is  
1095 highly correlated with the timing of the shift to very low exhumation rates, with more extended  
1096 high-rate periods (i.e. delayed exhumation rate change) requiring minimal relief loss. We prefer  
1097 conservative model predictions towards the middle to lower end of this range due to complexity  
1098 arising from the combined effects of isostasy and relief change. Relief has presumably been  
1099 stable throughout the Cenozoic due to high aridity, with a modest amount of surface uplift  
1100 probably occurring in the Oligocene-Miocene. The Hangay Mountain landscape is an old feature  
1101 that has recently undergone surface uplift of a few hundred meters, which locally imprinted a  
1102 younger, more dramatic landscape through glacial cirque cutting in the highest topography. This  
1103 mountain belt is an excellent example of a relict erosional landscape and demonstrates that  
1104 mature topography can endure for prolonged periods when there is little forcing from tectonics,  
1105 climate, or surface processes.

1106

### 1107 **Acknowledgements**

1108 The authors thank M. Fox and D. Cunningham for thorough reviews and suggestions to improve  
1109 the manuscript. We thank M. Jolivet and two anonymous reviewers for comments on an earlier  
1110 version of this manuscript. We also thank D. Whipp and F. Herman for discussions and for  
1111 supplying various bits of code and J. Braun and M. Sambridge for conversations about Pecube  
1112 and the Neighborhood Algorithm. We would also like to thank A. Pacheco of Lehigh University  
1113 HPC for support with the Lehigh Corona computing cluster. Final inversions were run through  
1114 XSEDE and the SDSC Gordon/Comet clusters and the UT-Austin TACC Stampede cluster. This

1115 study was supported by a grant from the National Science Foundation CD program grant EAR-  
1116 1009702. The data used are listed in the references, figures, tables, and supplements provided.

1117  
1118  
1119  
1120  
1121  
1122

## 1123 **References**

1124

1125 Ancuta, L. D. (2017), *Toward an Improved Understanding of Intraplate Uplift and Volcanism: Geochronology and Geochemistry of Intraplate Volcanic Rocks and Lower-Crustal Xenoliths*, 207 pp, Lehigh University, Bethlehem, PA.

1128 Avdeev, B., N. A. Niemi, and M. K. Clark (2011), Doing more with less: Bayesian estimation of erosion models with detrital thermochronometric data, *Earth and Planetary Science Letters*, 305(3), 385-395.

1131 Baldwin, J. A., K. X. Whipple, and G. E. Tucker (2003), Implications of the shear stress river incision model for the timescale of postorogenic decay of topography, *Journal of Geophysical Research: Solid Earth (1978–2012)*, 108(B3).

1134 Bayasgalan, A., J. Jackson, and D. McKenzie (2005), Lithosphere rheology and active tectonics in Mongolia: relations between earthquake source parameters, gravity and GPS measurements, *Geophysical Journal International*, 163(3), 1151-1179.

1137 Beucher, R., P. Beek, J. Braun, and G. E. Batt (2012), Exhumation and relief development in the Pelvoux and Dora - Maira massifs (western Alps) assessed by spectral analysis and inversion of thermochronological age transects, *Journal of Geophysical Research: Earth Surface*, 117(F3).

1141 Braun, J. (2002), Quantifying the effect of recent relief changes on age-elevation relationships, *Earth and Planetary Science Letters*, 200(3-4), 331-343.

1143 Braun, J. (2003), Pecube: a new finite-element code to solve the 3D heat transport equation including the effects of a time-varying, finite amplitude surface topography, *Computers & Geosciences*, 29(6), 787-794.

1146 Braun, J., and X. Robert (2005), Constraints on the rate of post-orogenic erosional decay from low-temperature thermochronological data: application to the Dabie Shan, China, *Earth Surface Processes and Landforms*, 30(9), 1203-1225.

1149 Braun, J., P. van der Beek, P. Valla, X. Robert, F. Herman, C. Glotzbach, V. Pedersen, C. Perry, T. Simon-Labric, and C. Prigent (2012), Quantifying rates of landscape evolution and tectonic processes by thermochronology and numerical modeling of crustal heat transport using PECUBE, *Tectonophysics*, 524-525, 1-28.

1153 Brewer, I., D. Burbank, and K. Hodges (2003), Modelling detrital cooling - age populations: Insights from two Himalayan catchments, *Basin Research*, 15(3), 305-320.

1155 Brocklehurst, S. H., and K. X. Whipple (2004), Hypsometry of glaciated landscapes, *Earth Surface Processes and Landforms*, 29(7), 907-926.

1157 Cai, K., M. Sun, B.-m. Jahn, W. Xiao, C. Yuan, X. Long, H. Chen, and D. Tumorhhuu (2015), A synthesis of zircon U-Pb ages and Hf isotopic compositions of granitoids from Southwest  
1158



- 1159 Mongolia: Implications for crustal nature and tectonic evolution of the Altai  
1160 Superterrane, *Lithos*, 232, 131-142.
- 1161 Carlson, R. W., and D. Ionov (2014), Lithospheric Mantle Contribution to High Topography in  
1162 Central Mongolia, American Geophysical Union, Fall Meeting 2014, abstract #T21A-  
1163 4556, San Francisco, CA.
- 1164 Caves, J. K., D. J. Sjostrom, H. T. Mix, M. J. Winnick, and C. P. Chamberlain (2014),  
1165 Aridification of Central Asia and uplift of the Altai and Hangay Mountains, Mongolia:  
1166 Stable isotope evidence, *American Journal of Science*, 314(8), 1171-1201.
- 1167 Chen, M., F. Niu, Q. Liu, and J. Tromp (2015), Mantle-driven uplift of Hangai Dome: New  
1168 seismic constraints from adjoint tomography, *Geophysical Research Letters*, 42(17),  
1169 6967-6974.
- 1170 Cogné, J.-P., V. A. Kravchinsky, N. Halim, and F. Hankard (2005), Late Jurassic-Early  
1171 Cretaceous closure of the Mongol-Okhotsk Ocean demonstrated by new Mesozoic  
1172 palaeomagnetic results from the Trans-Baikal area (SE Siberia), *Geophysical Journal  
1173 International*, 163(2), 813-832.
- 1174 Cunningham, W. D. (2001), Cenozoic normal faulting and regional doming in the southern  
1175 Hangay region, Central Mongolia: implications for the origin of the Baikal rift province,  
1176 *Tectonophysics*, 331(4), 389-411.
- 1177 Cunningham, W. D. (2013), Mountain building processes in intracontinental oblique deformation  
1178 belts: Lessons from the Gobi Corridor, Central Asia, *Journal of Structural Geology*, 46,  
1179 255-282.
- 1180 Cunningham, W. D. (2017), Folded basinal compartments of the southern Mongolian  
1181 borderland: A structural archive of the final consolidation of the Central Asian Orogenic  
1182 Belt, *Geosciences*, 7(2); doi:10.3390/geosciences7010002
- 1183 De Grave, J., M. M. Buslov, P. Van Den Haute, J. Metcalf, B. Dehandschutter, and M. O.  
1184 McWilliams (2009), Multi-method chronometry of the Teletskoye graben and its  
1185 basement, Siberian Altai Mountains: new insights on its thermo-tectonic evolution,  
1186 *Geological Society, London, Special Publications*, 324(1), 237-259.
- 1187 Devyatkin, E. V. (1975), Neotectonic structures of western Mongolia (in Russian): Mesozoic and  
1188 Cenozoic Tectonics and Magmatism of Mongolia: Moscow, Nauka, 264-282.
- 1189 Egholm, D. L., M. F. Knudsen, and M. Sandiford (2013), Lifespan of mountain ranges scaled by  
1190 feedbacks between landsliding and erosion by rivers, *Nature*, 498(7455), 475-478.
- 1191 Ehlers, T. A., A. Szameitat, E. Enkelmann, B. J. Yanites, and G. J. Woodsworth (2015),  
1192 Identifying spatial variations in glacial catchment erosion with detrital thermochronology,  
1193 *Journal of Geophysical Research: Earth Surface*, 120(6), 1023-1039.
- 1194 Farley, K. A. (2000), Helium diffusion from apatite; general behavior as illustrated by Durango  
1195 fluorapatite, *Journal of Geophysical Research*, 105(B2), 2903-2914.
- 1196 Farley, K. A., D. L. Shuster, and R. A. Ketcham (2011), U and Th zonation in apatite observed  
1197 by laser ablation ICPMS, and implications for the (U-Th)/He system, *Geochimica et  
1198 Cosmochimica Acta*, 75(16), 4515-4530.
- 1199 Fischer, K. M. (2002), Waning buoyancy in the crustal roots of old mountains, *Nature*,  
1200 417(6892), 933-936.
- 1201 Fitzgerald, P. G., S. L. Baldwin, L. E. Webb, and P. B. O'Sullivan (2006), Interpretation of (U-  
1202 Th)/He single grain ages from slowly cooled crustal terranes: A case study from the  
1203 Transantarctic Mountains of southern Victoria Land, *Chemical Geology*, 225(1-2), 91-  
1204 120.

- 1205 Flowers, R. M., R. A. Ketcham, D. L. Shuster, and K. A. Farley (2009), Apatite (U–Th)/He  
1206 thermochronometry using a radiation damage accumulation and annealing model,  
1207 *Geochimica et Cosmochimica Acta*, 73(8), 2347-2365.
- 1208 Fox, M., R. Reverman, F. Herman, M. G. Fellin, P. Sternai, and S. D. Willett (2014), Rock uplift  
1209 and erosion rate history of the Bergell intrusion from the inversion of low temperature  
1210 thermochronometric data, *Geochemistry, Geophysics, Geosystems*, 15(4), 1235-1257.
- 1211 Gautheron, C., L. Tassan-Got, J. Barbarand, and M. Pagel (2009), Effect of alpha-damage  
1212 annealing on apatite (U–Th)/He thermochronology, *Chemical Geology*, 266(3), 157-170.
- 1213 Glorie, S., and J. De Grave (2016), Exhuming the Meso–Cenozoic Kyrgyz Tianshan and  
1214 Siberian Altai-Sayan: A review based on low-temperature thermochronology, *Geoscience*  
1215 *Frontiers*, 7(2), 155-170.
- 1216 Glotzbach, C., P. A. Van Der Beek, and C. Spiegel (2011), Episodic exhumation and relief  
1217 growth in the Mont Blanc massif, Western Alps from numerical modelling of  
1218 thermochronology data, *Earth and Planetary Science Letters*, 304(3), 417-430.
- 1219 Hendrix, M. S., S. A. Graham, A. R. Carroll, E. R. Sobel, C. L. McKnight, B. J. Schulein, and Z.  
1220 Wang (1992), Sedimentary record and climatic implications of recurrent deformation in  
1221 the Tian Shan: Evidence from Mesozoic strata of the north Tarim, south Junggar, and  
1222 Turpan basins, northwest China, *Geological Society of America Bulletin*, 104(1), 53-79.
- 1223 Herman, F., E. J. Rhodes, J. Braun, and L. Heiniger (2010), Uniform erosion rates and relief  
1224 amplitude during glacial cycles in the Southern Alps of New Zealand, as revealed from  
1225 OSL-thermochronology, *Earth and Planetary Science Letters*, 297(1), 183-189.
- 1226 Hetzel, R., I. Dunkl, V. Haider, M. Strobl, H. von Eynatten, L. Ding, and D. Frei (2011),  
1227 Peneplain formation in southern Tibet predates the India-Asia collision and plateau uplift,  
1228 *Geology*, 39(10), 983-986.
- 1229 Hopkins, C. E. (2012), Beryllium-10 derived erosion rates from the Hangay Mountains,  
1230 Mongolia: landscape evolution in a periglacially-dominated continental interior, 48 pp,  
1231 Georgia Institute of Technology.
- 1232 Hunt, A. C., I. J. Parkinson, N. B. W. Harris, T. L. Barry, N. W. Rogers, and M. Yondon (2012),  
1233 Cenozoic Volcanism on the Hangai Dome, Central Mongolia: Geochemical Evidence for  
1234 Changing Melt Sources and Implications for Mechanisms of Melting, *Journal of*  
1235 *Petrology*.
- 1236 Idleman, B. D., P. K. Zeitler, and K. T. McDannell (2018), Characterization of helium release  
1237 from apatite by continuous ramped heating, *Chemical Geology*, 476, 223-232.  
1238 <https://doi.org/10.1016/j.chemgeo.2017.11.019>
- 1239 Ionov, D. A., S. Y. O'Reilly, and W. L. Griffin (1998), A geotherm and lithospheric section for  
1240 central Mongolia (Tariat region), *Mantle dynamics and plate interactions in East Asia*,  
1241 127-153.
- 1242 Jahn, B., F. Wu, and B. Chen (2000), Granitoids of the Central Asian Orogenic Belt and  
1243 continental growth in the Phanerozoic, *Geological Society of America Special Papers*,  
1244 350, 181-193.
- 1245 Jasra, A., D. Stephens, K. Gallagher, and C. Holmes (2006), Analysis of geochronological data  
1246 with measurement error using Bayesian mixtures, *Mathematical Geology*, 38(3), 269-  
1247 300.
- 1248 Johnson, C., K. Constenius, S. Graham, G. Mackey, T. Menotti, A. Payton, and J. Tully (2015),  
1249 Subsurface evidence for late Mesozoic extension in western Mongolia: tectonic and  
1250 petroleum systems implications, *Basin Research*, 27(3), 272-294.

- 1251 Jolivet, M. (2017), Mesozoic tectonic and topographic evolution of Central Asia and Tibet: a  
 1252 preliminary synthesis, *Geological Society, London, Special Publications*, 427(1), 19-55.
- 1253 Jolivet, M., S. Arzhannikov, A. Arzhannikova, A. Chauvet, R. Vassallo, and R. Braucher (2013),  
 1254 Geomorphic Mesozoic and Cenozoic evolution in the Oka-Jombolok region (East Sayan  
 1255 ranges, Siberia), *Journal of Asian Earth Sciences*, 62, 117-133.
- 1256 Jolivet, M., S. Bourquin, G. Heilbronn, C. Robin, L. Barrier, M.-P. Dabard, Y. Jia, E. De  
 1257 Pelsmaeker, and B. Fu (2015), The Upper Jurassic–Lower Cretaceous alluvial-fan  
 1258 deposits of the Kalaza Formation (Central Asia): tectonic pulse or increased aridity?,  
 1259 *Geological Society, London, Special Publications*, 427, SP427. 426.
- 1260 Jolivet, M., J.-F. Ritz, R. Vassallo, C. Larroque, R. Braucher, M. Todbileg, A. Chauvet, C. Sue,  
 1261 N. Arnaud, and R. De Vicente (2007), Mongolian summits: an uplifted, flat, old but still  
 1262 preserved erosion surface, *Geology*, 35(10), 871-874.
- 1263 Jolivet, M., T. De Boisgrollier, C. Petit, M. Fournier, V. Sankov, J. C. Ringenbach, L. Byzov, A.  
 1264 Miroshnichenko, S. N. Kovalenko, and S. Anisimova (2009), How old is the Baikal Rift  
 1265 Zone? Insight from apatite fission track thermochronology, *Tectonics*, 28(3).
- 1266 Koppes, M. N., and D. R. Montgomery (2009), The relative efficacy of fluvial and glacial  
 1267 erosion over modern to orogenic timescales, *Nature Geoscience*, 2(9), 644-647.
- 1268 Kopylova, M. G., S. Y. O'Reilly, and Y. S. Genshaft (1995), Thermal state of the lithosphere  
 1269 beneath Central Mongolia: evidence from deep-seated xenoliths from the Shavaryn-  
 1270 Saram volcanic centre in the Tariat depression, Hangai, Mongolia, *Lithos*, 36(3-4),  
 1271 243-255.
- 1272 Kröner, A., E. Hegner, B. Lehmann, J. Heinhorst, M. T. D. Wingate, D. Y. Liu, and P. Ermelov  
 1273 (2008), Palaeozoic arc magmatism in the Central Asian Orogenic Belt of Kazakhstan:  
 1274 SHRIMP zircon ages and whole-rock Nd isotopic systematics, *Journal of Asian Earth  
 1275 Sciences*, 32(2-4), 118-130.
- 1276 Landman, R. L. (2007), Petrologic constraints on the sources of granites from the Hangay  
 1277 Mountains, central Mongolia, 73 pp, Amherst College.
- 1278 Lehmann, J., K. Schulmann, O. Lexa, M. Corsini, A. Kroner, P. Stipska, D. Tomurhuu, and D.  
 1279 Otgonbator (2010), Structural constraints on the evolution of the Central Asian Orogenic  
 1280 Belt in SW Mongolia, *American Journal of Science*, 310(7), 575-628.
- 1281 Lehmkuhl, F. (1998), Quaternary glaciations in central and western Mongolia, *Journal of  
 1282 Quaternary Science*, 13(6), 153-167.
- 1283 Lehmkuhl, F., M. Klinge, and G. Stauch (2004), The extent of Late Pleistocene glaciations in the  
 1284 Altai and Khangai Mountains, in *Developments in Quaternary Sciences*, edited by J.  
 1285 Ehlers and P. L. Gibbard, pp. 243-254, Elsevier.
- 1286 Lehmkuhl, F., and A. Lang (2001), Geomorphological investigations and luminescence dating in  
 1287 the southern part of the Khangay and the Valley of the Gobi Lakes (Central Mongolia),  
 1288 *Journal of Quaternary Science*, 16(1), 69-87.
- 1289 Logachev, N. A., E. V. Devyatkin, E. M. Malaeva, and e. al. (1982), Cenozoic Deposits in the  
 1290 Taryat Basin and in the Chulutu R. Valley, Central Khangai, *Izv. AN SSSR. Ser. Geol.,  
 1291 no. 8*, 76-86.
- 1292 Lysak, S., and R. Dorofeeva (2003), Thermal state of lithosphere in Mongolia, *Russ. Geol.  
 1293 Geophys*, 44(9), 893-903.
- 1294 Mancktelow, N. S., and B. Grasemann (1997), Time-dependent effects of heat advection and  
 1295 topography on cooling histories during erosion, *Tectonophysics*, 270(3), 167-195.

- 1296 Matmon, A., P. R. Bierman, J. Larsen, S. Southworth, M. Pavich, and M. Caffee (2003),  
1297 Temporally and spatially uniform rates of erosion in the southern Appalachian Great  
1298 Smoky Mountains, *Geology*, 31(2), 155-158.
- 1299 McDannell, K. T. (2017), Methods and application of deep-time thermochronology: Insights  
1300 from slowly cooled terranes of Mongolia and the North American craton. Theses and  
1301 Dissertations. 2721. 261 p., Lehigh University, Bethlehem, Pennsylvania.  
1302 <https://preserve.lehigh.edu/etd/2721>
- 1303 McDannell, K. T., P. K. Zeitler, D. G. Janes, B. D. Idleman, and A. K. Fayon (2018), Screening  
1304 apatites for (U-Th)/He thermochronometry via continuous ramped heating: He age  
1305 components and implications for age dispersion, *Geochimica et Cosmochimica Acta*, 223,  
1306 90-106. <https://doi.org/10.1016/j.gca.2017.11.031>
- 1307 McDowell, F. W., W. C. McIntosh, and K. A. Farley (2005), A precise 40 Ar–39 Ar reference  
1308 age for the Durango apatite (U–Th)/He and fission-track dating standard, *Chemical  
1309 Geology*, 214(3), 249-263.
- 1310 McKeon, R. E., P. K. Zeitler, F. J. Pazzaglia, B. D. Idleman, and E. Enkelmann (2014), Decay of  
1311 an old orogen: Inferences about Appalachian landscape evolution from low-temperature  
1312 thermochronology, *Geological Society of America Bulletin*, 126(1-2), 31-46.
- 1313 Meltzer, A., et al. (2012), Intracontinental Deformation and Surface Uplift-Geodynamic  
1314 Evolution of the Hangay Dome, Mongolia Central Asia, American Geophysical Union,  
1315 Fall Meeting 2012, abstract #T12A-05, San Francisco, CA.
- 1316 Meltzer, A., et al. (2015), Betwixt and Between: Structure and Evolution of Central Mongolia,  
1317 American Geophysical Union, Fall Meeting 2015, abstract #T22A-05, San Francisco,  
1318 CA.
- 1319 Molnar, P., and P. Tapponnier (1975), Cenozoic tectonics of Asia: effects of a continental  
1320 collision, *Science*, 189(4201), 419-426.
- 1321 Molnar, P., and P. England (1990), Late Cenozoic uplift of mountain ranges and global climate  
1322 change: chicken or egg?, *Nature*, 346(6279), 29-34.
- 1323 Molnar, P., W. R. Boos, and D. S. Battisti (2010), Orographic controls on climate and  
1324 paleoclimate of Asia: thermal and mechanical roles for the Tibetan Plateau, *Annual  
1325 Review of Earth and Planetary Sciences*, 38(1), 77.
- 1326 Montgomery, D. R., and M. T. Brandon (2002), Topographic controls on erosion rates in  
1327 tectonically active mountain ranges, *Earth and Planetary Science Letters*, 201(3), 481-  
1328 489.
- 1329 Petit, C., C. Tiberi, A. Deschamps, and J. Déverchère (2008), Teleseismic traveltimes,  
1330 topography and the lithospheric structure across central Mongolia, *Geophysical Research  
1331 Letters*, 35(11).
- 1332 Petit, C., J. Deverchère, E. Calais, V. San'kov, and D. Fairhead (2002), Deep structure and  
1333 mechanical behavior of the lithosphere in the Hangai-Hovsgol region, Mongolia: new  
1334 constraints from gravity modeling, *Earth and Planetary Science Letters*, 197(3), 133-149.
- 1335 Raymo, M. E., and W. F. Ruddiman (1992), Tectonic forcing of late Cenozoic climate. *Nature*,  
1336 359(6391), 117-122.
- 1337 Reiners, P. W., and S. Nicolescu (2006), Measurement of parent nuclides for (U-Th)/He  
1338 chronometry by solution sector ICP-MS *ARHDL Report 3.0*, University of Arizona.
- 1339 Reiners, P. W., Z. Zhou, T. A. Ehlers, C. Xu, M. T. Brandon, R. A. Donelick, and S. Nicolescu  
1340 (2003), Post-orogenic evolution of the Dabie Shan, eastern China, from (U-Th)/He and  
1341 fission-track thermochronology, *American Journal of Science*, 303(6), 489-518.

- 1342 Reverman, R. L., M. G. Fellin, F. Herman, S. D. Willett, and C. Fitoussi (2012), Climatically  
 1343 versus tectonically forced erosion in the Alps: Thermochronometric constraints from the  
 1344 Adamello Complex, Southern Alps, Italy, *Earth and Planetary Science Letters*, 339, 127-  
 1345 138.
- 1346 Rickwood, P., and M. Sambridge (2006), Efficient parallel inversion using the Neighbourhood  
 1347 Algorithm, *Geochemistry, Geophysics, Geosystems*, 7(11).
- 1348 Ruhl, K. W., and K. V. Hodges (2005), The use of detrital mineral cooling ages to evaluate  
 1349 steady state assumptions in active orogens: An example from the central Nepalese  
 1350 Himalaya, *Tectonics*, 24(4), TC4015.
- 1351 Sahagian, D., A. Proussevitch, L. D. Ancuta, B. D. Idleman, and P. K. Zeitler (2016), Uplift of  
 1352 Central Mongolia Recorded in Vesicular Basalts, *The Journal of Geology*, 124(4), 435-  
 1353 445.
- 1354 Sambridge, M. (1999a), Geophysical inversion with a neighbourhood algorithm—I. Searching a  
 1355 parameter space, *Geophysical Journal International*, 138(2), 479-494.
- 1356 Sambridge, M. (1999b), Geophysical inversion with a neighbourhood algorithm—II. Appraising  
 1357 the ensemble, *Geophysical Journal International*, 138(3), 727-746.
- 1358 Shuster, D. L., R. M. Flowers, and K. A. Farley (2006), The influence of natural radiation  
 1359 damage on helium diffusion kinetics in apatite, *Earth and Planetary Science Letters*,  
 1360 249(3-4), 148-161.
- 1361 Smith, S. G., K. W. Wegmann, L. D. Ancuta, J. C. Gosse, and C. E. Hopkins (2016),  
 1362 Paleotopography and erosion rates in the central Hangay Dome, Mongolia: Landscape  
 1363 evolution since the mid-Miocene, *Journal of Asian Earth Sciences*, 125, 37-57.
- 1364 Stachnik, J. C., A. Meltzer, S. Souza, U. Munkhuu, B. Tsaagan, and R. M. Russo (2014),  
 1365 Lithospheric Structure Beneath the Hangay Dome, Central Mongolia, in *American*  
 1366 *Geophysical Union*, AGU abstract T21A-4555, San Francisco.
- 1367 Stock, G. M., T. A. Ehlers, and K. A. Farley (2006), Where does sediment come from?  
 1368 Quantifying catchment erosion with detrital apatite (U-Th)/He thermochronometry,  
 1369 *Geology*, 34(9), 725-728.
- 1370 Stock, J. D., and D. R. Montgomery (1996), Estimating palaeorelief from detrital mineral age  
 1371 ranges, *Basin Research*, 8(3), 317-327.
- 1372 Stosch, H. G., D. A. Ionov, I. S. Puchtel, S. J. G. Galer, and A. Sharpouri (1995), Lower crustal  
 1373 xenoliths from Mongolia and their bearing on the nature of the deep crust beneath central  
 1374 Asia, *Lithos*, 36(3-4), 227-242.
- 1375 Strahler, A. N. (1952), Hypsometric (area-altitude) analysis of erosional topography, *Geological*  
 1376 *Society of America Bulletin*, 63(11), 1117-1142.
- 1377 Stüwe, K., L. White, and R. Brown (1994), The influence of eroding topography on steady-state  
 1378 isotherms. Application to fission track analysis, *Earth and Planetary Science Letters*,  
 1379 124(1-4), 63-74.
- 1380 Tiberi, C., A. Deschamps, J. Déverchère, C. Petit, J. Perrot, D. Appriou, V. Mordvinova, T.  
 1381 Dugaarma, M. Ulzibaat, and A. Artemiev (2008), Asthenospheric imprints on the  
 1382 lithosphere in Central Mongolia and Southern Siberia from a joint inversion of gravity  
 1383 and seismology (MOBAL experiment), *Geophysical Journal International*, 175(3), 1283-  
 1384 1297.
- 1385 Tomurtogoo, O., ed., 1999, Geological Map of Mongolia. Mongolian Academy of Sciences,  
 1386 1:1,000,000.

- 1387 Tomurtogoo, O., B. Windley, A. Kröner, G. Badarch, and D. Liu (2005), Zircon age and  
1388 occurrence of the Adaatsag ophiolite and Muron shear zone, central Mongolia:  
1389 constraints on the evolution of the Mongol–Okhotsk ocean, suture and orogen, *Journal of*  
1390 *the Geological Society*, 162(1), 125-134.
- 1391 Valla, P. G., F. Herman, P. A. van der Beek, and J. Braun (2010), Inversion of  
1392 thermochronological age-elevation profiles to extract independent estimates of  
1393 denudation and relief history — I: Theory and conceptual model, *Earth and Planetary*  
1394 *Science Letters*, 295(3-4), 511-522.
- 1395 van der Beek, P., D. Delvaux, P. Andriessen, and K. Levi (1996), Early Cretaceous denudation  
1396 related to convergent tectonics in the Baikal region, SE Siberia, *Journal of the Geological*  
1397 *Society*, 153(4), 515-523.
- 1398 van der Beek, P. A., P. G. Valla, F. Herman, J. Braun, C. Persano, K. J. Dobson, and E. Labrin  
1399 (2010), Inversion of thermochronological age–elevation profiles to extract independent  
1400 estimates of denudation and relief history — II: Application to the French Western Alps,  
1401 *Earth and Planetary Science Letters*, 296(1–2), 9-22.
- 1402 Van der Voo, R., D. J. J. van Hinsbergen, M. Domeier, W. Spakman, and T. H. Torsvik (2015),  
1403 Latest Jurassic–earliest Cretaceous closure of the Mongol-Okhotsk Ocean: A  
1404 paleomagnetic and seismological-tomographic analysis, *Geological Society of America*  
1405 *Special Papers*, 513.
- 1406 Vassallo, R., M. Jolivet, J. F. Ritz, R. Braucher, C. Larroque, C. Sue, M. Todbileg, and D.  
1407 Javkhlanbold (2007), Uplift age and rates of the Gurvan Bogd system (Gobi-Altay) by  
1408 apatite fission track analysis, *Earth and Planetary Science Letters*, 259(3,Äi4), 333-346.
- 1409 Vermeesch, P. (2010), HelioPlot, and the treatment of overdispersed (U–Th–Sm)/He data,  
1410 *Chemical Geology*, 271(3–4), 108-111.
- 1411 Vermeesch, P. (2012), On the visualisation of detrital age distributions, *Chemical Geology*, 312,  
1412 190-194.
- 1413 Wegmann, K. W., et al. (2014), Geomorphic and Fish Genetics Constraints on Late Cenozoic  
1414 Long Wavelength Topographic Evolution of the Hangay Mountains, Central Mongolia,  
1415 American Geophysical Union, Fall Meeting 2014, abstract #T21A-4560, San Francisco,  
1416 CA.
- 1417 West, A. J., M. Fox, R. T. Walker, A. Carter, T. Harris, A. B. Watts, and B. Gantulga (2013),  
1418 Links between climate, erosion, uplift, and topography during intracontinental mountain  
1419 building of the Hangay Dome, Mongolia, *Geochemistry, Geophysics, Geosystems*,  
1420 14(12), 5171-5193.
- 1421 Whipp, D., T. Ehlers, J. Braun, and C. Spath (2009), Effects of exhumation kinematics and  
1422 topographic evolution on detrital thermochronometer data, *Journal of Geophysical*  
1423 *Research: Earth Surface*, 114(F4).
- 1424 Windley, B. F., and M. B. Allen (1993), Mongolian plateau: Evidence for a late Cenozoic mantle  
1425 plume under central Asia, *Geology*, 21(4), 295-298.
- 1426 Windley, B. F., D. Alexeiev, W. Xiao, A. Kröner, and G. Badarch (2007), Tectonic models for  
1427 accretion of the Central Asian Orogenic Belt, *Journal of the Geological Society*, 164(1),  
1428 31-47.
- 1429 Yang, Y.-T., Z.-X. Guo, C.-C. Song, X.-B. Li, and S. He (2015), A short-lived but significant  
1430 Mongol–Okhotsk collisional orogeny in latest Jurassic–earliest Cretaceous, *Gondwana*  
1431 *Research*, 28(3), 1096-1116.

- 1432 Yanovskaya, T., and V. Kozhevnikov (2003), 3D S-wave velocity pattern in the upper mantle  
 1433 beneath the continent of Asia from Rayleigh wave data, *Physics of the Earth and*  
 1434 *Planetary Interiors*, 138(3), 263-278.
- 1435 Yanshin, A. L. (1975), Mesozoic and Cenozoic tectonics and the magmatism of Mongolia: Joint  
 1436 Soviet-Mongolian scientific research geological expedition, *Transactions*, 11, 308.
- 1437 Yarmolyuk, V., B. Litvinovsky, V. Kovalenko, B.-M. Jahn, A. Zanvilevich, A. Vorontsov, D.  
 1438 Zhuravlev, V. Posokhov, D. Kuzmin, and G. Sandimirova (2001), Formation stages and  
 1439 sources of the peralkaline granitoid magmatism of the Northern Mongolia-Transbaikalia  
 1440 Rift Belt during the Permian and Triassic, *Petrology*, 9(4), 302-328.
- 1441 Yarmolyuk, V., et al. (2008), The age of the Khangai batholith and the problem of batholith  
 1442 formation in Central Asia, *Doklady Earth Sciences*, 423(1), 1223-1228.
- 1443 Yin, A. (2010), Cenozoic tectonic evolution of Asia: A preliminary synthesis, *Tectonophysics*,  
 1444 488(1), 293-325.
- 1445 Zeitler, P. K., A. S. Meltzer, P. O. Koons, D. Craw, B. Hallet, C. P. Chamberlain, W. S. Kidd, S.  
 1446 K. Park, L. Seeber, and M. Bishop (2001), Erosion, Himalayan geodynamics, and the  
 1447 geomorphology of metamorphism, *GSA Today*, 11(1), 4-9.
- 1448 Zorin, Y. A., M. R. Novoselova, E. K. Turutanov, and V. M. Kozhevnikov (1990), Structure of  
 1449 the lithosphere of the Mongolian-Siberian mountainous province, *Journal of*  
 1450 *Geodynamics*, 11(4), 327-342.
- 1451 Zorin, Y. A. (1999), Geodynamics of the western part of the Mongolia-Okhotsk collisional belt,  
 1452 Trans-Baikal region (Russia) and Mongolia, *Tectonophysics*, 306(1), 33-56.

## 1453 1454 1455 **FIGURE CAPTIONS**

1456  
 1457 **Figure 1:** Regional map showing areas of high topography within Mongolia and southern Russia. The  
 1458 mean elevation in this view extent is  $1500 \pm 563$  m and shows that the Hangay, Khövsgöl, Khentiyn, and  
 1459 Sayan Mountains (Russia) are a region of long-wavelength, high topography that has been dissected by  
 1460 the Selenga River network that drains the northern flank of the Hangay into Lake Baikal. Note that the  
 1461 deformation patterns vary regionally, i.e. the strong, large fault control in the Altai versus the diffuse,  
 1462 smaller faults of the Hangay. The dark brown line denotes the 1500 m topographic contour. Regional fault  
 1463 systems are also shown; the sinistral Bulnai (BF) is the major strike-slip fault north of the Hangay  
 1464 separating the Sayan/Khövsgöl from the Hangay. The Mongolian (MA) and Gobi Altai (GA) ranges south  
 1465 of the Hangay are within a major transpressional fault system. The Siberian craton margin begins just  
 1466 north of the Sayan Mountains in the < 500 m elevation region (green) near the Mongolia-Russia border  
 1467 and Lake Baikal at ~53°N latitude. Blue lines are major permanent streams draining higher elevations and  
 1468 the red line denotes the Selenga River system drainage divide. Heavy white line is Mongolian political  
 1469 border. Green dashed line is approximate Mongol-Okhotsk Ocean suture after *Van der Voo et al.* [2015].  
 1470 Yellow star is Ulaanbaatar, the capital city. (MA=Mongolian Altai; GA=Gobi Altai; DL=Depression of  
 1471 Lakes; VL=Valley of Lakes; HM=Hangay Mountains; LK=Lake Khövsgöl; KM=Khentiyn Mountains;  
 1472 SM=Sayan Mountains; OR=Orkhon River; SR=Selenga River; LB=Lake Baikal; SB=Selenga basin).  
 1473 Major towns in Hangay region shown on figure 2.

1474  
 1475 **Figure 2:** The eastern Hangay Mountains and major rivers (blue lines) with high elevation areas glaciated  
 1476 in the LGM shown in gray. River incision estimates at locations (triangles) from basalt age data presented  
 1477 in *Ancuta* [2017]. Numbers shown are in incision rates in m/My. Circled area in the southeast is the  
 1478 headwaters of the Orkhon River. Gray triangle is the Orkhon waterfall location (Ulaan Tsutgalan). Photo  
 1479 on the right shows a canyon location along the Orkhon River, at lower elevations in the Selenga River

1480 basin, where the higher incision rates (~58 m/My) are due to local basalt flow damming (~180 m total  
1481 thickness) over the past 3 m.y. Red dots mark major towns in the area. B = Bayankhongor; J = Jargalant;  
1482 T = Tariat; Tg = Tsetserleg; Ts = Tosontsengal. Photo: The contact between granitic basement and the  
1483 basalt flows is shown by the red line in the photo. Apatite (U-Th)/He sample 12MN09 is from the granite  
1484 bedrock [mean (U-Th)/He age of ~325 Ma].  
1485

1486 **Figure 3:** Imagery showing the regional topography near the highest Hangay peak, Otgontenger Uul  
1487 (triangle). The areas outlined in white are the ELA for the LGM at 2800 m elevation. The image below is  
1488 of the same area as above but showing elevations >2800 m (gray area is <2800 m) and areas with slopes  
1489  $\leq 5^\circ$  (orange). Enlarged digital elevation model (DEM) inset (top right, looking  $240^\circ$  at  $20^\circ$  inclination)  
1490 shows example of high elevation relict planation surface and associated cryoplanation features east of  
1491 Otgontenger. Bottom panel is a slope map of another such area to the south with a flat, relict surface and  
1492 cryoplanation terraces. See *West et al.*, [2013] for other examples.  
1493

1494 **Figure 4:** (A) Hypsometry of the Selenga and Orkhon River sub-catchments sampled for detrital AHe  
1495 (see figure 5 for locations; section 5 for discussion). (B) Schematic diagram illustrating the relationship  
1496 between detrital thermochronometer data and the hypsometry of a catchment given an assumed positive  
1497 age-elevation relationship where cooling ages should match the hypsometric curve if erosion is uniform,  
1498 i.e. all points on the topography produce cooling ages that correspond to the basin AER. If there is non-  
1499 uniform erosion, then the elevations on the landscape contributing sediments will affect the SPDF curve  
1500 accordingly, modified after *Stock et al.* [2006].  
1501

1502 **Figure 5:** Granitic-bedrock mean AHe ages across the Hangay Mountains and north-central Mongolia  
1503 colored by age. The majority of cooling ages in the Hangay are ca. 100-120 Ma, with a slightly younger  
1504 grouping <100 Ma on the north flank (red/white center). Off the Hangay, ages are similar, albeit with  
1505 greater scatter and an older component greater than ca. 120 Ma. Detrital sample locations are shown as  
1506 diamonds (mean age in italics). The red line shows the Selenga watershed and sub-catchments with  
1507 respect to detrital samples for the Selenga and Orkhon are the orange lines. Points tagged in yellow are  
1508 AHe/AFT transect (W) of *West et al.* [2013] shown in blue diamonds, transect (L) of *Landman* [2007]  
1509 near Egiin Davaa, and transect (T) discussed with figures 7 and 8. OT = Otgontenger Uul. Grayscale 90 m  
1510 DEM with 1700 m contour to mark higher elevations above the regional background and onset of  
1511 'regional knickpoint elevation zone' discussed in text and with fig. 7. Glaciated high elevations areas  
1512 shown in cyan blue, derived from the ELA during the LGM from *Lehmkuhl* [1998]. Major faults from  
1513 *Tomurtogoo* [1999] geologic map of Mongolia shown by heavy black lines. See supplement for full age  
1514 dataset.  
1515

1516 **Figure 6:** Selenga and Orkhon River detrital apatite (U-Th)/He cooling age populations shown by kernel  
1517 density estimator (KDE) (smooth, gray envelope) and probability density functions (PDF) (shaded blue)  
1518 from DensityPlotter [*Vermeesch*, 2012] using a Gaussian kernel and adaptive bandwidth (varied based on  
1519 local data density). White dots show individual grain ages for the datasets. The y-axis is number of grains.  
1520

1521 **Figure 7:** (A) Normalized CSPDF curves of Selenga detrital ages (dashed lines,  $t^*$ ) and catchment  
1522 elevations (solid line,  $z^*$ ) for the Selenga River, using 95% and 99% of the detrital dataset, after *Ruhl and*  
1523 *Hodges* [2005]. (B) SPDF curves for normalized age (gray) and elevation (solid black line) distributions  
1524 with inset age and elevations (upper right). Dashed line in (B) is the 'ideal' age SPDF obtained from  
1525 inverting the observed age SPDF and hypsometric curves with respect to the regional AER from the  
1526 northern Hangay (figure 5, transect labelled T). Small inset panels show ages for 95% of the detrital AHe  
1527 dataset and the elevations in the Selenga sub-catchment and red shading shows the dominant mismatch in  
1528 age/elevation from the ideal age SPDF, see text for details.  
1529



1530 **Figure 8:** Apatite AERs (left panel) from the western Hangay near Otgontenger (highest peak; figs. 3 and  
1531 4) incorporating a short transect from this study and from *West et al.* [2013] and *Landman* [2007] datasets  
1532 (see fig. 5 for transect locations). Positive AERs suggest valley-scale topographic wavelengths do not  
1533 affect low-T isotherms. Right panels show AFT and mean fission-track lengths (MTL) for *Jolivet et al.*  
1534 [2007] and *West et al.* [2013] datasets. Planation surfaces in the Gobi Altai, Valley of Lakes, and W.  
1535 Hangay (gray) are all similar in age suggesting regionally coincident exhumation and that highest  
1536 elevations are preserved remnants from an older event. *West et al.* AFT transect suggests the period  
1537 between ~180-130 Ma being governed by a moderate exhumation rate. Our rates and those published on  
1538 the right are for the AHe transects and overestimate the true exhumation rate.

1539  
1540 **Figure 9:** Pecube-NA sensitivity test of variables controlling relief to assess the ability to resolve relief  
1541 change in this type of slow exhumation setting. For tests, a two-phase exhumation scenario was used with  
1542 fixed rates of 100 m/My and 30 m/My. **(A)** Sensitivity test for *relief amplitude-only* showing least-  
1543 squares misfit and relief amplitude between 0 (no relief) to 2 (two times modern relief) with a defined  
1544 misfit minima at the true value of 0.5X the modern relief in the Hangay. **(B)** Misfit evolution over the  
1545 sensitivity test inversion where  $\tau$ ,  $R$ , and  $E$ -timing are allowed free, exhibiting optimal convergence after  
1546 >6000 models. **(C)** Correlation matrix for the free inversion parameters using NA-plot [*Sambridge,*  
1547 1999b]. Values approaching (-1)+1 show greater (anti)-correlation while values near 0 show no  
1548 relationship or dependence. Erosional timescale and relief amplitude are highly anti-correlated, while both  
1549 the exhumation rate change timing and relief amplitude have a slight positive correlation with erosional  
1550 timescale. These trends can also be seen in the PPDFs in panels D to F. **(D-F)** Scatter plots showing misfit  
1551 between  $\tau$ ,  $R$  and  $E$ -timing, the 2-D PPDF  $1\sigma$  (solid) and  $2\sigma$  (dashed) contours shown as overlays and the  
1552 corresponding 1-D marginal PPDF curves for each parameter on the corresponding axes. In each case the  
1553 star marks both the ‘true parameter value’ and in this case, the respective lowest misfit of the 1-D PPDF,  
1554 which in this synthetic example is also the mean or modal value.

1555  
1556 **Figure 10:** Pecube-NA inversion results for Run 1-TSW. Scatter plots are 2-D projections of the 5  
1557 dimensional parameter space on planes defined by combinations of two parameters. 1-D posterior curves  
1558 show probability density within the parameter search range. See supplementary material for additional  
1559 plots of other variables. Each dot represents a forward model from the inversion and is colored by the  $\chi^2$   
1560 misfit value. Stars denote the lowest misfit model while heavy/thin black lines are  $1\sigma$  (67% confidence)  
1561 and  $2\sigma$  (95% confidence) errors, respectively. Bottom middle panel shows misfit evolution and  
1562 convergence during the inversion and the bottom right shows the correlation matrix between difference  
1563 parameters between -1 to +1 signifying strong (negative) anti-correlation or positive correlation, with  
1564 values near zero having no relationship. Pecube physical modeling domain shown in fig. 13 inset box, see  
1565 text for discussion.

1566  
1567 **Figure 11:** Pecube-NA Run 1-C inversion results for 9504 models. The same figure scheme as figure 9.  
1568 The difference between Run 1-TSW is that the exhumation rate change timing is allowed free in this  
1569 inversion.

1570  
1571 **Figure 12:** **(A)** Contoured age map (5 Ma interval) of Pecube-NA Run 1-TSW in the western Hangay  
1572 (see fig. 13 for location, inset box). Locations of samples are circles with mean ages shown, ages in red  
1573 are multi-grain aliquots from *West et al.* [2013]. Note that single grain ages were used in the inversion.  
1574 Single grains shown in panel D. **(B)** Plot showing how topography changes in the model according to  
1575 equation 6. Our model inversion 1-TSW exhibits highly positive best-fit values for  $\tau$ , suggesting relief  
1576 decayed rapidly and was  $\geq 90\%$  of the modern relief by ca. 100-85 Ma. **(C)** A plot of single-grain AHe  
1577 ages with respect to  $eU$  for a few samples in the modeling domain. The Pecube model predictions (stars)  
1578 are fairly consistent with observed age- $eU$  patterns. **(D)** Observed and predicted cooling ages and  
1579 corresponding elevations are in good agreement except mainly at the highest elevations which are derived  
1580 from Pecube forward models using our best-fit or maximum likelihood values from the model inversion.

1581 Black circles are observed single-grain age replicates with errors, while squares are predicted cooling  
1582 ages. **(E)** 1-to-1 line for predicted vs. observed cooling ages; gray squares are AFT samples. **(F)** observed  
1583 versus predicted elevations using best-fit 1-TSW inversion relief scenario in Pecube forward model.  
1584

1585 **Figure 13:** Pecube forward model age predictions using inversion run 1-TSW best-fit parameter values  
1586 with the main exhumation stage from 150-130 Ma after *West et al.* [2013] model thermal history. Inset  
1587 box shows location of western Hangay bounds used in Pecube-NA inversion. Regional forward models  
1588 are resampled at 10 km to smooth ages and are shown with a 5 Ma contour interval. (Top left) Elevations  
1589 from 90m SRTM DEM (2000 m elev. contoured) with white dots showing sample locations used in  
1590 Pecube modeling of the entire Hangay, (top right) the ages predicted by the best-fit model results of  
1591 inversion 1-TSW shown in table 1 ( $T_e = 6.1$  km). Other panels show the effects of varying the effective  
1592 elastic thickness ( $T_e$ ) while holding all other best-fit variables constant.  
1593

1594 **Figure 14:** Pecube forward model results for a planation surface and carving of topographic relief **(A)**  
1595 The model starting condition for topography is a high plateau at the highest modern elevation (slightly  
1596 lower than actual due to grid resampling). See elevation scale in panel B. **(B)** The end of the model run  
1597 showing the modern topography. This relief was created using an erosional timescale of 930 My, which  
1598 created the modern topography (within 90%) by 100-85 Ma. Note: although difficult to see, there are  
1599 remnant surfaces (red) at highest elevations in panel B. **(C)** The predicted AHe age map across the region.  
1600 Ages are best predicted in the Hangay but suggest younger ages outside of the Hangay, which is not in  
1601 total agreement with real AHe data. Circles are the locations of real data used in the model **(D)** The  
1602 predicted exhumation rates over the single time step with two phases of exhumation using the best-fit  
1603 values from inversion 1-TSW. The rates are spatially variable and show no erosion at highest peaks and  
1604 more focused/higher exhumation in the incised topography. Exhumation rates are on par with previously  
1605 mentioned long-term estimates and inversion results between 4-16 m/My. **(E)** The observed and predicted  
1606 single-grain AHe ages going from west to east in panel C showing a good match (also refer to fig. 5 for  
1607 AHe age reference). The MSWD model misfit is 0.92 between observed/predicted and shaded gray  
1608 denotes single-grain age outliers. **(F)** The observed and predicted elevations for a ‘planation surface’  
1609 exhumation model displaying excellent correlation ( $R^2=0.92$ ) and suggesting the exhumation/relief  
1610 evolution model is viable at orogeny-scale. Line is 1-to-1 for reference.  
1611

1612 **Table 1:** Fixed model parameters used in Pecube inversions to calculate the isostatic and thermal  
1613 response to varying relief.  
1614

1615 **Table 2:** Pecube-NA inversion results for sensitivity test and full inversions. Values separated by a colon  
1616 are the prior search ranges during the NA sampling stage while those in bold are the best-fit parameter  
1617 values (lowest misfit). Mean and standard deviation represent the resampling results from the NA  
1618 appraisal of the model ensemble.  $R$  = relief amplitude;  $\tau$  = erosional timescale; E-timing is the time of  
1619 exhumation rate change;  $E_1$  and  $E_2$  = exhumation rate 1 and exhumation rate 2. See text for details.  
1620  
1621  
1622